博士学位論文

太陽光エネルギー変換用の多様な機能を有する酸化チタンメソ結晶光触媒に関する研究

張　鵬

2016 年 1 月

大阪大学大学院工学研究科

Preface

The studies presented in this thesis were carried out under the direction of Professor Tetsuro Majima, the Institute of Scientific and Industrial Research (SANKEN), Osaka University during October 2012 to March 2016.

The object of this thesis is the development of modified or doped TiO_2 mesocrystals with versatile applications in solar energy converstion from UV to visible light range. The aim of this research is to resolve the problems of low photocatalytic efficiency and intrinsic wide bang gap of TiO_2 after facilely improved with co-catalyst, tunable anisotroptic crystal facet, and doping. The author hopes that the results and conclusion presented in this thesis contribute to the further improvement of the quantum efficiency with practical application, which will deepen our understanding of the good relationship between their structure and phtocatalytic performance.

Peng Zhang

Department of Applied Chemistry
Graduate School of Engineering
Osaka University
2016

Contents

General Introduction

Over the past decades, the rapid depletion of fossil fuels and serious environmental pollution started to strongly affect the modern society, such as the air pollution, water pollution and even our healthy body (PM 2.5). With concerning the deficiency of human energy usage and alleviating the environmental pollution, solar energy as the sustainable source is becoming the clean, cheap, renewable energy to fulfill rising global demand in our life. In this case, photocatalysis shows great potentials among the basic science like CO_2 photoreduction, environmental purification like photodegradation of organic pollutant, and fuel generation like water splitting, and so on.[1-3] With the recent boom of nanotechnology, research interests on the photocatalyst have been expanded to ultimate efficient mental oxide semiconductors with intriguing physiochemical property and exciting functions in photo(electro)catalysis. Due to the strong redox ability, high chemical stability, low toxicity, and abundant availability, titanium dioxide (TiO_2) is becoming a promising photocatalyst and applied in the wide range of solar-to-chemical energy conversion such as environmental remediation, solar water splitting, CO_2 photoreduction, and photovoltaic cells.[4-7] As the photocatalytic materials since 1972,[8] TiO_2 still represents problems in widespread applications of photovoltaics and photo(electro)catalysis inevitably due to its low quantum efficiency and wide band gap. A series of TiO_2 with good structure-performance relationship have been developed to significantly improve the quantum efficiency in photocatalysis.[9] For the low quantum efficiency, the efficient charge separation may retard the fast charge recombination from surface or volume in reaction process. The rapid and efficient collection of photogenerated electrons and holes on the catalytic sites (reduction or oxidation sites) from the surface is much more important to improve the reactive efficiency (Scheme 1A). In the development of a new class of porous materials, metal oxides mesocrystals are superstructures of assembled nanoparticles and have potentially tunable electronic, optical, and magnetic properties for applications ranging from catalysis to optoelectronics and to energy storage and conversion.[10,11] Recently, anatase TiO_2 mesocrystals (TMC) consisting of nanocrystal building blocks show significant enhancement of the charge separation and excellent photocatalytic activity compared with nanocrystal or commercial TiO_2.[12] It was clearly revealed

that the long-range ordered mesocrystal superstructures significantly retard the recombination of electron-hole pairs due to the efficient interparticle charge separation.[13] Therefore, it is strongly required to understand the relationship between the structural characteristics and the interfacial charge transfer dynamics to optimize the composite systems with highly improved catalytic performance.

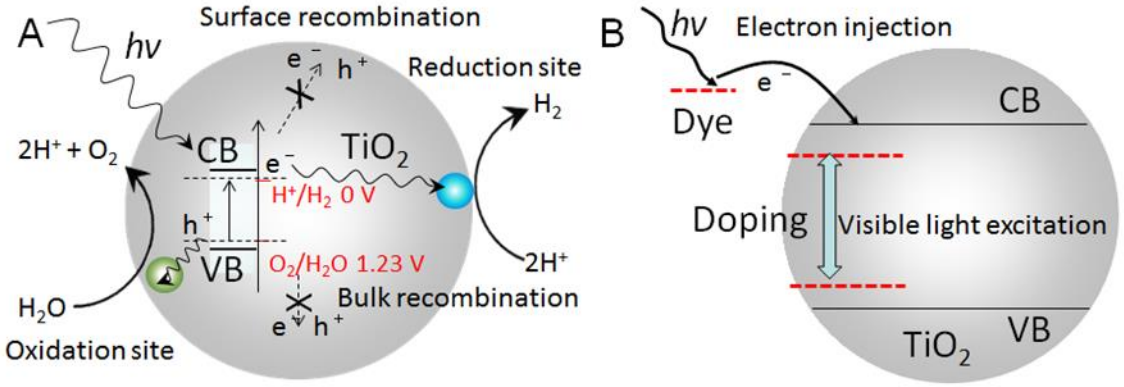

Scheme 1. (A) Charge separation on TiO_2 and (B) Activation of TiO_2 in visible light region.

On the other hand to resolve the problems of intrinsic wide band gap, many efforts have attempted to study band gap engineering of TiO_2 to achieve its visible-light-responding in practical application (Scheme 1B).[14,15] To date, a variety of modifications are exploited to extend the optical response of TiO_2 from UV to the visible light region, such as the nonmetal doping/codoping (N, S, C, F), metal deposition (Au, Cu, V, Cr), coupling with semiconductors (CdS, Bi_2S_3), defect engineering (Ti^{3+}), and dye sensitization (Ru complex).[15,16] It is worthy considering that for the large-scale preparation in practical application, the novel pyrolysis of titanium-compound containing dopants elements is proposed to be the ideal candidate for acquiring efficient doping. The ammonium oxofluorotitanate (NH_4TiOF_3) is a fundamental group of titanium-compound to synthesize doped TiO_2. It was inferred that the anisotropic dissolution of NH_4TiOF_3 can be chemically converted to TMC during the topochemical transformation, accompanying with N and F releasing. Therefore, it is a great of significance to introduce the dopant simultaneously from the original precursors or intermedium during the synthesis, without affecting the nucleation and growth of TMC. However, it still remains a challenge to facilely synthesize TMCs with higher visible-light activity instead of the instrument-dependent and cost-effective treatment in this field.

Introduction of each chapter is shown as below.

In Chapter 1, the reaction dynamics of charge separation (photogenerated electrons or holes) in the composites of CoPi-deposited TMC and MoS_2/TMC with superior efficiency was studied from ensemble-averaged experiment, single-particle spectroscopy, and time resolved transient absorption. The charge transfer dynamics between the superstructure (TMC) and the active sites (CoPi, Pt, and MoS_2) were monitored from the time-resolved and spatial resolution.

In Chapter 2, a series of TMCs with tunable facet ratio of {001} to {101} was successfully synthesized using a crystal growth inhibitor (NH_4F). Their photocatalytic performances were explored in pollutant degradation and H_2 evolution with anisotropic electron flow among the dominant facet from UV to visible light, where the {101} facets prefer reduction, whereas the {001} facets favor oxidation, because of crystal-facet-dependent surface adsorption and charge transfer.

In Chapter 3, topotactic transformation confined doping (F doping or N and F codoping) on TMC was facilely designed for the first time. Their comparison of charge transfer dynamics from time-resolved transient absorption to the photocatalytic efficiency could confirm the effect of the dopant (F dopant with improved electron conductivity or N, F codopants with improved surface modification) induced the different charge transfer dynamics in the hydrogen generation, photocatareductive Cr (VI), and dye degradation under the visible light or UV light irradiation.

Reference:

(1) Hoffmann, M. R.; Martin, S. T.; Choi, W.; Bahnemann, D. W. *Chem. Rev.* **1995**, *95*, 69.

(2) Chen, X.; Mao, S. S. *Chem. Rev.* **2007**, *107*, 2891.

(3) Chen, X.; Shen, S.; Guo, L.; Mao, S. S. *Chem. Rev.* **2010**, *110*, 6503.

(4) Ma, Y.; Wang, X.; Jia, Y.; Chen, X.; Han, H.; Li, C. *Chem. Rev.* **2014**, *114*, 9987.

(5) Wang, L.; Sasaki, T. *Chem. Rev.* **2014**, *114*, 9455.

(6) Bai, Y.; Mora-Sero, I.; De Angelis, F.; Bisquert, J.; Wang, P. *Chem. Rev.* **2014**, *114*, 10095.

(7) Walter, M. G.; Warren, E. L.; McKone, J. R.; Boettcher, S. W.; Mi, Q.; Santori, E. A.; Lewis, N. S. *Chem. Rev.* **2010**, *110*, 6446.

(8) Fujishima, A.; Honda, K. *Nature* **1972**, *238*, 37.

(9) Liu, G.; Yang, H. G.; Pan, J.; Yang, Y. Q.; Lu, G. Q.; Cheng, H. M. *Chem. Rev.* **2014**, *114*, 9559.

(10) Cölfen, H.; Antonietti, M. *Ang. Chem. Int. Ed.* **2005**, *44*, 5576.

(11) Zhou, L.; O'Brien, P. *J. Phys. Chem. Lett.* **2012**, *3*, 620.

(12) Bian, Z.; Tachikawa, T.; Majima, T. *J. Phys. Chem. Lett.* **2012**, *3*, 1422.

(13) Bian, Z.; Tachikawa, T.; Kim, W.; Choi, W.; Majima, T. *J. Phys. Chem. C* **2012**, *116*, 25444.

(14) Chen, X.; Liu, L.; Huang, F. *Chem. Soc. Rev.* **2015**, *44*, 1861.

(15) Pelaez, M.; Nolan, N. T.; Pillai, S. C.; Seery, M. K.; Falaras, P.; Kontos, A. G.; Dunlop, P. S. M.; Hamilton, J. W. J.; Byrne, J. A.; O'Shea, K.; Entezari, M. H.; Dionysiou, D. D. *Appl. Cat. B: Environ.* **2012**, *125*, 331.

(16) Asahi, R.; Morikawa, T.; Irie, H.; Ohwaki, T. *Chem. Rev.* **2014**, *114*, 9824.

Charpter 1: Spatial charge separation on TMC with efficient photocatalytic activity

The semiconductor photocatalysis research has been developed and a lot of achievements have been made, but there remain many key problems waited to be resolved such as the low photocatalytic efficiency. For the low quantum efficiency, the efficient charge separation may retard the fast charge recombination from surface or volume in reaction process. Rapid and efficient collection of photogenerated electrons and holes on the catalytic sites (reduction or oxidation sites) from the semiconductor surface is much important to improve the reactive efficiency. Semiconductors modified with co-catalysts strongly affect the water splitting from the structural characteristics and interfacial charge transfer dynamics. However, there is no report on the investigation of O_2 and H_2 evolution from the mesocrystal with such co-catalysts to improve the water-splitting efficiency.

Part 1. Co-catalysts selective on TMC with efficient charge separation in water splitting

1. Introduction

Semiconductors such as metal oxide have been studied extensively due to their potential applications among the photocatalysis, photovoltaics, batteries, and sensors.[1-6] In this regard, photocatalytic water splitting into H_2 and O_2 allows for the storage of solar energy as fuel source.[5,6] Rapid and efficient collection of multiple photogenerated charges of electrons (e^-) and holes (h^+) on the catalytic sites of the semiconductor surface to accompany the redox events and bond formation is of paramount importance in the entire reaction sequence. In this case, co-catalysts iridium oxides (IrO_x)[7-9] or cobalt oxides/oxyhydroxides (CoO_x/CoOOH)[10-12], have attracted great interest in modify on semiconductors surface, since they are widely applied as efficient photocatalysts to promote water oxidation. As we know, their photocatalytic performances are strongly influenced by the preparation and the electronic and morphological structures of the semiconductors and co-catalysts. It is strongly required to understand the

relationship between the structural characteristics and the interfacial charge transfer dynamics for optimization of the composite systems with efficient performance.

Anatase TiO_2 is one of the most promising semiconductors for heterogeneous photocatalysis owing to its low cost, stability, and nontoxicity.[13-16] As photocatalysts and electrode materials, traditional metal oxide nanoparticles have some limitations in practical applications due to the rapid charge recombination both in the bulk and on the surface. To resolve this point, metal oxide mesocrystals with high surface area and highly ordered nanocrystal building blocks, have recently been becoming a new class of porous semiconductor materials.[17-20] TMC could strongly enhance the efficiency of charge separation upon UV light irradiation, leading to remarkably long-lived charges, higher photoconductivity and photocatalytic activity.[19,20] However, there are no study on dealing with the fabrication and characterization of photoactive TMC with oxygen-evolving co-catalysts.

The plate-like structure of TMC is composed of aligned anatase TiO_2 nanocrystals with exposed dominant {001} facets in Fig. 1. Such a superstructure is beneficial for the migration of photogenerated e^- between adjacent nanocrystals upon UV light irradiation. One possible way to facilitate both charge separation and subsequent water splitting has been the deposition of cobalt phosphate (CoPi),[21,22] known as an efficient oxygen-evolving catalyst, onto semiconductor materials such as ZnO,[11] TiO_2,[23,24] Fe_2O_3,[12,25-28], WO_3,[29] and $BiVO_4$.[30] The hole-accepting states of Co species (Co^{II} and Co^{III}) in CoPi are located at energy levels above the valence band (VB) of TiO_2. Therefore, upon UV light irradiation, h^+ in the TiO_2 VB can be transferred to the CoPi catalysts and deposited on the surface.[23,24] The e^- in the conduction band (CB) of TiO_2 is possibly transferred to the high valence Co ion, eventually inhibiting the oxidation reactions owing to the undesired charge recombination.

In this part, the author used photochemical deposition method to modify TMC with CoPi and platinum (Pt) nanoparticles, which are commonly used as a co-catalyst for hydrogen evolution, and investigated the reaction dynamics of photogenerated charges in the composite by using steady-state and time-resolved spectroscopies. The charge transfer processes in inhomogeneous structures and environments are explored *in situ* single-particle fluorescence imaging techniques with fluorescence probes. To date, direct imaging methods based on optical absorption and fluorescence have been applied for screening and optimization of water oxidation catalysts,[31,32] but the present work is the first example of exploring the photooxidation activity of semiconductor-based composites at single-particle or single-aggregate level.

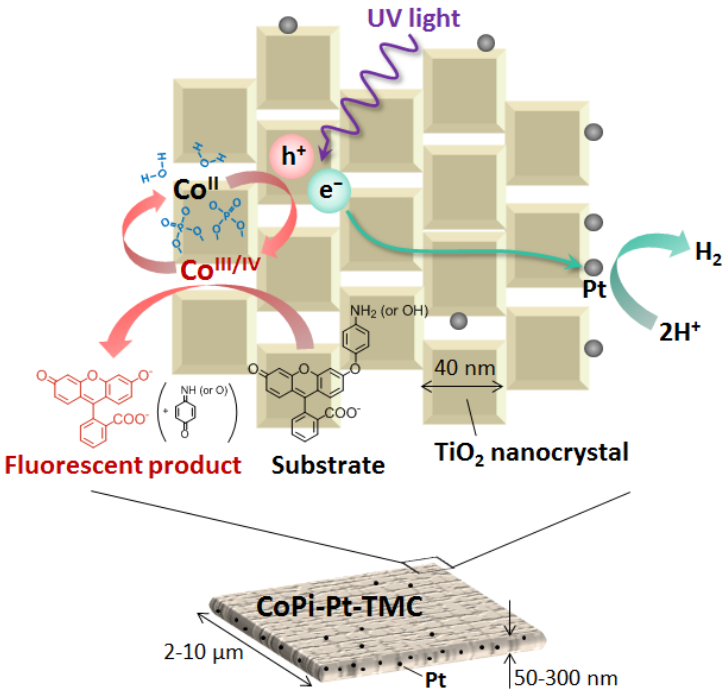

Fig. 1 Schematic illustration of charge transfer on the surface of CoPi-Pt-TMC. TMC is composed of aligned anatase TiO_2 nanocrystals. The width and thickness of TMC structures are 2–10 μm and 50–300 nm, respectively. Pt nanoparticles are deposited on the lateral surfaces of CoPi-TMC. Active $Co^{III/IV}$ species in CoPi as well as TiO_2 holes (h^+) oxidize 3'-*p*-aminophenyl fluorescein (APF) and 3'-*p*-hydroxyphenyl fluorescein (HPF) substrates to generate fluorescein as a fluorescent product and *p*-benzoquinone imine or *p*-benzoquinone as a byproduct, respectively, via *O*-dearylation reaction. TiO_2 electrons (e^-) migrate to the edges of TMC through the TiO_2 nanocrystal network, and they are eventually captured by Pt nanoparticles.[20]

2. Experimental Section

Materials. The chemicals for synthesis of catalysts were purchased from Aldrich, Wako, and Nacalai Tesque and used without further purification. Commercial ST21 (Ishihara Sangyo) and P25 (Nippon Aerosil) were used as received. TMC, Pt-TMC, and NanoTiO_2 (annealed under oxygen atmosphere at 500 ℃) were synthesized according to literature procedures.[19,20] 3'-*p*-aminophenyl fluorescein (APF) and 3'-*p*-hydroxyphenyl fluorescein (HPF) were purchased from Sekisui Medical and used without further purification. Fluorescein sodium salt was purchased from Tokyo Chemical Industry and used without further purification. *p*-Benzoquinone was purchased from Aldrich and purified by sublimation before use.

Synthesis of CoPi-TiO_2. In a typical synthesis of CoPi-TiO_2, 3 mg TiO_2 was mixed with a 3 ml solution of 0.5 mM $Co(NO_3)_2$ in 0.1 M sodium phosphate (NaPi) buffer at pH 7.0 forming a homogenous suspension. The suspensions were then exposed to UV light (315–400 nm, 580 mW cm^{-2}) from a mercury light source (Asahi Spectra, REX-250) at room temperature. Finally, the suspensions were centrifuged at 10000 rpm (Hitachi, himac CF16RX) to separate the solid products. The products were subsequently washed with Milli-Q water. The amounts of loaded Co were determined by UV-Vis absorption and EDX measurements.

Instruments. The samples were characterized using FESEM equipped with EDX analyzer (JEOL JSM-6330FT) and TEM equipped with EDX analyzer (Hitach H-800; operated at 200 kV). The steady-state UV-Vis absorption and diffuse reflectance spectra were measured by UV-Vis-NIR spectrophotometers (Shimadzu, UV-3100, and Jasco, V-570, respectively) at room temperature. The steady-state fluorescence spectra were measured using a HORIBA FluoroMax-4 fluorescence spectrophotometer at room temperature. EPR spectra were recorded on a JEOL JES-RE2X electron spin resonance spectrometer at 77 K. The g values were calibrated using Mn^{2+} in MgO as standard.

Time-Resolved Diffuse Reflectance Measurements. The sample suspensions containing the TiO_2 powders (20 g L^{-1}) were sonicated for 15 min and are placed in 1-mm light path quartz cuvettes before the measurements. The time-resolved diffuse reflectance measurements were performed using the third harmonic generation (355 nm, 5 ns full width at half-maximum, 1.5 mJ $pulse^{-1}$, 1 Hz) from a Q-switched Nd^{3+}:YAG laser (Continuum, Surelite II-10) for the excitation operated by temporal control using a delay generator (Stanford Research Systems, DG535). The reflected analyzing light from a continuous wave 450 W Xe-arc lamp (Ushio, UXL-451-0) was

collected by a focusing lens and directed through a grating monochromator (Nikon, G250) to a silicon avalanche photodiode detector (Hamamatsu Photonics, S5343). The transient signals were amplified with a voltage amplifier (Femto, DHPVA-100) and recorded by a digitizer (Tektronix, DPO3054). Time profiles were obtained from the average of 8 or 32 laser shots. All experiments were carried out at room temperature. The % absorption (%Abs) is given by equation: %Abs = $(R_0 - R)/R_0 \times 100$, where R and R_0 represent the intensities of the diffuse reflected monitor light with and without excitation, respectively.

Photooxidation Activity Tests. For typical runs, 3 mL of a phosphate buffer suspension containing TiO_2 (0.07 g L^{-1}) and APF (2 μM) was sonicated for 20 min, and then transferred into a quartz cuvette. The photochemical reaction was initiated upon irradiation with a mercury light source (Asahi Spectra, REX-250) through a filter (centered at 365 nm) at room temperature. The intensity of the UV light was measured to be 6 mW cm^{-2}. After stopping the UV light illumination, the sample was centrifuged at 10000 rpm (Hitachi, himac CF16RX) to separate the solid particles. The oxidation of APF was monitored by a UV-Vis spectrophotometer and the fluorescence from the products was analyzed by a fluorescence spectrophotometer.

Sample Preparation for Fluorescence Imaging. The cover glasses were purchased from Matsunami glass (Japan) and cleaned by sonication in a detergent solution for 4 h, followed by repeated washings with warm flowing water for 30 min. Finally, the cover glasses were washed again with Milli-Q ultrapure water (Millipore). Well-dispersed buffer suspensions of TiO_2 were subsequently spin-coated on the cleaned cover glasses. The cover glasses were placed in a sample chamber. A TiO_2-coated cover glass was mounted on the bottom of a holder designed for viewing specimens on the microscope. A silicon spacer with a 9 mm pore (Invitrogen) was placed on the TiO_2-coated glass to form a chamber. The chamber was filled with a sample solution and was then covered with a clean cover glass to prevent the solution from escaping.

Single-Particle Fluorescence Measurements with Wide-Field Microscopy. The experimental setup included an Olympus IX81 inverted fluorescence microscope. 488-nm CW laser (Coherent; ~3 W cm^{-2} at the glass surface) and 365-nm LED (Opto-Line; ~5 mW cm^{-2} at the glass surface) sources were used to excite the dyes and TiO_2, respectively. The optical transmission and emission images were recorded on an EMCCD camera (Roper Scientific, Evolve 512) at a frame rate of 20 frames s^{-1} using MetaMorph (Molecular Devices). All

experimental data were obtained at room temperature. Fluorescence images were analyzed using the Image J software (http://rsb.info.nih.gov/ij/).

Single-Particle PL Measurements with Time-Resolved Confocal Mcroscopy. Fluorescence lifetime images were recorded using an objective-scanning confocal microscope system (PicoQuant) coupled with an Olympus IX71 inverted fluorescence microscope. The samples were excited through an oil objective (Olympus, UPLSAPO 100XO; 1.40 NA, 100×) with a circular-polarized 485 nm pulsed laser (PicoQuant) controlled by a PDL-800B driver (PicoQuant). An instrument response function (IRF) of ~110 ps was obtained by measuring the scattered laser light in order to analyze the temporal profile. The emission was collected with the same objective and detected by a single photon avalanche photodiode (Micro Photon Devices, PDM 50CT) through a dichroic beam splitter (Chroma, z405/488rpc), a long-pass filter (Chroma, HQ510LP), a band-pass filter (Semrock, FF01-531/40), and a 75-μm pinhole for spatial filtering to reject out-of-focus signals. The data collected using the PicoHarp 300 TCSPC module (PicoQuant) were stored in the time-tagged time-resolved mode (TTTR), recording every detected photon with its individual timing, which were used for the analysis. All the experimental data were obtained at room temperature.

3. Results and Discussions

0.1 M phosphate (Pi) buffer suspensions (pH 7.0) containing TiO_2 powder and Co^{2+} ions were irradiated by UV light (315–400 nm, 580 mW cm^{-2}) for 3 h to deposit CoPi on the TiO_2 surface without any applied bias potential. Fig. 2A shows the field-emission scanning electron microscopy (FESEM) and energy dispersive X-ray (EDX) spectroscopic mapping images of CoPi-loaded TMC (CoPi-TMC). TMC is composed of aligned anatase TiO_2 nanocrystals with an average diameter of around 40 nm, and has a plate-like structure with a width of several micrometers and thickness of around 100 nm. Elemental mapping analysis revealed that Co and P elements are distributed over the surface of TMC, and their concentrations are lower than 1 wt%. As shown in Fig. 2B, EDX spectrum obtained from the surface of CoPi-TMC clearly indicates a Co Kα peak, which was not observed for the as-synthesized TMC. Transmission electron microscope (TEM) images revealed that CoPi-TMC consists of assembled TiO_2 nanoparticles and that it has many pores on its surface (the left and middle images of Fig. 2C). The electron diffraction pattern of the selected area shows single-crystal diffraction along with the anatase [001] zone axis (the image on the extreme right of Fig. 2C). Scanning TEM (STEM)-

EDX spectral measurements were selectively performed for the center and the edge of CoPi-TMC, as demonstrated in Fig. 2D, where Ti Kα peaks have been normalized for comparison. Co concentrations are 0.57 ± 0.15 and 0.71 ± 0.35 wt% near the center and the edge of TMC, respectively (five different crystals were analyzed).

The concentrations of Co deposited on different TiO_2 samples were further determined by two independent methods as follows: UV-Vis absorption measurements of residual Co^{2+} ions (with a peak at around 520 nm) in solutions after UV light irradiation and FESEM-EDX measurements. The concentrations of deposited Co under the same synthesis conditions are summarized in Table 1 along with the structural characteristics of TiO_2 used in this study. To facilitate the comparison, two TiO_2 samples with the anatase crystal phase were used, commercial TiO_2 (ST21, ST01) and synthesized TiO_2 (NanoTiO_2) nanocrystals. NanoTiO_2 has the truncated bipyramidal morphology with dominant {001} facets, analogous to the TiO_2 nanocrystal building blocks of TMC.[19] P25 consists of anatase and rutile crystalline phases and is frequently used as a benchmark in photocatalysis.

From Table 1, it is evident that Co species can be deposited more effectively on the surface of TMC than on the surface of other TiO_2 nanocrystals. During photochemical deposition, h^+ in the TiO_2 VB is used to oxidize Co^{2+} ions to deposit Co^{III} species as an oxide or as oxyhydroxides on the TiO_2 surface, while e^- in the TiO_2 CB reduces the Co^{III} species back to the starting Co^{II} material.[23,24] Therefore, the highest deposition ability of TMC is possibly due to the efficient charge separation owing to the ordered structure of TiO_2 nanocrystals. In addition, Pt nanoparticle-loaded TMC (Pt- TMC), with Pt nanoparticles of ~2.5 nm mostly located on the lateral surfaces containing {101} facets of TMC.[20] Pt nanoparticles loaded on TiO_2 could collect e^-, and thus greatly improve the oxidation efficiency, enhancing significantly the photochemical deposition of the Co species.

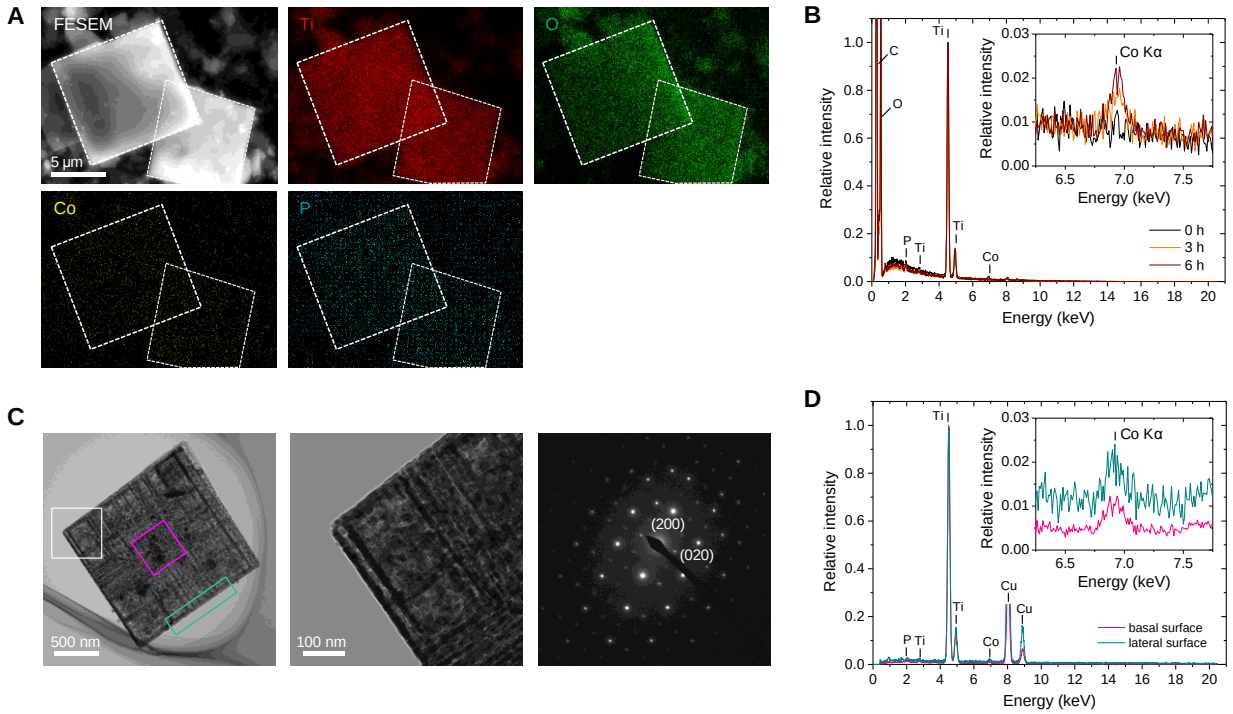

Fig. 2 (A) FESEM and elemental mapping images of CoPi-TMC. (B) FESEM-EDX spectra of TMC after the photodeposition of CoPi for 0, 3, and 6 h. (C) TEM images (left and middle) and diffraction pattern (right) observed for CoPi-TMC. The middle image represents the enlarged white square in the left image. (D) STEM-EDX spectra measured from the center and edge (which are represented by pink and green squares in TEM image (left), respectively) of CoPi-TMC synthesized by photodeposition for 3 h.

Table 1. Structural Characteristics and Photoactivity of CoPi-TiO_2

TiO_2	crystalline phase [a]	particle size (nm) [b]	surface area ($m^2\ g^{-1}$) [b]	deposition time (h)	Co loading (wt%)	Relative reaction rate [e]
TMC	A	39	63	3	0.69 [c], 0.80 [d]	1.0 (15)
Pt-TMC	A	–	–	0.5	1.1 [c], 2.5 [d]	36 (1.6)
P25	A/R	25	55	3	0.42 [c], 0.35 [d]	1.7 (5.1)
ST21	A	20	50	3	0.48 [c], 0.29 [d]	1.6 (5.1)
NanoTiO_2	A	25	41	3	0.49 [c], 0.53 [d]	1.0 (3.5)

[a] A and R mean anatase and rutile, respectively.
[b] Refs 19 and 20.

[c] Calculated from the absorbance of Co ions in solution.
[d] Obtained from FESEM-EDX analysis.
[e] Calculated from the temporal change of fluorescence intensity for the sample solutions before and after the UV light irradiation. The numbers in parentheses are the enhancements in the reaction rates after the CoPi deposition.

Fig. 3 shows the steady-state UV-Vis diffuse reflectance spectra of TMC (black solid line) and CoPi-TMC (orange solid line). CoPi-TMC sample displayed broad absorption covering the visible range, in addition to the strong absorption by TiO_2 in the UV region. Co oxides and oxyhydroxides with Co^{II} or Co^{III} states are known to have light-yellow or gray color, respectively,[33] which are in accordance with the observed spectra for CoPi-TMC.

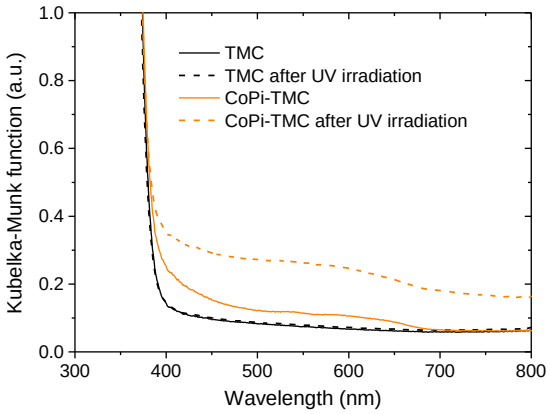

Fig. 3 Steady-state diffuse reflectance spectra of TMC (black) and CoPi-TMC (orange) in phosphate buffer solutions (0.1 M, pH 7.0) before (solid lines) and after (broken lines) 355-nm laser irradiation.

Time-resolved diffuse reflectance spectroscopy was employed to explore the reaction dynamics of photogenerated e^- and h^+ in TiO_2. As seen in Fig. 4A, TMC exhibits a broad transient absorption band in the visible to near-infrared range upon 355-nm laser excitation, which represents the overlapping of trapped h^+ (mainly 400–700 nm) and trapped e^- (mainly 500–850 nm).[34,35] Fig. 4C compares the transient absorption spectra observed at 1 μs in the presence and absence of CoPi on TMC. From spectral deconvolution into individual components, it was found that the presence of CoPi decreases the absorption intensity of trapped h^+ at around 500 nm (also see Fig. 4B for the spectra at different time regions). These results suggest that photogenerated (free and trapped) h^+ is transferred to the Co^{II} or Co^{III} species on the TiO_2 surface.

Barroso et al. observed long-time-scale bleaching at 580 nm for CoPi-Fe_2O_3 nanoparticles by time-resolved diffuse reflectance spectroscopy.[36] They explained this phenomenon in terms of the depletion of photogenerated h^+ in Fe_2O_3 by the transfer to Co, or losing the characteristic optical absorption of Co^{II} or Co^{III} species.

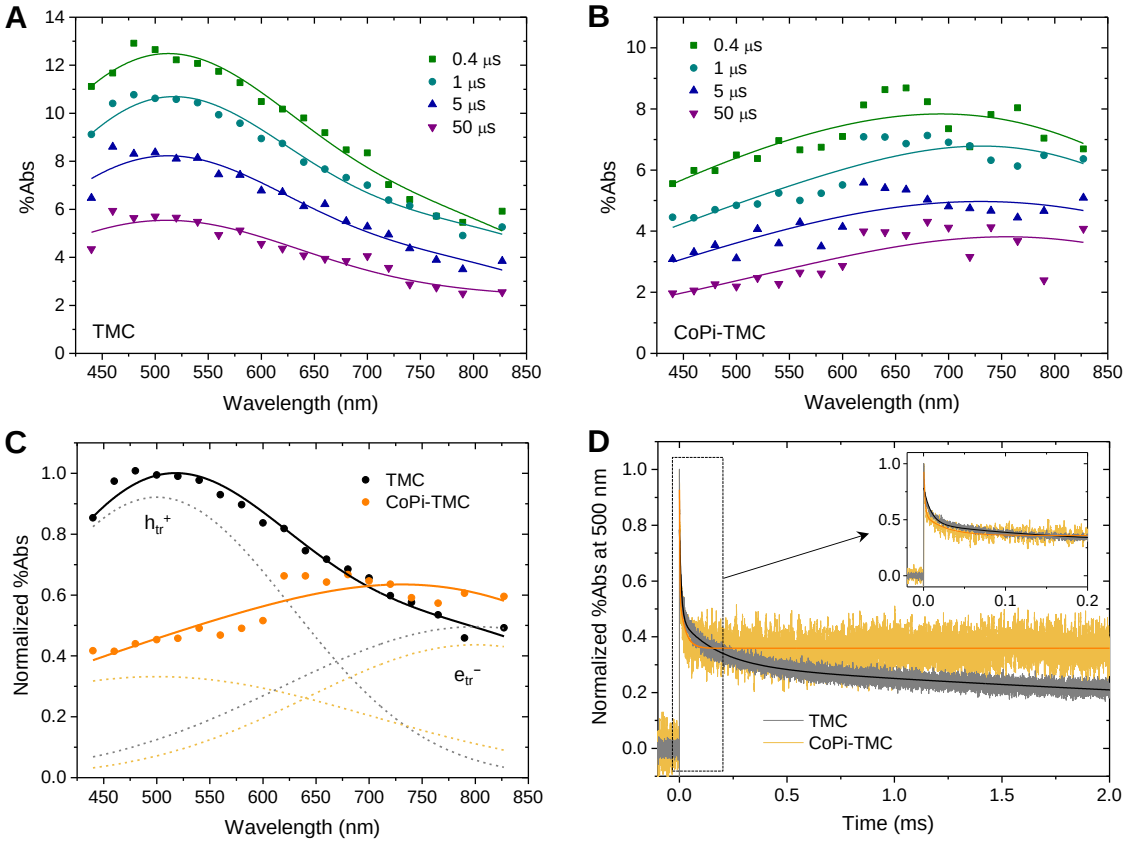

Fig. 4 Time-resolved diffuse reflectance spectra during the 355-nm laser photolysis of TMC (A) and CoPi-TMC (B) in phosphate buffer solutions. Comparisons of transient spectra at 1 μs (C) and time traces at 500 nm (D).

The decay profiles at 500 nm were analyzed by multi-exponential curve fitting and the determined lifetimes are summarized in Table 2. By CoPi deposition, the lifetimes of trapped h^+ shortened significantly compared with those in pure TMC, and a new long-lived component with lifetime of >10 ms appeared. Furthermore, they noticed that the color of CoPi-TMC suspension changed from pale yellow to dark blue upon the laser irradiation. This color change was significantly suppressed by saturating the suspension with oxygen gas (electron scavenger)

before the UV light irradiation. Steady-state diffuse reflectance measurements confirmed that a broad absorption band emerged in the 400–800 nm wavelength regions when CoPi-TMC powder in phosphate buffer solution was exposed to 355-nm laser light (Fig. 3). This resembles a well-known feature of e^- accumulated in TiO_2,[37,38] inferring that the observed non-decay component can be ascribed to the prolonged lifetime of trapped e^-.

Table 2. Decay Time Constants of Transient Absorption at 500 nm

TiO_2	lifetime (ms) [a]
TMC	0.009 (39%), 0.18 (22%), 5.7 (39%),
CoPi-TMC	0.0015 (54%), 0.026 (16%), >10 (30%)

[a] Determined by the non-linear least squares curve fitting. The numbers in parentheses are relative amplitudes.

The photoinduced charge transfer processes in CoPi-TMC were also confirmed by electron paramagnetic resonance (EPR) spectroscopy. EPR spectra of the samples were taken at 77 K before and after the UV light irradiation for 20 min at 77 K, and are given as differential EPR spectra in Fig. 5. The spectrum of TMC exhibits intense resonance peaks at g = 2.017, 2.012, and 2.003. This spectral feature has been assigned to the trapped h^+, *i.e.*, O^- in TiO_2, as reproduced from the reported EPR parameters (pink solid line).[39,40] The very weak resonance signal at g = 1.992 could be attributed to the trapped e^-, *i.e.*, Ti^{3+} in bulk.[41] This Ti^{3+} signal is known to weaken upon annealing at >250 ℃ in air (TMC used in this study was annealed at 500 ℃ during the synthesis).[42] On the other hand, the spectrum of CoPi-TMC has no assignable peaks related to the trapped charges in TiO_2. Although the EPR signals of Co species were not observed in the magnetic field range of 80–580 mT,[43] possibly due to their low concentrations, the observation suggests that photogenerated h^+ is scavenged by the CoPi deposited on the TiO_2 surface.

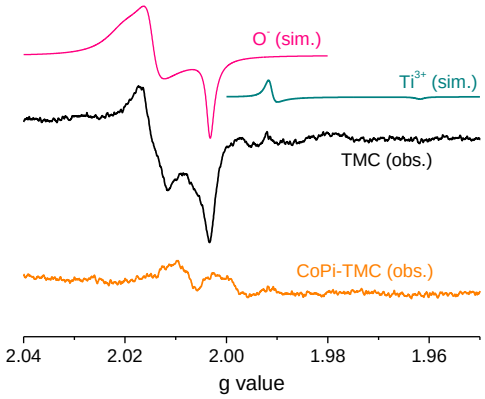

Fig. 5 Differential EPR spectra for TMC (black line) and CoPi-TMC (red line) in frozen buffer solutions, obtained by subtracting the spectra observed before the UV light irradiation from those after the UV light irradiation at 77 K. "Obs." and "sim." are the observed and simulated spectra, respectively. To reproduce the observed spectra, simulations were performed with the following EPR parameters: g_{xx} = 2.0205, g_{yy} = 2.0015, g_{zz} = 2.0035 for O^{-} and $g_{\parallel}$ = 1.9915, $g_{\perp}$ = 1.9620 for Ti^{3+}.

The energy diagram for the charge transfer on CoPi-TiO_2 surface is illustrated in Fig. 6. The holes transfer from excited TiO_2 to $Co^{II/III}$ species is thermodynamically possible, and this process enhances the efficiency of photoinduced charge separation, thereby ensuring substantial enhancement in photocatalytic activity for redox reactions. The photooxidation activity of bare TiO_2 and CoPi-TiO_2 was first evaluated by using ensemble-averaged spectroscopy. They used two fluorescence dye probes, 3'-*p*-aminophenyl fluorescein (APF) and 3'-*p*-hydroxyphenyl fluorescein (HPF), to selectively monitor the oxidation reaction. For instance, upon the oxidation of *p*-aminophenyl group of APF by TiO_2 h^+ or active $Co^{III/IV}$ species, APF produces fluorescein as a main fluorescent product and *p*-benzoquinone imine as a byproduct (*p*-benzoquinone for HPF) via oxidative *O*-dearylation reactions (Figs. 1 and 6).

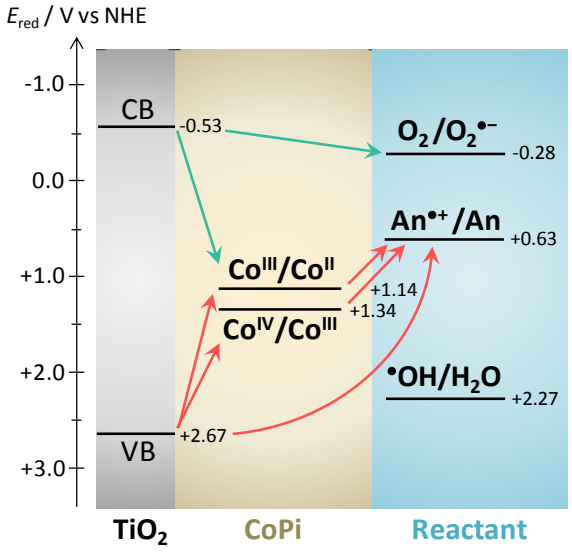

Fig. 6 Energy diagram for the interfacial charge transfer on CoPi-TiO_2.[43] CB and VB are conduction and valence bands of TiO_2, respectively. The band potentials are calculated from $E_{CB} = -0.12 - 0.059 \cdot pH$ and band gap energy of 3.2 eV.[44] "An" is aniline,[45] which is the preferable moiety for the oxidation of APF. The redox potential (E_{red}) of phenol, which is the preferable moiety for the oxidation of HPF, is +0.86 V vs. NHE.[46]

In bulk experiments, TiO_2 powder (0.07 g L^{-1}) dispersed in 3 mL of 2 μM APF phosphate buffer solution (pH 7.0) was irradiated in a 1 cm × 1 cm quartz cell by UV lamp (centered at 365 nm, 6 mW cm^{-2}). Dimethyl sulfoxide (DMSO) (100 mM) was added to the sample solution to scavenge $^{\bullet}OH$, which is highly reactive oxygen species generated during the TiO_2 photocatalytic reactions.[47] As shown in Fig. 7A, after UV light irradiation of CoPi and Pt nanoparticle-loaded TMC (CoPi-Pt-TMC) sample, the fluorescence intensity of the peak at 512 nm gradually increased, indicating the generation of fluorescein. Fig. 7B shows the time course of the fluorescence intensity for the TMC-based samples during UV light irradiation. In the absence of TiO_2 or UV light, the increase in the fluorescence intensity due to the UV light-induced oxidation or auto-oxidation of APF is almost negligible. It was concluded that the oxidation reactivity followed the order CoPi-Pt-TMC > Pt-TMC> CoPi-TMC > TMC. The deposition of Pt nanoparticles greatly enhances the activity, because part of e^- in TiO_2 is transferred to Pt before the charge recombination, thus increasing the concentration and lifetime of h^+ in TiO_2. The repeated deposition of CoPi on Pt-TMC enhances the photooxidation by an order of magnitude (Fig. 7C). Excess amount of CoPi caused a decrease in the activity, probably due to the

deactivation of $Co^{III/IV}$ species by capturing e^-. They also compared the activity of CoPi-TMC with those of the TiO_2 nanocrystal reference samples. As demonstrated in Fig. 7D, CoPi-loaded TMC showed the highest fluorescence intensity and activity enhancement among the tested TiO_2 samples, thus highlighting the importance of the ordered structure of TMC, especially when compared with NanoTiO_2 (see also Table 1).

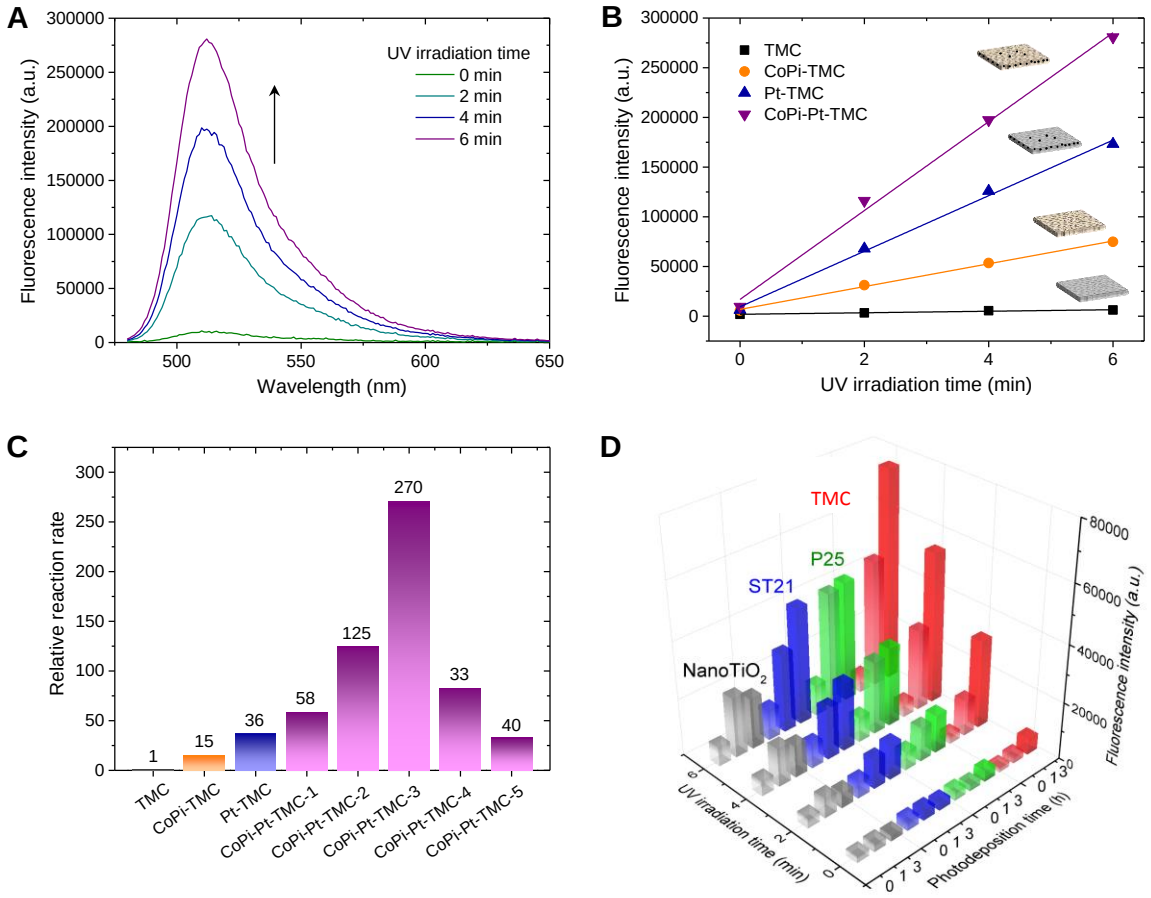

Fig. 7 (A) Fluorescence spectra of phosphate buffer solutions (0.1 M, pH 7.0) before and after the UV light irradiation of sample suspensions containing CoPi-Pt-TMC (0.07 g L^{-1}) and APF (2 μM) (excitation at 470 nm). TiO_2 powder was removed by centrifugation before the measurements. (B) UV light irradiation time dependence of fluorescence intensities monitored at 512 nm. In the illustrated structures of the samples, TMC and CoPi-TMC are shown in gray and ivory, respectively. Black dots indicate the Pt nanoparticles deposited on the surface. (C) Relative reaction rates obtained for TMC-based samples. The reaction rates were determined from the initial slopes of fluorescence intensity changes. The *n* of CoPi-Pt-TMC*n* (*n* = 1–5) is the number of repetitions for the CoPi deposition ([TMC] = 1 g L^{-1}, $[Co^{2+}]$ = 0.5 mM, UV light

irradiation time = 30 min). Each procedure can deposit ~1.1 wt% Co (estimated from UV-Vis absorption measurements) on the TMC surfaces. (D) Dependence of fluorescence intensity on the UV light irradiation time and photodeposition time for phosphate buffer solutions containing the reaction products.

Based on the results above, they have evaluated the photooxidation activity of individual CoPi-TMC crystals by *in situ* fluorescence imaging. Experiments on a single crystal provide useful information for elucidating the inherent heterogeneity of the reaction processes on surfaces.[48,49] Figs. 8A and B show typical optical transmission and fluorescence images of a single CoPi-TMC crystal in 2 μM HPF phosphate buffer solution (0.1 M, pH 7.0), respectively. The crystal was illuminated by the evanescent light of 488-nm continuous wave laser (penetration depth is ~200 nm) or 365-nm LED light to excite the fluorescence dye or TiO_2, respectively. The initial fluorescence observed prior to the UV light irradiation is ascribed to the HPF molecules adsorbed on the surface. Under the experimental conditions, the contributions of the scattered light from the crystal and the fluorescence from the products directly oxidized by UV light irradiation are negligible due to the low excitation intensity (~3 W cm^{-2} and ~5 mW cm^{-2} at the cover glass surface for 488 nm and 365 nm light, respectively).[45,47] Interestingly, the area near the edge of the CoPi-TMC crystal showed higher fluorescence intensity than that near the center (Figs. 8B and 9A, respectively). The average intensity ratio of the edge (within 1 μm distance from the lateral faces) and the center is 1.4 ± 0.2, which is greater than that (1.1 ± 0.1) of the bare TMC. Previously, it was demonstrated by site-selective deposition of Pt nanoparticles and single-molecule fluorescence imaging of reduction sites with a specific fluorogenic probe that the photogenerated e^- in TMC can reach the lateral surfaces over a micrometer distance through the nanocrystal network.[20] Assuming that fluorescence intensity correlated directly with the number of adsorbed HPF molecules, the observed spatial distribution of fluorescence intensity implies that Co species are readily deposited near the edge of TMC, and their concentration gradually decreases towards the center. This tendency was confirmed by the STEM-EDX analysis (Fig. 2D). Moreover, it is obvious from the transmission and fluorescence images (Figs. 8D and E) that the well-ordered parts of TMC exhibit higher fluorescence intensity, *i.e.*, higher concentration of Co species, than the broken parts of TMC. Although it is difficult to observe selectively the reaction processes on the basal and lateral surfaces of CoPi-TMC because of the limited spatial resolution (~250 nm), the findings support the hypothesis that well-ordered

structures of TMC can effectively deliver e^- to the lateral surfaces, thereby increasing the oxidation reaction efficiency.

As predicted by the ensemble experiments, the fluorescence intensity on the crystal underwent a substantial increase immediately after the UV light irradiation (Figs. 8C and F). Moreover, the UV light-induced increase in fluorescence intensity around the perimeter of the crystal indicates that the fluorescent products diffused from the crystal surface into the bulk solution. This result supports the proposed mechanism for the oxidation of the probes (Fig. 1), and it is well consistent with the fact that more than 90% of fluorescent products are separated from the sample suspensions by centrifugation or filtration, possibly owing to the electrostatic repulsion between negatively charged TiO_2 surface (isoelectric point ≈ 5.5) and fluorescein dianion (p*K*a 6.4) in water at pH 7.0.[50] Considering the pore size distribution of TMC (5.1 ± 2.5 nm)[19] and the hydrodynamic radius of fluorescein (0.8 nm),[51] the escape of the product fluorescein molecules into the bulk solution should however be partially restricted, allowing us to observe the change in fluorescence intensity over the crystal. The change in the fluorescence intensity varies strongly from crystal to crystal, as shown in Fig. 9G. Meaningful positive correlation was observed for the initial fluorescence intensity with UV light-induced fluorescence intensity changes on the surface (corrected $R^2 = 0.72$) and in solution near the crystal (corrected $R^2 = 0.51$) (Fig. 8H), again indicating the photooxidation of preadsorbed HPF molecules.

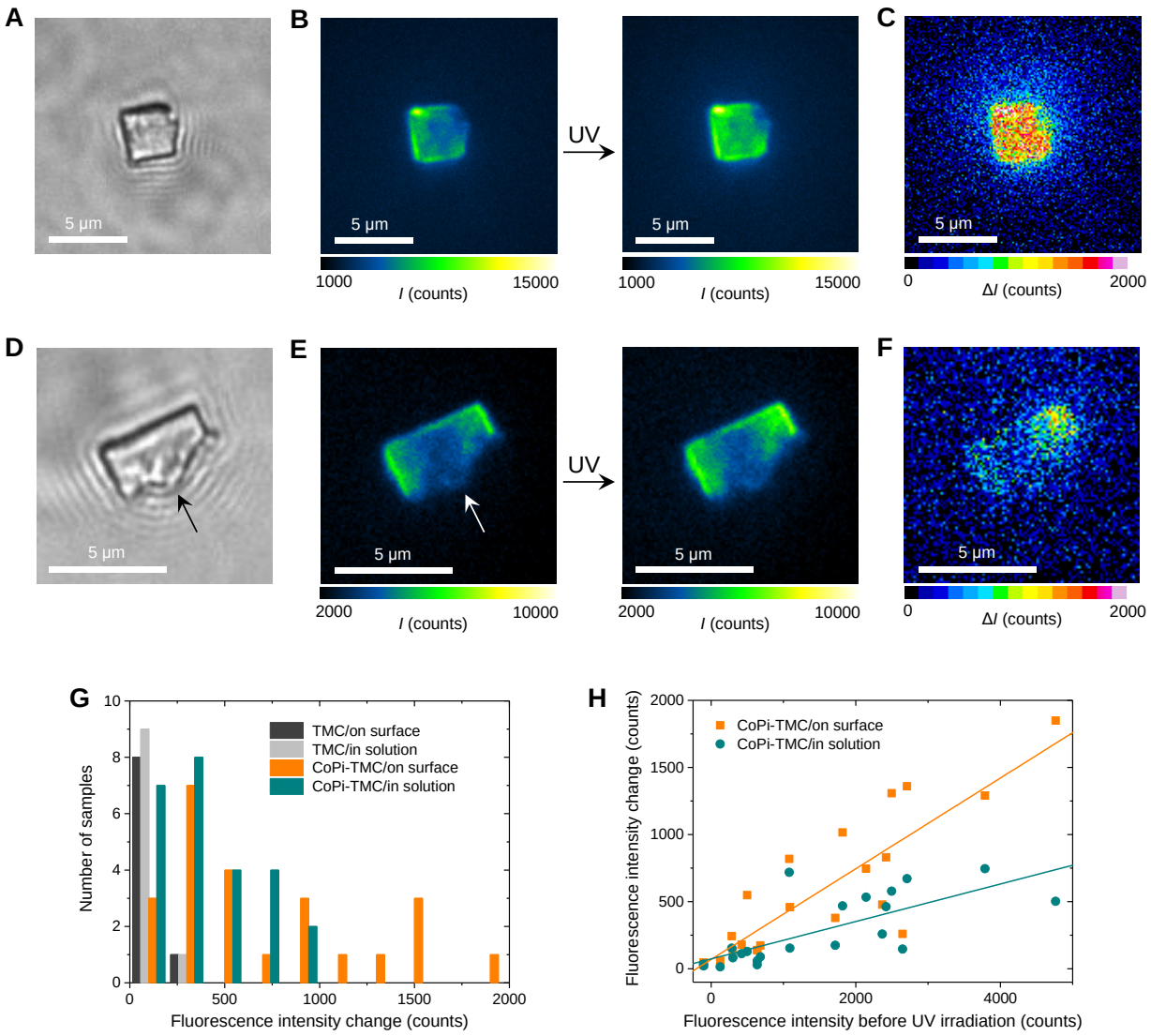

Fig. 8 Optical transmission (A, D) and fluorescence (B, E) images of single CoPi-TMC crystals before and after the UV light irradiation. (C, F) Differential fluorescence images obtained by subtracting the image before the UV light irradiation from the image just after the UV light irradiation. The acquisition time for one frame was 50 ms. (G) Histograms of UV light-induced change in fluorescence intensity measured on the surface of the crystal and in solution at the distance of 1 μm from the edge of the crystal. (H) The relationship between the initial fluorescence intensity and UV light-induced fluorescence intensity change. The background was subtracted from the original data.

4. Conclusion

In summary, the author studied the reaction dynamics of photogenerated charge carriers in CoPi-deposited TMC using ensemble-averaged and single-particle spectroscopies. The combination of CoPi/Pt deposition and the anisotropic electron flow in the superstructure of TMC significantly retarded the charge recombination of h^+ and e^-, resulting in remarkably enhanced photooxidation activity. This is highly beneficial for developing novel photoactive materials for numerous applications, including photocatalysis for water splitting and environmental remediation. In principle, their strategy based on mesocrystal superstructures can be applied to a variety of semiconductor materials and their composites with co-catalysts. However, further efforts are required to assemble the structures in photoelectrochemical cells for water splitting.

5. Reference

(1) Hoffmann, M. R.; Martin, S. T.; Choi, W.; Bahnemann, D. W. *Chem. Rev.* **1995**, *95*, 69.

(2) Hagfeldt, A.; Grätzel, M. *Chem. Rev.* **1995**, *95*, 49.

(3) Walter, M. G.; Warren, E. L.; McKone, J. R.; Boettcher, S. W.; Mi, Q.; Santori, E. A.; Lewis, N. S. *Chem. Rev.* **2010**, *110*, 6446.

(4) Kubacka, A.; Fernández-García, M.; Colón, G. *Chem. Rev.* **2012**, *112*, 1555.

(5) Kudo, A.; Miseki, Y. *Chem. Soc. Rev.* **2009**, *38*, 253.

(6) Chen, X.; Shen, S.; Guo, L.; Mao, S. S. *Chem. Rev.* **2010**, *110*, 6503.

(7) Nakagawa, T.; Bjorge, N. S.; Murray, R. W. *J. Am. Chem. Soc.* **2009**, *131*, 15578.

(8) Tilley, S. D.; Cornuz, M.; Sivula, K.; Grätzel, M. *Angew. Chem., Int. Ed.* **2010**, *49*, 6405.

(9) Abe, R.; Higashi, M.; Domen, K. *J. Am. Chem. Soc.* **2010**, *132*, 11828.

(10) Kay, A.; Cesar, I.; Grätzel, M. *J. Am. Chem. Soc.* **2006**, *128*, 15714.

(11) Steinmiller, E. M. P.; Choi, K.-S. *Proc. Natl. Acad. Sci. U. S. A.* **2009**, *106*, 20633.

(12) Zhong, D. K.; Sun, J.; Inumaru, H.; Gamelin, D. R. *J. Am. Chem. Soc.* **2009**, *131*, 6086.

(13) Fujishima, A.; Rao, T. N.; Tryk, D. A. *J. Photochem. Photobiol., C* **2000**, *1*, 1.

(14) Thompson, T. L.; Yates, J. T., Jr. *Chem. Rev.* **2006**, *106*, 4428.

(15) Chen, X.; Mao, S. S. *Chem. Rev.* **2007**, *107*, 2891.

(16) Diebold, U. *Surf. Sci. Rep.* **2003**, *48*, 53.

(17) Cölfen, H.; Antonietti, M. *Angew. Chem., Int. Ed.* **2005**, *44*, 5576.

(18) Zhou, L.; O'Brien, P. *J. Phys. Chem. Lett.* **2012**, *3*, 620.

(19) Bian, Z.; Tachikawa, T.; Majima, T. *J. Phys. Chem. Lett.* **2012**, *3*, 1422.

(20) Bian, Z.; Tachikawa, T.; Kim, W.; Choi, W.; Majima, T. *J. Phys. Chem. C* **2012**, *116*, 25444.

(21) Kanan, M. W.; Nocera, D. G. *Science* **2008**, *321*, 1072.

(22) Kanan, M. W.; Surendranath, Y.; Nocera, D. G. *Chem. Soc. Rev.* **2009**, *38*, 109.

(23) Khnayzer, R. S.; Mara, M. W.; Huang, J.; Shelby, M. L.; Chen, L. X.; Castellano, F. N. *ACS Catal.* **2012**, *2*, 2150.

(24) Liu, D.; Jing, L.; Luan, P.; Tang, J.; Fu, H. *ACS Appl. Mater. Interfaces*, Ahead of Print.

(25) Klahr, B.; Gimenez, S.; Fabregat-Santiago, F.; Bisquert, J.; Hamann, T. W. *J. Am. Chem. Soc.* **2012**, *134*, 16693.

(26) Zhong, D. K.; Gamelin, D. R. *J. Am. Chem. Soc.* **2010**, *132*, 4202.

(27) Zhong, D. K.; Cornuz, M.; Sivula, K.; Grätzel, M.; Gamelin, D. R. *Energy Environ. Sci.* **2011**, *4*, 1759.

(28) McDonald, K. J.; Choi, K.-S. *Chem. Mater.* **2011**, *23*, 1686.

(29) Seabold, J. A.; Choi, K.-S. *Chem. Mater.* **2011**, *23*, 1105.

(30) Wang, D.; Li, R.; Zhu, J.; Shi, J.; Han, J.; Zong, X.; Li, C. *J. Phys. Chem. C* **2012**, *116*, 5082.

(31) Morris, N. D.; Mallouk, T. E. *J. Am. Chem. Soc.* **2002**, *124*, 11114.

(32) Gerken, J. B.; Chen, J. Y. C.; Masse, R. C.; Powell, A. B.; Stahl, S. S. *Angew. Chem., Int. Ed.* **2012**, *51*, 6676.

(33) Fonseca, C. N. P. d.; Paoli, M.-A. D.; Gorenstein, A. *Sol. Energy Mater. Sol. Cells* **1994**, *33*, 73.

(34) Yoshihara, T.; Katoh, R.; Furube, A.; Tamaki, Y.; Murai, M.; Hara, K.; Murata, S.; Arakawa, H.; Tachiya, M. *J. Phys. Chem. B* **2004**, *108*, 3817.

(35) Tachikawa, T.; Fujitsuka, M.; Majima, T. *J. Phys. Chem. C* **2007**, *111*, 5259.

(36) Cowan, A. J.; Barnett, C. J.; Pendlebury, S. R.; Barroso, M.; Sivula, K.; Grätzel, M.; Durrant, J. R.; Klug, D. R. *J. Am. Chem. Soc.* **2011**, *133*, 10134.

(37) Boschloo, G.; Fitzmaurice, D. *J. Phys. Chem. B* **1999**, *103*, 7860.

(38) Tachikawa, T.; Tojo, S.; Fujitsuka, M.; Sekino, T.; Majima, T. *J. Phys. Chem. B* **2006**, *110*, 14055.

(39) Howe, R. F.; Grätzel, M. *J. Phys. Chem.* **1987**, *91*, 3906.

(40) Micic, O. I.; Zhang, Y.; Cromack, K. R.; Trifunac, A. D.; Thurnauer, M. C. *J. Phys. Chem.* **1993**, *97*, 7277.
(41) Howe, R. F.; Grätzel, M. *J. Phys. Chem.* **1985**, *89*, 4495.
(42) Kumar, C. P.; Gopal, N. O.; Wang, T. C.; Wong, M.-S.; Ke, S. C. *J. Phys. Chem. B* **2006**, *110*, 5223.
(43) McAlpin, J. G.; Surendranath, Y.; Dinca, M.; Stich, T. A.; Stoian, S. A.; Casey, W. H.; Nocera, D. G.; Britt, R. D. *J. Am. Chem. Soc.* **2010**, *132*, 6882.
(44) Duonghong, D.; Ramsden, J.; Grätzel, M. *J. Am. Chem. Soc.* **1982**, *104*, 2977.
(45) Tachikawa, T.; Yamashita, S.; Majima, T. *Angew. Chem., Int. Ed.* **2010**, *49*, 432.
(46) Harriman, A. *J. Phys. Chem.* **1987**, *91*, 6102.
(47) Naito, K.; Tachikawa, T.; Fujitsuka, M.; Majima, T. *J. Am. Chem. Soc.* **2009**, *131*, 934.
(48) Weckhuysen, B. M. *Angew. Chem., Int. Ed.* **2009**, *48*, 4910.
(49) Tachikawa, T.; Majima, T. *Chem. Soc. Rev.* **2010**, *39*, 4802.
(50) Wu, H.-P.; Cheng, T.-L.; Tseng, W.-L. *Langmuir* **2007**, *23*, 7880.
(51) Banks, D. S.; Fradin, C. *Biophys. J.* **2005**, *89*, 2960.

Part 2. Synergetic hydrogen evolution from 3D architectures of TMC with MoS_2 modification

1. Introduction

With mounting concern regarding the reduction of human energy usage and alleviating environmental issues, the efficient utilization of solar energy has become a major research interest over the past few decades. Hydrogen as a renewable resource has been studied extensively in this regard,[1,2] with photocatalysis playing an important role in applications of solar-driven hydrogen evolution since the 1970s.[3] For example, TiO_2 photocatalysts have attracted a great amount of research interest in terms of the hydrogen evolution reaction (HER) because of their strong redox ability, high chemical stability, low toxicity, and abundant availability.[4-6] However, TiO_2 itself showed a poor HER activity even in the presence of sacrificial reagents. In order to promote the HER, robust cocatalysts are usually present on semiconductor materials as active sites.[7-9] Among the noble metals, platinum (Pt) nanoparticles exhibited an efficient HER due to the ideal free energy of hydrogen adsorption.[10-12] However, the

high price and insufficient storage of Pt limit its application in commercial production. Thus, the development of a cocatalyst with low cost and good performance in the HER is strongly motivated in regards to both scientific and engineering interests.

Recently, two-dimensional MoS_2 nanosheets have been extensively investigated and considered as an alternative candidate for the replacement of Pt in efficient HERs.[13,14] MoS_2 forms two different crystal structures: a trigonal prismatic (2H) phase and an octahedral (1T) phase. The increase in the number of active sulfur edge sites on 2H-MoS_2, in preference to inert basal planes, has become essential in the improvement of the reaction efficiency.[15-18] However, semiconducting 2H-MoS_2 is generally combined with additive photosensitizers[19-23] or conductive materials[24-26] to overcome the inherent restriction of poor electrical conductivity. The metallic 1T-MoS_2 showed higher HER rates because of its higher conductivity; however, it was observed that this phase was not thermally stable.[27,28] The author thus conclude that both the photoconductivity and the photocatalytic activity of supporting semiconductor materials are essential for achieving the desired functionality. MoS_2 nanosheets coupled with semiconductor nanoparticles such as TiO_2 have been synthesized and shown to exhibit higher activity in the HER than MoS_2 or TiO_2 alone.[29-33] However, the irregular re-stacking of MoS_2 layers, which potentially reduces the number of active sites, and complicated synthetic procedures (e.g., introduction of graphene as a third component) are disadvantageous for their implementation in practical applications.

In the development of a new class of porous materials, it has recently demonstrated that anatase TiO_2 mesocrystals (TMCs) significantly enhance the charge separation with remarkably long-lived charges (over 4 times), and exhibit excellent photoconductivity (over 10 times) than nanocrystal samples, and even similar photocatalytic activities for organic degradation as commercial P25, which is a benchmark TiO_2 photocatalyst.[34-37] TMCs consist of TiO_2 nanocrystal building blocks and form a well-defined crystal shape. Herein the author reported a new synthetic approach involving the assembly of chemically exfoliated MoS_2 nanosheets as cocatalysts onto external surfaces of TMCs after mild impregnation and annealing. The synergetic HER of MoS_2 supported on TMCs (MoS_2/TMC) exhibited higher activity than in a nanoparticle-based system using P25. It was further revealed by time-resolved diffuse reflectance (TDR) spectroscopy that the higher HER efficiency was promoted by efficient interfacial electron transfer in MoS_2/TMC. The 3D architectures of MoS_2/TMC with promising superiority

are expected to become a potential competitor to earth-abundant catalysts for the HER.

2. Experimental Section

Preparation of MoS_2 Nanosheets. The lithium intercalation was carried out in a nitrogen-filled glovebox ([O_2] < 100 ppm).[38] About 300 mg of bulk MoS_2 (Sigma-Aldrich) was immersed in 3 mL of *n*-butylithium and stirred for 2 days. The stock solution was filtered and washed with 100 mL hexane. Then the semi-dry powder was added in 300 mL of Milli-Q water and ultrasonicated for 1 h. The mixture was centrifugated and washed with Milli-Q water to remove the lithium cation and unexfoliated MoS_2. It was eventually collected and redispersed in Milli-Q water (pH ≈ 6.5). The concentration of MoS_2 in the suspension was determined by inductively coupled plasma (ICP) analysis.

Preparation of Cubic-like TiO_2 Mesocrystals (TMCs). The cubic-like TMCs were synthesized according to references with some modification.[34] The samples were prepared from precursor solutions containing TiF_4 (Sigma-Aldrich), NH_4NO_3 (Wako Pure Chemical Industries), and H_2O. The TiF_4:NH_4NO_3:H_2O molar ratios were 1:4.9:347. The precursor solutions were placed on a silicon wafer to form a thin layer; the temperature was raised at a rate of 10 ℃ min^{-1}, and the products were calcined at 500 ℃ for 2 h. The obtained powders were then calcined at 500 ℃ in an oxygen atmosphere for 8 h to remove surface residues, including fluorine species, completely (confirmed by X-ray photoelectron spectroscopy (XPS)).

Preparation of TMCs Assembled with MoS_2. The preparation method of the MoS_2/TMC composites was described as follows. 2.6 mg TMCs were impregnated with different concentrations of chemically exfoliated MoS_2 nanosheets in 0.7 mL Milli-Q water (pH ≈ 6.5). After sonication, the suspension was dropped on a silicon wafer and annealed for 10 min on an electric heater in the glovebox ([O_2] < 100 ppm). Finally, the product was collected after cooling to room temperature. For the preparation of other reference samples, the same modification procedures were applied for crashed TMCs, P25 (Japan Aerosil), sheet-like TMCs,[S3] and Al_2O_3 nanoparticles (Aldrich; particle size is < 50 nm).

Preparation of Pt Nanoparticle-Loaded TMC (Pt/TMC). Pt/TMC was synthesized according to the literature procedure.[36] TMCs were stirred in water with H_2PtCl_6 (Aldrich) at room temperature and evaporated the water at 100 ℃, and calcined in air at 500 ℃. The amount of Pt was 10 wt%, which was determined by ICP.

Characterizations. The structures of the samples were examined using X-ray diffraction

(XRD; Rigaku, Smartlab; operated at 40 kV and 200 mA, Cu Kα source). The morphologies were investigated using field-emission scanning electron microscopy (FESEM) equipped with EDX analyzer (JEOL, JSM-6330FT) and transmission electron microscopy (TEM) equipped with EDX analyzer (JEOL, JEM 3000F operated at 300 kV or JEM-2100 operated at 200 kV). The Brunauer–Emmett–Teller (BET) surface areas were measured using nitrogen sorption (BEL Japan, BEL-SORP max). The pore volumes and pore diameter distributions were derived from the adsorption isotherms using the Barrett–Joyner–Halenda (BJH) model. The steady-state UV-Vis absorption and diffuse reflectance spectra were measured by UV-Vis-NIR spectrophotometers (Shimadzu, UV-3100 or Jasco, V-570) at room temperature. The concentration of MoS_2 was determined by ICP (Shimadzu, ICPS-8100). The XPS spectral measurements were performed with the PHI X-tool (ULVAC-PHI).

Photocatalytic H_2 Generation Tests. The catalyst of MoS_2/TMC (1 mg) was suspended in 2 mL water with lactic acid (10 vol%) in 10 mL quartz cell and the suspension was shaken for 10 min. Then, the cell was sealed with a rubber septum and purged with Ar gas for 20 min before initiating the irradiation. The sample was irradiated with a UV-LED source (Asahi Spectra, POT-365; 100 mW cm^{-2}) with constant magnetic stirring at room temperature. After the reaction, 0.1 mL of gas was collected from the headspace of the reactor and analyzed using a Shimadzu GC-8A gas chromatograph equipped with an MS-5A column and a thermal conductivity detector. The apparent quantum efficiency (AQE) for hydrogen evolution at each centered wavelength of the monochromatic light with width of ±5 nm (Asahi Spectra, HAL-320; 0.7 mW cm^{-2}) was calculated via the following equation: AQE = (2 × number of number of hydrogen molecules / number of incident photons) × 100%.

Time-Resolved Diffuse Reflectance Measurements. The femtosecond diffuse reflectance spectra were measured by the pump and probe method using a regeneratively amplified titanium sapphire laser (Spectra-Physics, Spitfire Pro F, 1 kHz) pumped by a Nd:YLF laser (Spectra-Physics, Empower 15). The seed pulse was generated by a titanium sapphire laser (Spectra-Physics, Mai Tai VFSJW; fwhm 80 fs). The fourth harmonic generation (330 nm, 3 μJ $pulse^{-1}$) of the optical parametric amplifier (Spectra-Physics, OPA-800CF-1) was used as the excitation pulse. A white light continuum pulse, which was generated by focusing the residual of the fundamental light on a sapphire crystal after the computer controlled optical delay, was divided into two parts and used as the probe and the reference lights, of which the latter was used to

compensate the laser fluctuation. Both probe and reference lights were directed to the sample powder coated on the glass substrate, and the reflected lights were detected by a linear InGaAs array detector equipped with the polychromator (Solar, MS3504). The pump pulse was chopped by the mechanical chopper synchronized to one-half of the laser repetition rate, resulting in a pair of spectra with and without the pump, from which the absorption change (% Abs) induced by the pump pulse was estimated. All measurements were carried out at room temperature.

3. Results and Discussions

The general morphologies of the materials were characterized by field-emission scanning electron microscopy (FESEM) and transmission electron microscopy (TEM). In Fig. 1A, it can be seen that the TMCs, which were newly synthesized via topotactic conversion from precursor NH_4TiOF_3 crystals,[34] display cubic-like morphologies. The author also observed that TMCs with porous structures were composed of an ordered alignment of anatase TiO_2 nanocrystals, with sizes of ~20 nm, as determined from the magnified FESEM image of the crystal surface (insert in Fig. 1A).

The FESEM images of the MoS_2/TMC (Figs. 1B and C) indicate that the structure of the TMCs remains intact after the modification treatment, and the majority of MoS_2 nanosheets are uniformly attached onto the external surfaces of TMCs without considerable aggregation. Although it is not facile to distinguish the existence of MoS_2 nanosheets tiled on the TMCs due to the nm thickness, the elemental mapping analysis proves the distribution of Mo (3.6 wt%) and S (5.2 wt%) elements on the faces of the TMCs, which are consistent with the results of inductively coupled plasma (ICP) analysis. The detailed structures of MoS_2 nanosheets and 3D architectures of MoS_2/TMC were further examined. Fig. 1D shows that the chemically exfoliated MoS_2 moieties are nm-thick sheets with partial overlaps. By atomic force microscopy (AFM), the size and thickness of the MoS_2 monolayer were found to be ~400 nm and ~1.6 nm, respectively.[38] The SAED pattern recorded on exfoliated MoS_2 exhibits a diffraction pattern corresponding to 1T-MoS_2 along the [001] zone axis (Fig. 1E).[27,28] Fig. 1F shows the TEM image of MoS_2/TMC. The high-resolution TEM (HRTEM) analysis clearly reveals that a layered MoS_2 exists at the lateral surface of TMC (Fig. 1G). The lattice spacing, as indicated by two dotted lines in Fig. 1G, was found to be approximately 0.62 nm, thus corresponding to the (002) plane of 2H-MoS_2.[31] Furthermore, a number of folded edges exhibit multi-parallel lines corresponding to two or three layers of MoS_2.

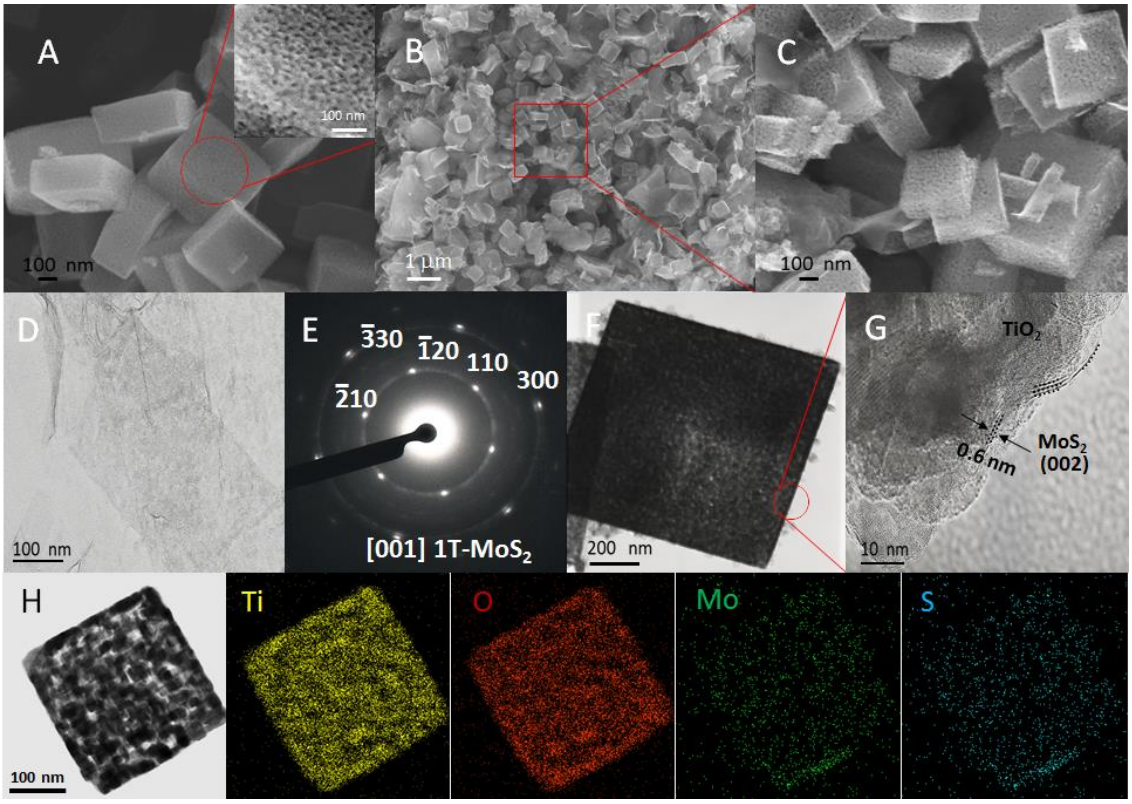

Fig. 1 FESEM images of (A) TMC, (B) MoS_2/TMC, and (C) magnified image of panel B. The inset of panel (A) is the magnified image. TEM image of (D) MoS_2 and its (E) SAED; and (F) MoS_2/TMC and its (G) HRTEM.

The phase identities of the samples were collected using powder X-ray diffraction (XRD), as shown in Fig. 2A. The patterns of all TMCs were comparable with the standard peaks of the anatase phase. For stacked MoS_2 nanosheets on the glass substrate, a detectable diffraction peak was observed at 14.4°, which corresponds to the *c*-plane of stacking MoS_2.[21] The patterns of MoS_2/TMC powders were also characterized and in accordance with each component. The intensities of (002), (100), and (110) diffraction peaks from MoS_2 increased gradually upon increasing the amounts of MoS_2 on the TMCs from 1 wt% to 23 wt%. The nitrogen adsorption-desorption isotherms and the corresponding pore size distribution curves were used to investigate the textural properties of MoS_2, TMC, and MoS_2/TMC. The surface areas of TMC and MoS_2/TMC were calculated to be 62 m^2 g^{-1} and 43 m^2 g^{-1}, respectively, with a similar mean pore size of ~24 nm. After the introduction of MoS_2, there was the slight decrease in surface area due to the presence of partially covered pores on the TMCs.

X-ray photoelectron spectroscopy (XPS) was employed to investigate the phase composition of MoS_2 on TMCs at various annealing temperatures (Fig. 2B). At room temperature, the MoS_2/TMC showed binding energies of Mo $3d_{3/2}$, Mo $3d_{5/2}$, S $2p_{1/2}$, and S $2p_{3/2}$ at 231.2, 228.0, 162.1, and 161.0 eV, respectively.[19] Upon elevating the annealing temperature, the binding energies of Mo 3d and S 2p shifted to higher energies, indicating a phase transition from 1T to 2H,[19] while no difference was observed in Ti 2p and O 1s for the TMCs due to the thermal stability at 500 ℃.

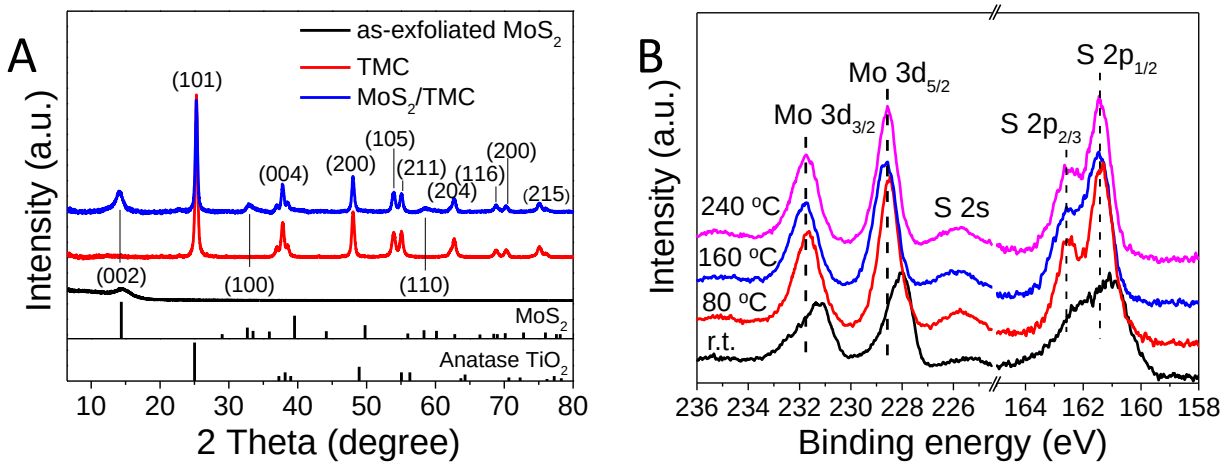

Fig. 2 (A) XRD patterns of MoS_2, TMC, and MoS_2/TMC (10 wt% MoS_2). (B) XPS spectra of MoS_2/TMC (10 wt% MoS_2) powders annealed at a range of temperatures.

The photocatalytic HER was evaluated on MoS_2 (exfoliated MoS_2 and MoS_2/Al_2O_3 annealed at 160 ℃), TMC, and a range of MoS_2/TiO_2 with equal MoS_2 loadings (10 wt%), except in the case of pure TMC. The HER was investigated under UV light irradiation, where lactic acid was used as both a hole scavenger and as an abundant source of H^+ ions (Fig. 3A).[32] A negligible amount of H_2 gas evolution was detected on MoS_2 or TMCs alone. Subsequently, a promising and synergetic improvement in the photocatalytic HER was observed on MoS_2/TMC, with the MoS_2 loading being found to play a crucial role in the HER efficiency. With an increased loading of MoS_2, the HER of MoS_2/TMC was enhanced due to an increase in the number of active sites, to an optimal value of 10 wt%; however, it was also observed that excessive loading lowered the efficiency of MoS_2/TMC, possibly due to the competitive absorption of UV light, and the stacking of MoS_2 monolayers.[39]

They also observed that the HER over MoS_2/TMC was influenced by the annealing temperature. At lower temperatures, a poor physical contact between MoS_2 and TMC resulted, which is disadvantageous to interfacial electron transfer, even though metallic 1T-MoS_2 has a better electrical conductivity. The decrease in activity after annealing at 240 ℃ may be attributed to the disappearance of the 1T phase and/or partial oxidation of active edge sites.

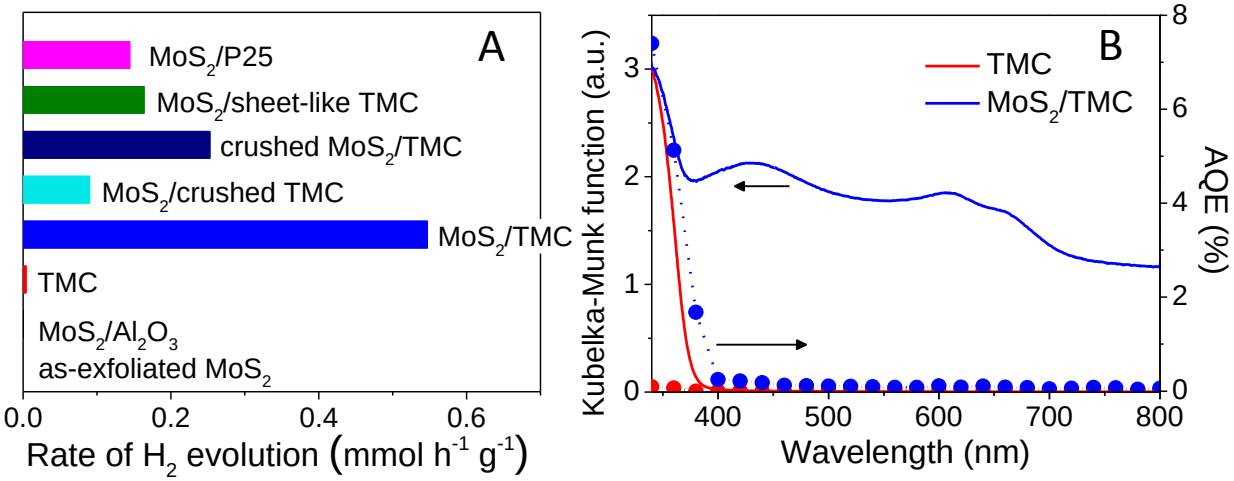

Fig. 3 (A) Comparison of the hydrogen generation rates of different samples. (B) Steady-state diffuse reflectance spectra (left axis, solid lines) and AQE (right axis, symbols with dashed lines) of TMC (red) and MoS_2/TMC (blue).

Under the same conditions, the optimal MoS_2/TMC gives an H_2 evolution rate of 0.55 mmol h^{-1} g^{-1}, which is 4 times greater than that of MoS_2/P25 (0.14 mmol h^{-1} g^{-1}), despite its larger surface area of 51 m^2 g^{-1}. To confirm the impact of mesocrystal superstructures on the HER, they prepared two reference samples, crushed MoS_2/TMC and MoS_2/crushed TMC; in the latter case, TMCs were crushed by grinding with a mortar before modification. As summarized in Fig. 3A, these composites exhibited much lower activity than MoS_2/TMC. The well-aligned nanocrystals on the external surfaces of TMCs form a close contact with the MoS_2 sheets, thus facilitating the electron transfer between the two to efficiently promote the HER. Furthermore, a unique morphological effect was observed; MoS_2/cubic-like TMC appears to be more active than MoS_2/sheet-like TMC. This is likely due to the fact that the lateral surfaces of cubic-like TMCs are dominated by {101} facets, which are in favor of H_2 generation compared to the basal {001} surfaces of sheet-like TMCs.[40-42]

The apparent quantum efficiency (AQE) at each centered wavelength of the monochromatic light was calculated using the following equation: *AQE = (2 × number of H_2 molecules/number of incident photons) × 100%*. Results are shown in Fig. 3B for the UV-visible steady-state diffuse reflectance spectra of the samples tested. The pure TMCs showed negligible H_2 generation in the whole wavelength region tested, due to their intrinsic limitation. On the other hand, MoS_2/TMC evolved H_2 gas, and the action spectrum of AQE was found to be in agreement with the absorption spectrum of TMCs. The AQE reached up to 1.8% at 340 nm and 1.4% at 360 nm. Even though 2H-MoS_2 has an intrinsic visible light absorption, the MoS_2/TMC combination exhibits a poor visible performance due to insufficient charge generation from the excited MoS_2. The stability of MoS_2/TMC was further tested by recycling the catalyst for five times. After 25 h, the catalyst did not show any loss of the activity, indicating its reusability in the photocatalytic reactions. Even though the activity of MoS_2/TMC still falls behind that of Pt nanoparticle-loaded TMC (Pt/TMC) (~1.4 mmol h^{-1} g^{-1}), MoS_2 is considered an ideal alternative to Pt owing to its low cost, its electrochemical stability, and its environmental advantages.

To confirm the fast interfacial electron transfer dynamics within the 3D architectures of MoS_2/TMC, they employed femtosecond TDR spectroscopy. After 330-nm laser excitation of MoS_2/TMC in ambient air, as shown in Fig. 4A, a broad absorption band appeared in the near-infrared region, which was superimposed with trapped and free (or shallowly trapped) electrons in TMCs. Similar absorption spectra were observed for pure TMC, P25, and MoS_2/P25. In the period of 0–10 ps, the transient absorption decayed rapidly when compared with pure TMCs (black lines in Fig. 4B). After 10 ps had passed, the transient absorption diminished gradually. To evaluate the decay kinetics, the time profiles of absorption, probed at 900 nm, were fitted using multi-exponential functions (Fig. 4B), and their lifetimes summarized in Table 1. By modifying TMCs with MoS_2, the lifetimes of the electrons were found to decrease largely to 1.7 ps (49%), 33 ps (32%), and 780 ps (19%) from corresponding time scales of 4.8 ps (23%), 53 ps (41%), and 1070 ps (36%) for pure TMCs. Considering that the transient absorption signal from MoS_2/Al_2O_3 is very weak and decays within 1 ps, it was obvious that interfacial electron transfer could take place between TMCs and MoS_2. The reaction time of electrons was tentatively estimated using the diffusion coefficient of electrons in TiO_2. The mean times required for electron diffusion from a nanocrystal (21 nm × 17 nm) to the neighboring MoS_2 were within tens of picoseconds, which is reasonably consistent with the first (τ_1) and second (τ_2) components.

The third component (τ_3) of MoS_2/TMC is possibly mediated by multiple TiO_2 nanocrystals. The interparticle electron transfer over several hundred nanometers, which corresponds to more than ten nanocrystals, was expected to occur in the microsecond time scale, which is beyond the time window measured here. It is noteworthy that MoS_2/P25 exhibits similar decay times to those of pure P25, except for the fast decay within ~1 ps (~10%), which might be indicative of electron transfer at the interface between TiO_2 and MoS_2. Thus, the well-ordered geometry of TMCs facilitates electron transfer between nanocrystals, resulting in the retardation of the charge recombination, and in efficient electron harvesting by MoS_2. This is likely to be the main reason why MoS_2/TMC exhibits a higher photocatalytic activity (2~5 times) compared to other MoS_2/TiO_2.

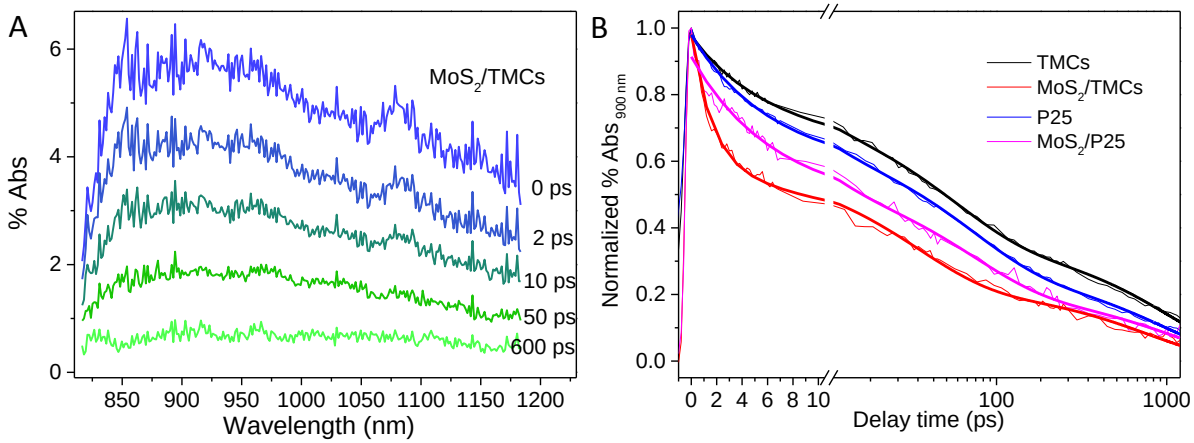

Fig. 4 (A) Time-resolved diffuse reflectance spectra of MoS_2/TMC. (B) Normalized transient absorption traces observed at 900 nm for a range of samples. Bold lines indicate multiexponential curves fitted to kinetic traces.

Table 1. Kinetic Parameters of Transient Absorption Decays

Sample	τ_1 (ps)	τ_2 (ps)	τ_3 (ps)
TMC	5.0 ±0.4 (30%)	55 ±3 (37%)	1100 ±37 (33%)
MoS_2/TMC	1.9 ±0.1 (64%)	36 ±2 (23%)	805 ±53 (13%)
P25	6.0 ±0.3 (38%)	72 ±4 (37%)	1024 ±46 (25%)
MoS_2/P25	7.6 ±0.6 (46%)	91 ±12 (35%)	1372 ±271 (19%)

4. Conclusion

The author decorated the newly designed TMCs with the chemically exfoliated MoS_2 nanosheets by a simple impregnation method. MoS_2/TMC exhibits the high HER rate (0.55 mmol h^{-1} g^{-1}), high AQE (1.8%), and good reusability (over 25 h) under UV light irradiation, without conductive supports such as graphene. To verify the efficient charge separation in MoS_2/TMC, the electron transfer dynamics from the excited TMC to MoS_2 was directly monitored by transient absorption for the first time. This strategy possesses not only a possibility for use of noble-metal-free MoS_2, but also confirms the crucial concept that the hetero-superstructure with the synergy is beneficial for achieving a high photocatalytic activity. It is believed that this concept can be exploited for a range of applications, such as (photo)catalysis, optoelectronics, and energy storage.

5. References

(1) Chen, X.; Shen, S.; Guo, L.; Mao, S. S. *Chem. Rev.* **2010**, *110*, 6503.

(2) Kudo, A.; Miseki, Y.; *Chem. Soc. Rev.* **2009**, *38*, 253.

(3) Fujishima, A.; Honda, K. *Nature* **1972**, *238*, 37.

(4) Ma, Y.; Wang, X.; Jia, Y.; Chen, X.; Han, H.; Li, C. *Chem. Rev.* **2014**, *114*, 9987.

(5) Kapilashrami, M.; Zhang, Y.; Liu, Y. S.; Hagfeldt, A.; Guo, J. *Chem. Rev.* **2014**, *114*, 9662.

(6) Sang,L. X.; Zhao, Y. X.; Burda, C. *Chem. Rev.* **2014**, *114*, 9283.

(7) Yang, J.; Wang, D.; Han, H.; Li, C. *Acc. Chem. Res.* **2013**, *46*, 1900.

(8) Ran, J.; Zhang, J.; Yu, J.; Jaroniec, M.; Qiao, S. *Chem. Soc. Rev.* **2014**, *43*, 7787.

(9) Li, X.; Yu, J.; ;Low, J.; Fang, Y.; Xiao, J.; Chen, X. *J. Mater. Chem. A* **2013**, *3*, 2485.

(10) Trasatti, S. *J. Electroanal. Chem.* **1972**, *39*, 163.

(11) Nørskov, J. K.; Bligaard, T.; Logadottir, A.; Kitchin, J. R.; Chen, J. G.; Pandelov, S.; Stimming, U. *J. Electrochem. Chem.* **2005**, *152*, 23.

(12) Nørskov J. K.; Bligaard, T.; Rossmeisl, J.; Christensen, C. H. *Nat. Chem.* **2009**, *1*, 37.

(13) Chhowalla, M.; Shin, H. S.; Eda, G.; Li, L. J.; Loh, K. P.; Zhang, H. *Nat. Chem.* **2013**, *5*, 263.

(14) Yan, Y.; Xia, B.; Xu, Z.; Wang, X. *ACS Catal.* **2014**, *4*, 1693.

(15) Kanda, S.; Akita, T.; Fujishima, M.; Tada, H. *J. Colloid Interface Sci.* **2011**, *354*, 607.

(16) Zhou, W.; Yin, Z.; Du, Y.; Huang, X.; Zeng, Z.; Fan, Z.; Liu, H. J. Wang, H. Zhang, *Small* **2013**, *9*, 140.

(17) King, L. A.; Zhao, W.; Chhowalla, M.; Riley, D. J.; Eda, G. *J. Mater. Chem. A* **2013**, *1*, 8935.

(18) Liu, C.; Wang, L; Tang, Y.; Luo, S.; Liu, Y.; Zhang, S.; Zeng, Y.; Xu, Y. *Appl. Catal., B*, **2015**, *164*, 1.

(19) Eda, G.; Yamaguchi, H.; Voiry, D.; Fujita, T.; Chen, M.; Chhowalla, M. *Nano Lett.* **2011**, *11*, 5111.

(20) Lukowski, M. A.; Daniel, A. S.; Meng, F.; Forticaux, A.; Li, L.; Jin, S. *J. Am. Chem. Soc.* **2013**, *135*, 10274.

(21) Ding, Q.; Meng, F.; English, C. R.; Cabán-Acevedo, M.; Shearer, M. J.; Liang, D.; Daniel, A. S.; Hamers, R. J.; Jin, S. *J. Am. Chem. Soc.* **2014**, *136*, 8504.

(22) Voiry, D.; Salehi, M.; Silva, R.; Fujita, T.; Chen, M.; Asefa, T.; Shenoy, V. B.; Eda, G.; Chhowalla, M. *Nano Lett.* **2014**, *13*, 6222.

(23) Maitra, U.; Gupta, U.; De, M.; Datta, R.; Govindaraj, A.; Rao, C. N. R. *Angew. Chem., Int. Ed.* **2013**, *52*, 13057.

(24) Hinnemann, B.; Moses, P. G.; Bonde, J.; Jørgensen, K. P.; Nielsen, J. H.; Horch, S.; Chorkendorff, I.; Nørskov, J. K. *J. Am. Chem. Soc.* **2005**, *127*, 5308.

(25) Jaramillo, T. F.; Jørgensen, K. P.; Bonde, J.; Nielsen, J. H.; Horch, S.; Chorkendorff, I. *Science* **2007**, *317*, 100.

(26) Kibsgaard, J.; Chen, Z.; Reinecke, B. N.; Jaramillo, T. F. *Nat. Mater.* **2012**, *11*, 963.

(27) Zong, X.; Na, Y.; Wen, F.; Ma, G.; Yang, J.; Wang, D.; Ma, Y.; Wang, M.; Sun, L.; Li, C. *Chem. Commun.* **2009**, *30*, 4536.

(28) Min, S.; Lu, G. *J. Phys. Chem. C.* **2012**, *116*, 25415.

(29) Li, Y.; Wang, H.; Xie, L.; Liang, Y.; Hong, G.; Dai, H. *J. Am. Chem. Soc.* **2011**, *133*, 7296.

(30) Xiang, Q.; Yu, J.; Jaroniec, M. *J. Am. Chem. Soc.* **2012**, *134*, 6575.

(31) Meng, F.; Li, J.; Cushing, S. K.; Zhi, M.; Wu, N. *J. Am. Chem. Soc.* **2013**, *135*, 10286.

(32) Chang, K.; Mei, Z.; Wang, T.; Kang, Q.; Ouyang, S.; Ye, J. *ACS Nano* **2014**, *8*, 7078.

(33) Xu, J.; Cao, X. *Chem. Eng. J.* **2015**, *260*, 642.

(34) Bian, Z.; Tachikawa, T.; Majima, T. *J. Phys. Chem. Lett.* **2012**, *3*, 1422.

(35) Bian, Z.; Tachikawa, T.; Zhang, P.; Fujitsuka, M.; Majima, T. *J. Am. Chem. Soc.* **2014**, *136*, 458.

(36) Tachikawa, T.; Zhang, P.; Bian, Z.; Majima, T. *J. Mater. Chem. A* **2014**, *2*, 3381.

(37) Bian, Z.; Tachikawa, T.; Zhang, P.; Fujitsuka, M.; Majima, T. *Nat. Commun.* **2014**, *5*:3038.

(38) Chou, S. S.; Kaehr, B.; Kim, J.; Foley, B. M.; De, M.; Hopkins, P. E.; Huang, J.; Brinker, C. J.; Dravid, V. P. *Angew. Chem., Int. Ed.* **2013**, *52*, 4160.

(39) Yu, Y.; Huang, S. Y.; Li, Y.; Steinmann, S. N.; Yang, W.; Cao, L. *Nano Lett.* **2014**, *14*, 553.

(40) Tachikawa, T.; Yamashita, S.; Majima, T. *J. Am. Chem. Soc.* **2011**, *133*, 7197.

(41) Pan, J.; Liu, G.; Lu, G. Q.; Cheng, H. M. *Angew. Chem., Int. Ed.* **2011**, *50*, 2133.

(42) Bian, Z.; Tachikawa, T.; Kim, W.; Choi, W.; Majima, T. *J. Phys. Chem. C* **2012**, *116*, 25444.

Chapter 2. Tunably anisotropic electron flow on specific facet-dominated TMC with photocatalytic selectivity

1. Introduction

Surface science is a critical factor in the equilibrium crystallography and physicochemical performances of semiconductors.[1-4] Anisotropic crystal engineering is an important strategy for tuning and optimizing material reactivities.[5-9] Semiconductor photocatalysts with specific exposed facets exhibit pronounced redox behaviors because of their abundant adsorption sites, efficient separation of photogenerated charges (electrons and holes), and synergism.[10-17] TiO_2 has been widely investigated as a highly active photocatalyst for environmental and energy applications.[18-22] The photocatalytic activity of TiO_2 is dominated by its crystal phase, size, morphology, and surface structure.[23-26] Surface-structure control of the atomic configuration can induce anisotropic crystal growth because of the different surface energies. In the case of anatase TiO_2, the average surface energies of the different facets are 0.90 Jm^{-2} for the (001) facet, 0.53 Jm^{-2} for (100), and 0.44 Jm^{-2} for (101).[27] Based on the Wulff construction, the {001} facet is the most difficult to expose in crystal growth, because its surface energy is high compared with that of the thermodynamically stable {101} facet.[1] However, fluorine-ion capping, which is a pioneering development in the synthesis of anisotropic TiO_2 crystals, can reduce the surface energy and largely expose the {001} facets.[13] As expected, the high-energy {001} facets exhibit higher chemical activities in the degradation of organic pollutants and water splitting.[28-32] Meanwhile, some controversial results suggesting that the activity of the exposed {101} facet for specific reactions is superior to that of the exposed {001} facet have been reported.[33-36] Fundamental mechanistic studies are therefore needed to gain a proper understanding of the photochemical behavior.

Herein the author describes the novel strategies for the synthesis of a series of TiO_2 mesocrystals (TMCs) with different morphologies and explore their photocatalytic performance in pollutant degradation and H_2 evolution from water. Mesocrystals are superstructures with a crystallographically ordered alignment of nanoparticles and are useful for many areas of application owing to their unique characteristics such as a high surface area, pore accessibility, and good electronic conductivity and thermal stability.[37-40] The ratio of the exposed {001} and

{101} TMC facets was successfully controlled using a crystal growth inhibitor (NH_4F). It is suggested that the {101} facets prefer reduction, whereas the {001} facets favor oxidation, because of crystal-facet-dependent surface adsorption and charge transfer. This work will help to gain an in-depth understanding of charge separation within solid catalysts with specific crystal facets, and facilitate construction of more efficient photocatalysts for environmental and energy conversion applications.

2. Experimental Section

Preparation of TMCs with Different Morphologies. TMCs with different morphologies were prepared from precursor solutions containing NH_4F (Wako Pure Chemical Industries), TiF_4 (Sigma-Aldrich), H_2O, NH_4NO_3 (Wako Pure Chemical Industries), and P123 [amphiphilic triblock copolymer, namely $(EO)_{20}(PO)_{70}(EO)_{20}$; Sigma-Aldrich]. The NH_4F:TiF_4:H_2O:NH_4NO_3:P123 molar ratios were *x*:93:32000:453:1. The detailed synthetic procedure and formation mechanism for TMCs have been described elsewhere.[41,42] The obtained samples were denoted by TMC-*n*, where *n* = 1, 2, 3, and 4, representing the TMCs synthesized with *x* (NH_4F) = 0, 46, 116, and 232, respectively. The precursor solutions were placed on a silicon wafer to form a thin layer; the temperature was raised at a rate of 10 ℃ min^{-1}, and the solutions were calcined at 500 ℃ for 2 h. The obtained powders were calcined at 500 ℃ in an oxygen atmosphere for 8 h to remove surface residues, including fluorine species, completely.[43]

Preparation of Pt/TMCs. A photochemical deposition method was used to load 1 wt% Pt nanoparticles on TMCs with different morphologies.[44] In a typical procedure, TMCs (30 mg), Milli-Q ultrapure water (27 mL; Millipore), methanol (3 mL), and a certain amount of H_2PtCl_6 (Aldrich) were mixed to form a homogeneous suspension. The solution was then exposed to ultraviolet (UV) light from a mercury light source (Asahi Spectra, REX-250) for 30 min at room temperature. Finally, the product was collected after centrifugation and dried. The amount of loaded Pt was determined using inductively coupled plasma atomic emission spectroscopy (Shimadzu, ICPS-8100).

Characterization. The crystal structures of the samples were examined using X-ray diffraction (XRD; Rigaku, Smartlab; operated at 40 kV and 200 mA, Cu Kα source). The morphologies were investigated using field-emission scanning electron microscopy (FESEM; JEOL, JSM-6330FT) and transmission electron microscopy (TEM; JEOL, JEM 3000F operated at 300 kV or Hitachi, H-800 operated at 200 kV). The Brunauer–Emmett–Teller (BET) surface

areas were measured using nitrogen sorption (BEL Japan, BEL-SORP max). The pore volumes and pore diameter distributions were derived from the adsorption isotherms, using the Barrett–Joyner–Halenda (BJH) model.

Photocatalytic Degradation Test. For a typical photocatalytic process, TMC dispersions (2 mL) containing 4-chlorophenol (Wako Pure Chemical Industries) (0.1 mM) or $K_2Cr_2O_7$ (Wako Pure Chemical Industries) (0.4 mM) were sonicated for 20 min and then transferred to a quartz cuvette. The photocatalytic reaction was initiated by irradiation with a mercury light source (Asahi Spectra, REX-250) through a filter (centered at 365 nm) at room temperature. After stopping the UV illumination, the sample was centrifuged at 10000 rpm (Hitachi, himac CF16RX) to separate the solid particles. The concentration of unreacted molecules, from which the degradation yield was calculated, was analyzed using a UV-visible-near infrared spectrophotometer (Shimadzu, UV-3100 or UV-3600) at the characteristic wavelength.

Photocatalytic H_2 Generation Test. For UV-induced H_2 production, Pt/TMC (5 mg) was suspended in 5 vol% methanol–water (5 mL). Ar was bubbled through the suspension for 20 min, and then the test tube was sealed with a rubber septum. The test tube was irradiated with a mercury light source (Asahi Spectra, REX-250) through a filter (centered at 365 nm), with magnetic stirring, at room temperature. The intensity of the UV light was approximately 100 mW cm^{-2}. For visible-light H_2 production, Pt/TMC (2.5 mg) was dispersed in 5 mL of an aqueous solution (pH 10, adjusted with NaOH and HCl) of 1 mM eosin Y (EY^{2-}; Nacalai Tesque) and 0.7 M triethanolamine (TEOA; Sigma-Aldrich), or in 5 mL of an aqueous solution (pH 3, adjusted with $HClO_4$) of 10 μM Ruthenizer 470 (Solaronix) and 10 mM ethylenediaminetetraacetic acid (EDTA; Nacalai Tesque). The suspensions were irradiated with visible light (Asahi Spectra, HAL-C100; 400−700 nm, 100 mW cm^{-2}), with magnetic stirring, at room temperature. A 430 nm cutoff filter was used to remove UV light. After the reaction, gas (0.1 mL) was collected from the top of the reactor and analyzed using a Shimadzu GC-8A gas chromatograph equipped with an MS-5A column and a thermal conductivity detector. The surface concentrations of the dye sensitizers were determined from the UV-visible absorption spectra of supernatant solutions separated by centrifugation.

Time-Resolved Diffuse Reflectance Measurements. Ar-saturated acetonitrile slurries containing the catalyst powders (20 g L^{-1}) and N719 ruthenium dye [*cis*-diisothiocyanato-bis(2,2'-bipyridyl-4,4'-dicarboxylato)ruthenium(II) bis(tetrabutylammonium), 1 mM; Solaronix]

were prepared. Time-resolved diffuse reflectance measurements were performed using the second harmonic generation (532 nm, 0.2 mJ pulse^{-1}, 5 ns full-width at half-maximum) from a Q-switched Nd^{3+}:YAG laser (Continuum, Surelite II-10) for excitation, operated with temporal control by a delay generator (Stanford Research Systems, DG535).[43] The reflected analyzing light from a continuous-wave 450 W Xe-arc lamp (Ushio, UXL-451-0) was collected using a focusing lens and directed through a grating monochromator (Nikon, G250) to a silicon avalanche photodiode detector (Hamamatsu Photonics, S5343). The transient signals were amplified with a voltage amplifier (Femto, DHPVA-100) and recorded using a digitizer (Tektronix, DPO3054). All experiments were carried out at room temperature. The percentage absorption (%abs) is given by the equation: %abs = $[(R_0 - R)/R_0] \times 100$, where R and R_0 represent the intensities of the diffuse reflected monitor light with and without excitation, respectively.

3. Results and Discussion

3.1. Synthesis and Structure of Different-Shaped TMCs. The synthesis and structures of different-shaped TMCs are shown in Fig. 1. A thin layer of an aqueous solution containing TiF_4, NH_4NO_3, P123, and NH_4F was dropped on a silicon wafer and calcined at 500 ℃. Intermediate NH_4TiOF_3 crystals were formed during the initial annealing process (<200 ℃).[43,45] During the self-assembly process, the amount of NH_4F added was critical in controlling the size and thickness of the crystal.[41] With increasing annealing temperatures, topotactic transformation occurred from NH_4TiOF_3 to anatase TiO_2. It has been reported that the plate-like mesocrystal superstructures are composed of aligned anatase TiO_2 nanocrystals with dominant {001} facets which lead to efficient charge separation.[42-44,46] When the molar ratio x of NH_4F relative to that of P123 was in the range 0–232, the growth geometry was well ordered along the [101] zone axis, corresponding to TMC-1–4 with different $\{001\}_M/\{101\}_M$ ratios, where M indicates the external surface of a mesocrystal to distinguish it from nanocrystal facets. The TMC morphology gradually became thinner and longer, i.e., the proportion of $\{001\}_M$ surfaces increased and that of $\{101\}_M$ surfaces decreased.

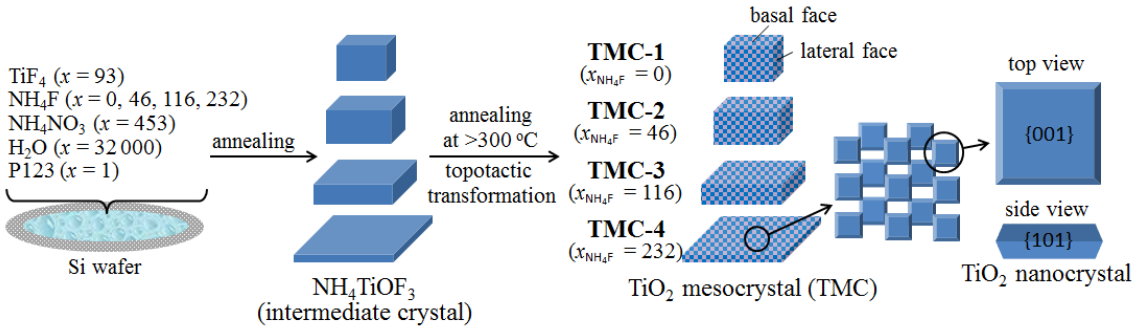

Fig. 1 Schematic illustration of synthesis of different-shaped TMCs.

The low-magnification FESEM images in Fig. 2 show the general morphologies of the as-synthesized TMCs. The TMC shape was changed from cubic to plate-like by varying the molar ratio of NH_4F, although some agglomerates were occasionally observed. As can be seen in Fig. 2A, cubic structures of average thickness ~290 nm and average size ~650 nm were formed in the absence of NH_4F. When a small amount of NH_4F was introduced, the average TMC thickness decreased to ~210 nm, and the average size increased slightly to 880 nm (Fig. 2B). When they continued to increase the NH_4F concentration, the product showed a plate-like morphology, with a thickness of ~140 nm and a size of ~1 μm (Fig. 2C). Eventually, increasing the concentration of NH_4F produced a sheet-like structure with a smaller thickness of ~120 nm and a larger size of ~1.4 μm (Fig. 2D). When they further increased the NH_4F concentration, the TMC sheets merged to form irregular structures, because of the excess area of the {001} surfaces. Based on the gradual changes in the morphology from cubic to plate-like structures, the area ratios of the $\{001\}_M$ surfaces to the $\{101\}_M$ surfaces ($S^M_{\{001\}}/S^M_{\{101\}}$) vary from 1.1 to 5.8 (Table 1). On the other hand, the area ratios of the {001} and {101} facets of TiO_2 nanocrystals in TMCs ($S^N_{\{001\}}/S^N_{\{101\}}$) slightly increased from 0.41 to 0.46 by increasing the amount of NH_4F (Table 1), supporting the explanation that NH_4F mainly controls the shapes of the NH_4TiOF_3 crystals.

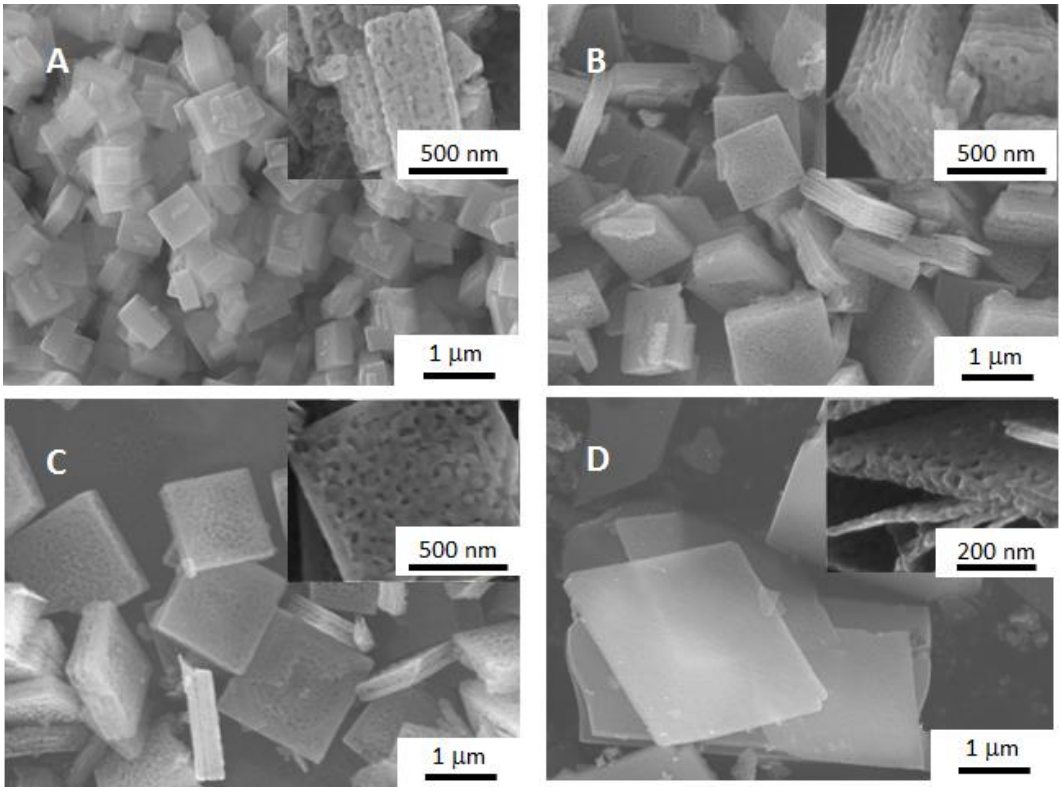

Fig. 2 FESEM images of different-shaped TMCs synthesized with *x* (molar ratio of NH_4F) = 0 (A), 46 (B), 116 (C), and 232 (D). Insets show the high-magnification FESEM images.

Table 1. Structural Characteristics of TiO_2 Mesocrystals (TMCs)

Sample	Thickness, (nm) [a]	Length, (nm) [b]	$S^{M}_{\{001\}}$ / $S^{M}_{\{101\}}$	$I_{(001)}$/ $I_{(004)}$ [c]	Surface area, ($m^2\ g^{-1}$)	Pore volume, ($cm^3\ g^{-1}$)	Pore size, (nm)	Nanocrystal size, (nm) [d]	$S^{N}_{\{001\}}$ / $S^{N}_{\{101\}}$ [e]
TMC-1	290	650	1.1	0.22	92	0.29	11	19 (21)	0.41
TMC-2	210	880	2.1	0.24	96	0.36	11	21 (22)	0.42
TMC-3	140	1000	3.6	0.25	93	0.36	9	24 (21)	0.43
TMC-4	120	1400	5.8	0.44	96	0.36	11	23 (22)	0.46

[a] Face-to-face distance between $\{001\}_M$ TMC facets.
[b] Face-to-face distance between $\{101\}_M$ TMC facets.
[c] Obtained from powder XRD data.
[d] Obtained from TEM analysis. The numbers in parentheses are the nanocrystal size calculated from powder XRD data using the Scherrer equation.
[e] Ratio of surface areas of nanocrystals in TMCs, determined from TEM analysis.

Electron microscope analyses further confirmed the superstructures of the TMC samples. The high-magnification FESEM and TEM images clearly show that the TMCs have a typical porous structure with a pore size of several tens of nanometers (Fig. 3). A selected-area electron diffraction pattern recorded on the TMC shows a diffraction pattern corresponding to single-crystal anatase along the [001] zone axis; this indicates ordered alignment of nanocrystals (inset in Fig. 3B). A photochemical deposition technique was used to prepare Pt-nanoparticle-loaded TMCs.[44] In Figs. 3A and B, a number of Pt nanoparticles (red arrows) are clearly seen on the TMC surfaces. It is worth noting that the Pt nanoparticles are mostly deposited on the lateral faces of the TMCs and the pore wall surfaces; these expose the {101} facets as reductive sites.[46] The preferential deposition of Pt nanoparticles on the {101} facets has previously been observed for anatase TiO_2 nanocrystals.[11,14,44] The size distributions of the Pt nanoparticles deposited on the TMCs are between 1.5 and 3.5 nm, with average diameters of ~2.5 nm.

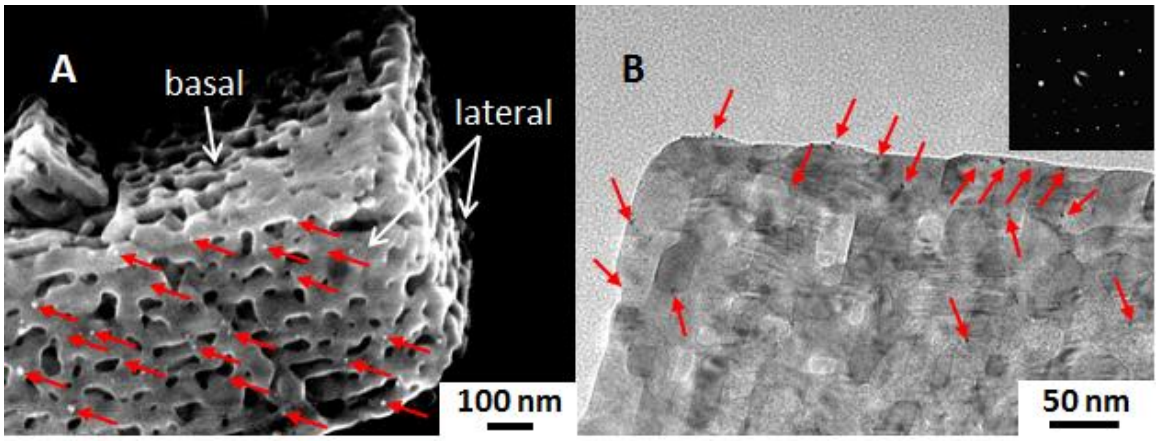

Fig. 3 (A) High-magnification FESEM image of Pt/TMC-1. (B) TEM image of Pt/TMC-4. The red arrows indicate the Pt nanoparticles. Inset in panel (B) indicates the electron diffraction pattern of the selected area.

The powder XRD patterns of as-synthesized TMCs are shown in Fig. 4. All the diffraction peaks are attributable to the anatase phase of TiO_2. There are no obvious differences between the peak positions and peak widths with and without NH_4F. For anatase TiO_2, the detected main peaks at 2θ values of 25.8 °, 37.7 °, and 47.8 ° can be assigned, respectively, to the (101), (004), and (200) planes in the tetragonal anatase phase. The relative ratio of the (004) diffraction peak intensity to that of the (101) peak increased as the NH_4F concentration increased, implying oriented crystal growth along the [101] axis (Table 1). This tendency is in good agreement with

the FESEM results. In addition, the crystallite sizes of TiO_2 estimated from the Scherrer equation are consistent with the TEM observations (Table 1).

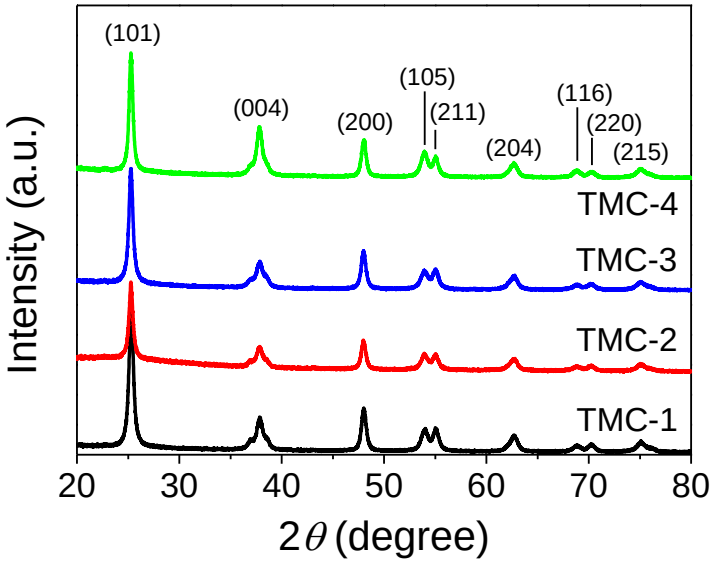

Fig. 4 Powder XRD patterns of TMCs.

Fig. 5 shows the nitrogen adsorption–desorption isotherms and the corresponding pore-size distribution curves (inset) for the TMC samples. All the curves show type IV isotherms and hysteresis loops at high relative pressures, supporting the presence of mesoporous structures. The pore-size distributions in the Fig. 5 inset indicate that all the samples have mesopores with mean sizes of around 10 nm. Furthermore, the BET specific surface areas of the samples are very similar (~90 m^2 g^{-1}) (Table 1), although the sample morphologies are quite different.

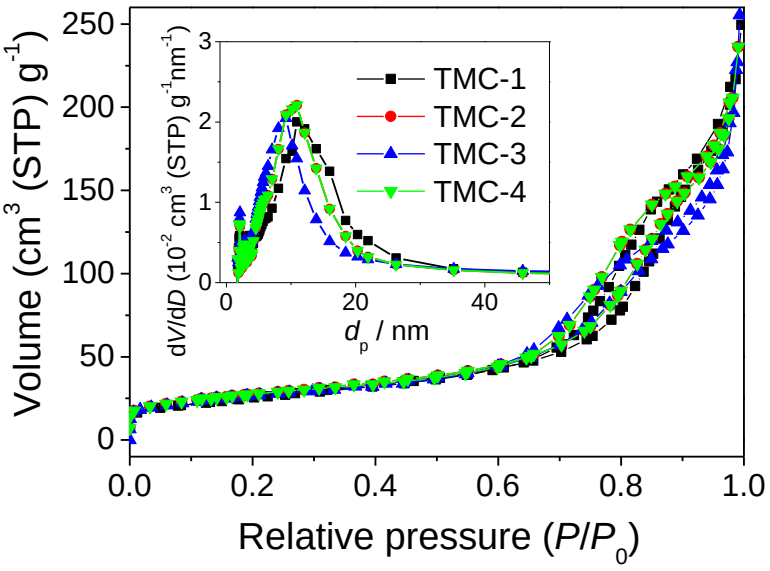

Fig. 5 Nitrogen adsorption-desorption isotherms and pore size distributions (inset) of TMCs.

3.2. Photocatalytic Degradation. The photocatalytic performances of TMCs with different morphologies in the oxidative degradation of 4-chlorophenol, which is a commonly used test compound for photocatalysis,[43] were evaluated. Fig. 6 shows the degradation of 4-chlorophenol under UV-light irradiation, where C_0 and C are the concentrations of 4-chlorophenol before and after UV-light irradiation, respectively. Negligible degradation was observed in the absence of TMCs or UV light. The rate constants for 4-chlorophenol degradation were estimated from the slopes of $\ln(C_0/C)$ vs. irradiation time (inset in Fig. 6) to be 0.021, 0.024, 0.028, and 0.036 min^{-1} for TMC-1–4, respectively. The degradation efficiency clearly increases in proportion to the amount of $\{001\}_M$ surfaces. TMC-4 exhibited the highest activity among the samples tested. This result indicates that the reactive {001} facets play a crucial role in the photodegradation of 4-chlorophenol, possibly because of their strong ability to form hydroxyl radicals.[28]

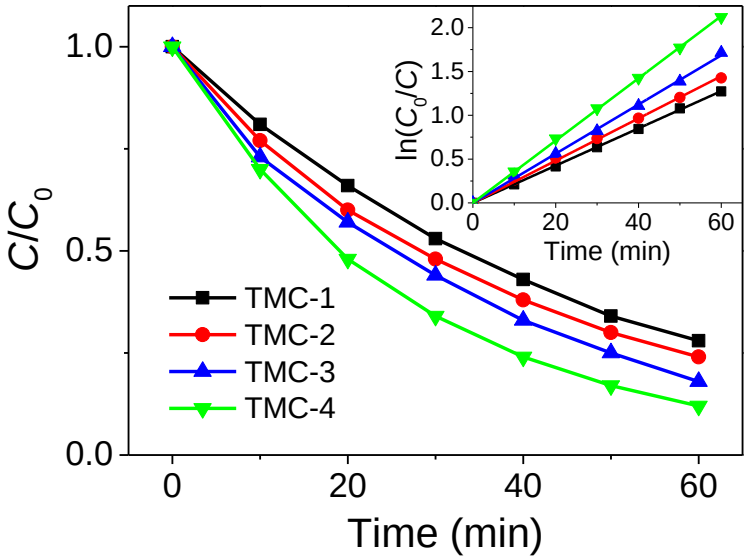

Fig. 6 Photocatalytic degradation of 4-chlorophenol over different TMC samples under UV-light irradiation. C_0 and C are the concentrations of 4-chlorophenol before and after UV-light irradiation, respectively. The experimental conditions were [TMC] = 0.5 g L^{-1}, [4-chlorophenol] = 0.1 mM, pH = 7, λ = 365 nm, I_{UV} = 140 mW cm^{-2}, and air saturation.

To evaluate the TMC performances further, they examined the photocatalytic reduction of Cr^{6+} in the aqueous phase as a probe reaction. The changes in the characteristic absorption bands were monitored to estimate the degradation efficiency. In contrast to oxidative degradation, the activity increased in the order TMC-4 < TMC-3 < TMC-2 < TMC-1, as shown in Fig. 7.

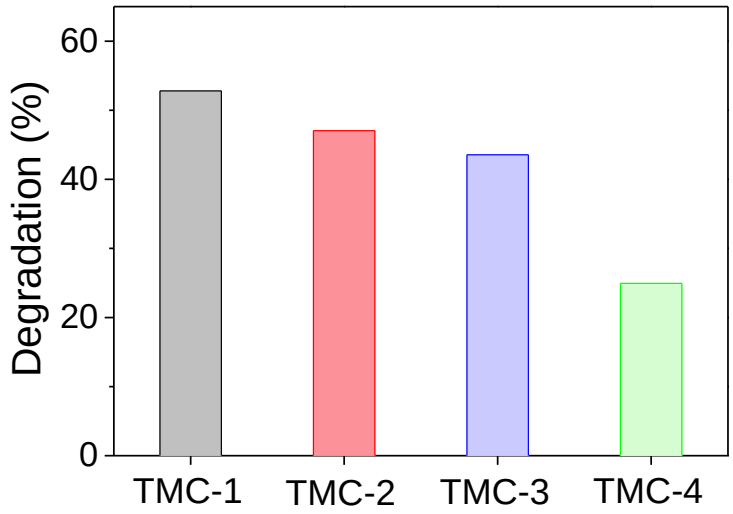

Fig. 7 Photocatalytic degradation of Cr^{6+} in aqueous phase in the presence of different TMC powders. The experimental conditions were [TMC] = 0.4 g L^{-1}, [Cr^{6+}] = 0.4 mM, pH = 3, λ = 365 nm, I_{UV} = 100 mW cm^{-2}, t_{UV} = 2 h, and air saturation.

3.3. Photocatalytic H_2 Evolution under UV-Light Irradiation. As is well known, pure TiO_2 cannot split water effectively to produce H_2 under UV-light irradiation. The reaction efficiency of this process is improved when a Pt cocatalyst and sacrificial electron donor are added to the system.[47,48] The amounts of H_2 evolved during UV-light irradiation of the Pt/TMC powders were measured in aqueous solutions containing methanol as a sacrificial electron donor. Fig. 8 shows the time profiles of H_2 evolution over Pt/TMC samples with different morphologies. Interestingly, the photocatalytic activity increased with decreasing $S^{M}_{\{001\}}/S^{M}_{\{101\}}$; for example, the activity of Pt/TMC-1 was 2.5 times that of Pt/TMC-4. Pan et al.[33] and Gordon et al.[34] reported that TiO_2 nanocrystals with dominant {101} facets produce more H_2 than {001}-faceted crystals do; this is in agreement with the results. It is therefore proposed that following UV-light irradiation, the photogenerated electrons in the conduction band (CB) of TiO_2 migrate from the {001} facet to the {101} facet and are stored in Pt, where they reduce H^+ to generate H_2.[35] Concurrently, the photogenerated holes, which could be preferentially trapped on the {001} facet, oxidize the methanol.

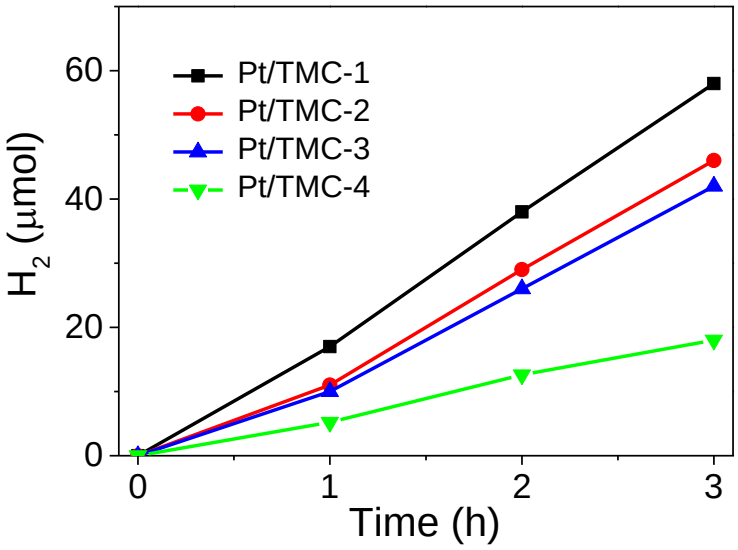

Fig. 8 H_2 evolution during UV-light irradiation of Pt/TMC samples in methanol–water solution. The experimental conditions were [Pt/TMC] = 0.5 g L^{-1}, λ = 365 nm, I_{UV} = 100 mW cm^{-2}, and initial Ar saturation.

3.4. Dye-Sensitized H_2 Evolution under Visible-Light Irradiation. Efficient sunlight harvesting from UV to visible regions is one of the key challenges for practical applications. They thus examine the differences among facet-dominated reactions in dye-sensitized water-splitting systems.[49-54] The efficiency of H_2 evolution in the presence of visible-light-active dye sensitizers is determined by the following factors: (i) surface adsorption of dyes, (ii) interfacial electron transfer from the excited dyes (or reducing dye radical anions) to the CB of TiO_2, and (iii) charge recombination between the oxidized dyes and injected electrons. To investigate factor (i), EY[50] and Ruthenizer 470[49] were used as dye sensitizers for photocatalytic H_2 evolution.

Fig. 9 shows the time dependence of H_2 production during visible-light irradiation of aqueous suspensions of Pt/TMC powders in the presence of EY (its molecular structure is shown in the inset) and TEOA, which was used as a sacrificial electron donor. It is obvious that all the Pt/TMC samples evolved H_2 at the same level as the previously reported one,[50] and their activities increased as $S^{M}_{\{001\}} / S^{M}_{\{101\}}$ decreased.

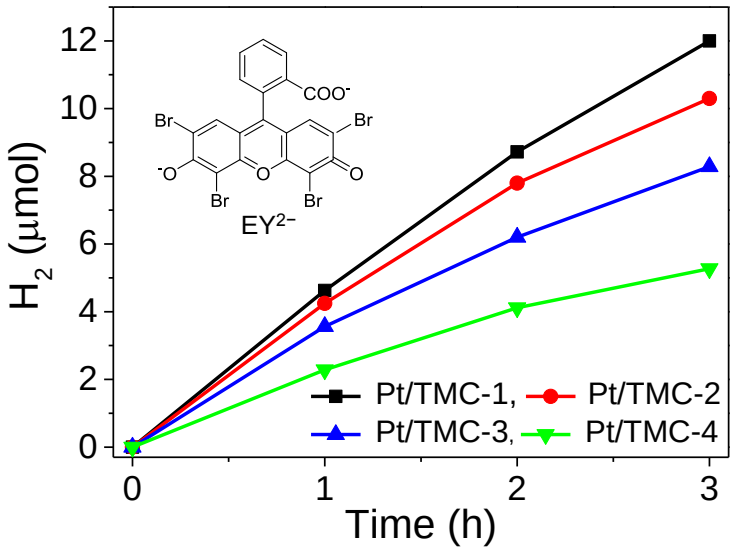

Fig.9 H_2 evolution during visible light irradiation of Pt/TMC powders in aqueous solution (pH 10) containing EY and TEOA. The experimental conditions were [Pt/TMC] = 0.5 g L^{-1}, [EY] = 1 mM, [TEOA] = 0.7 M, pH = 10, λ = 430~700 nm, I_{vis} = 100 mW cm^{-2}, and initial Ar saturation.

The pK_a values for proton dissociation of the hydroxyl and carboxylic groups of EY in water are 2.81 and 3.75, respectively,[55] therefore EY forms a dianion (EY^{2-}) in alkaline solution at pH 10. Anatase TiO_2 nanoparticles have an isoelectric point in the vicinity of pH 6–7,[56] implying that molecular adsorption is strongly inhibited by repulsion between negatively charged TiO_2 and EY^{2-}.[50] In fact, the concentrations of adsorbed EY molecules on the Pt/TMC samples were estimated to be below 1% of the total EY.

The reaction process after photoexcitation of free EY^{2-} in solution is summarized as follows:

$$^{1,3}(EY^{2-})^{*} + TEOA \rightarrow EY^{\bullet 3-} + TEOA^{\bullet +} \quad (1)$$

$$EY^{\bullet 3-} + TiO_2 \rightarrow EY^{2-} + TiO_2(e^{-}) \quad (2)$$

where $^{1,3}(EY^{2-})^{*}$ is the singlet and triplet states of EY^{2-} and $TEOA^{\bullet +}$ is the radical cation of TEOA.[57] Back electron transfer from $EY^{\bullet 3-}$ to $TEOA^{\bullet +}$ would be inhibited because of the rapid degradation of $TEOA^{\bullet +}$. $EY^{\bullet 3-}$, which is generated from reductive quenching by TEOA, ejects an electron to TiO_2 via a collision process. The one-electron reduction potential of EY^{2-} was reported to be −0.80 vs. normal hydrogen electrode (NHE),[58] which is higher than the CB level

(−0.71 V vs. NHE at pH 10) of TiO_2.[59] Reaction (2) is therefore thermodynamically possible. During this key step, electrons are probably preferentially injected into the {101} facet, which has a CB level lower by ca. 0.05–0.1 V than that of the {001} facet.[60,61] Finally, electrons are trapped by Pt and consumed in H^+ reduction. This confirms the significant role of the $\{101\}_M$ facets in determining the reaction efficiency and enables understanding of the activity trend.

Ruthenizer 470 (its molecular structure is shown in the inset in Fig. 10) has six carboxylic groups, which act as efficient anchors on the TiO_2 surface. In the Ruthenizer-470-sensitized Pt/TMC system (pH 3), the excited dye molecules adsorbed on the TMC surface inject electrons into the CB of the TMC as follows:

$$^{1,3}(\text{Ruthenizer 470})_{ad}^{*} + TiO_2 \rightarrow (\text{Ruthenizer 470})^{\bullet+} + TiO_2(e^-) \quad (3)$$

where $^{1,3}(\text{Ruthenizer 470})_{ad}^{*}$ is the singlet and triplet states of Ruthenizer 470 adsorbed on the TiO_2 surface.[49] The sensitizer is regenerated by an electron donor, i.e., EDTA.

As shown in Fig. 10, the visible-light H_2 evolution activity of the Pt/TMC samples increased as $S^{M}_{\{001\}} / S^{M}_{\{101\}}$ increased, in contrast to the EY-sensitized system. The amounts of adsorbed Ruthenizer 470 on the TMC surfaces were estimated to compare the adsorption abilities of the catalysts. It is clearly seen from Fig.11 that the TMC samples with dominant $\{001\}_M$ facets adsorb more dye molecules on their surfaces.

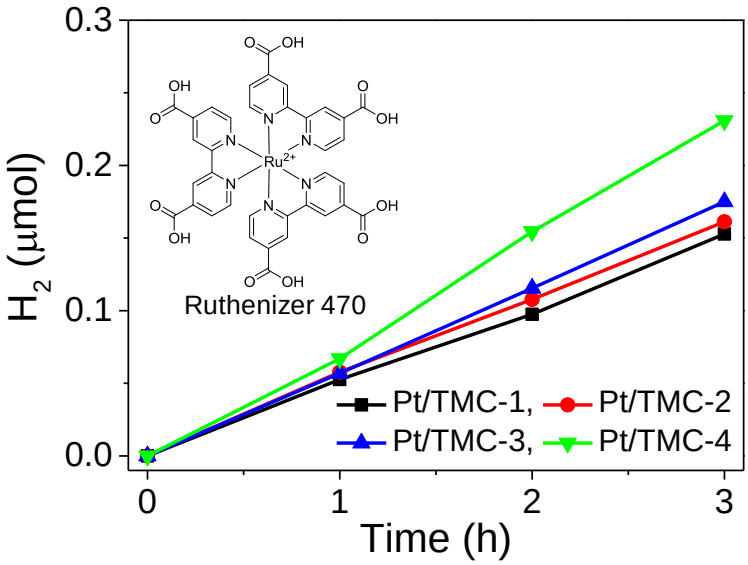

Fig. 10 H_2 evolution during visible-light irradiation of Pt/TMC powders suspended in aqueous solution containing Ruthenizer 470 and EDTA. The experimental conditions were [Pt/TMC] =

0.5 g L^{-1}, [Ruthenizer 470] = 10 μM, [EDTA] = 10 mM, pH = 3, λ = 430~700 nm, I_{vis} = 100 mW cm^{-2}, and initial Ar saturation.

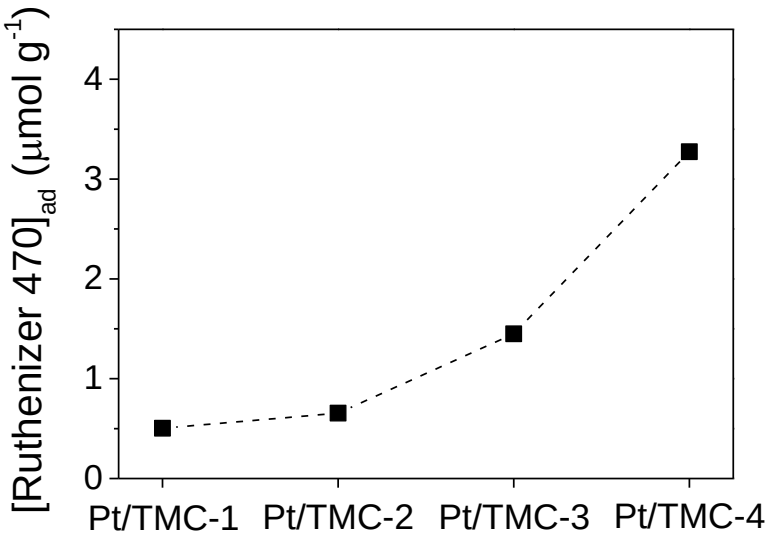

Fig. 11 Adsorption of Ruthenizer 470 on TMC in presence of EDTA in aqueous suspensions of Pt/TMC. [Pt/TMC] = 0.5 g L^{-1}, [Ruthenizer 470] = 10 μM, [EDTA] = 10 mM.

Yu et al. found that the surface concentration (1.43 × 10^{-7} mol cm^{-2}) of N719 dye [*cis*-bis(isothiocyanato)bis(2,2'-bipyridyl-4,4'-dicarboxylato)ruthenium(II) bis(tetrabutylammonium)] adsorbed on TiO_2 nanosheets with dominant {001} facets was slightly lower than that (2.14 × 10^{-7} mol cm^{-2}) on typical anatase nanoparticles in acetonitrile electrolyte solution.[62] Laskova et al. also reported that the surface concentration (0.4–0.5 molecules nm^{-2}) of C101 dye [*cis*-bis(isothiocanate)(4,4'-bis(5-hexylthiophene-2-yl)-2,2'-bipyridine)(4-carboxylic acid-4'-carboxylate-2,2'-bipyridine)ruthenium(II) sodium] was lower on TiO_2 (001) nanosheets than that on TiO_2 (101) nanoparticles (0.7–0.8 molecules nm^{-2}).[63] Recent first-principle theoretical calculations suggested that the observed smaller dye coverage on the {001} facets is a consequence of a partial contact of the thiophene and alkyl bipyridine substituents of C101 with the TiO_2 surface.[61] Compared with those systems, Ruthenizer 470 does not have bulky substituents, and its surface concentrations on the TMC samples are quite low (e.g., 0.023 molecules nm^{-2} for TMC-4). The effect of steric hindrance by TiO_2 and adsorbed molecules is

therefore explicitly ruled out. According to the literature,[64-67] the anatase (001) surface has a strong ability to adsorb hydroxyl and carboxylic groups (as well as water molecules) dissociatively onto the undercoordinated Ti cations. It can therefore be reasonably concluded that the percentage of exposed {001} TMC facets plays an essential role in determining the dye adsorption capability, because the surface areas of the TMC samples are very similar.

3.5. Charge Transfer Dynamics on TMCs. To verify the superior properties of TMCs, the author compared the photocatalytic activities of TMCs synthesized without P123, which have a similar morphology to TMC-4, and anatase TiO_2 nanocrystals (TNCs) with similar surface areas.[43] The TNCs have the truncated bipyramidal morphology and the percentage of exposed TNC {001} facets is similar to that for TMC.[43] As demonstrated in Fig. 12A, Ruthenizer-470-sensitized TMCs could efficiently produce H_2 under visible-light irradiation than Ruthenizer-470-sensitized TNCs did.

Factors (ii) and (iii), mentioned above, were examined. In general, the metal-to-ligand charge transfer excited states of the adsorbed ruthenium dyes have higher energies than the CB of TiO_2, suggesting that this interfacial electron transfer is highly exergonic. The author group recently observed, using time-resolved confocal fluorescence spectroscopy, that the average emission lifetimes of an adsorbed ruthenium dye [*cis*-bis(2,2'-bipyridyl)-(2,2'-bipyridyl-4,4'-dicarboxylic acid)ruthenium(II) hexafluorophosphate] were very similar (~25 ns) for the {001} and {101} facets of anatase TiO_2 crystals in acetonitrile.[68] Based on this result, it can be assumed that the electron injection efficiencies of the {001} and {101} facets are similar.

The injected electrons in TiO_2 either migrate to Pt or recombine with the oxidized dye. The interparticle charge transfer is an important factor that affects the photocatalytic activity in dye-sensitized water-splitting processes,[69-71] because the spatial charge separation at the dye–semiconductor interface greatly retards charge recombination between electrons and oxidized dyes. Time-resolved diffuse reflectance spectroscopy[72,73] was used to explore the dynamics of recombination of the injected electrons in the TMCs and the dye cations. As shown in Fig.12B, the time trace of the transient absorption signal was monitored at 827 nm during 532 nm laser photolysis of TiO_2 powders sensitized with N719 ruthenium dye in Ar-saturated acetonitrile. Electron injection was completed within the laser pulse scattering time (ca. 100 ns) and the accompanying dye cations and injected electrons appeared in the wavelength region above 600 nm (inset in Fig. 12B).[74] The TNC system showed similar spectral features and electron injection

efficiency. The observed time traces were well reproduced using a stretched exponential function:

$$\%\text{abs}\ (t) = (\%\text{abs})_0 \exp[-(t/\tau)^{\alpha}] \quad (4)$$

where $(\%\text{abs})_0$ is the initial absorbance of the dye cations that were generated within the laser pulse (at $t = 0$), τ is the average lifetime, and α is a heterogeneous parameter.[74] The fitting parameters are summarized in Table 2. The τ of the TMC system was about three times that of the TNC system, supporting the idea that efficient electron transport in the mesocrystal superstructure slows down recombination. This result may explain the higher activity observed for Ruthenizer-470-sensitized TMCs. Moreover, the higher α value for the TMC system is possibly attributed to more dispersive recombination dynamics through multiple electron trapping/detrapping processes.

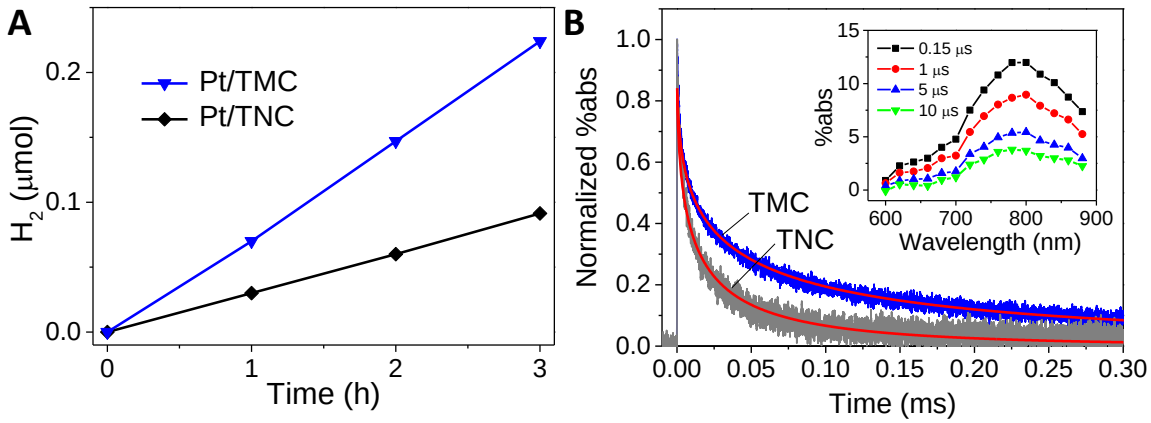

Fig. 12 (A) H_2 evolution during visible-light irradiation of Pt/TMC and Pt/TNC powders suspended in aqueous solutions containing Ruthenizer 470 and EDTA. The experimental conditions were [catalyst] = 0.5 g L^{-1}, [Ruthenizer 470] = 10 μM, [EDTA] = 10 mM, pH = 3, λ = 430~700 nm, I_{vis} = 100 mW cm^{-2}, and initial Ar saturation. (B) Time traces of transient absorption observed at 827 nm during 532 nm laser flash photolysis of acetonitrile suspensions of TMCs and TNCs in the presence of N719 dye. The red lines were obtained using eq 4. Inset shows the time-resolved diffuse reflectance spectra obtained for acetonitrile suspensions containing TMCs and N719 dye.

Table 2. Fitting Parameters for Decay Kinetics

sample	τ (μs)	α
TMC	27	0.37
TNC	10	0.44

3.6. Reaction Mechanisms. The proposed reaction mechanisms of charge transfer on TMCs are illustrated in Fig. 13. In the case of UV excitation (Fig. 13A), the photogenerated electrons are preferentially trapped on the {101} surface through the nanocrystal network in the TMCs, and reduce substances such as Pt precursor and H^+. Because of their high surface energy, the {001} surfaces effectively adsorb water and alcoholic compounds in a dissociative manner, facilitating their oxidation by photogenerated holes and/or hydroxyl radicals (Fig. 6). Reduction seems to occur preferentially on the {101} facets rather than the {001} facets (Fig. 7).

Both the dye-sensitized TMC samples tested here act as visible-light-responsive photocatalysts for H_2 evolution, but the reaction processes are quite different. In the EY-sensitized system (Fig. 13B), the electrons are delivered by freely diffusing $EY^{\bullet 3-}$, which is generated by electron-transfer reactions between $^{1,3}(EY^{2-})^*$ and TEOA. The injected electrons are then transferred to Pt nanoparticles deposited on the TMC {101} facets to produce H_2 (Fig. 9). In contrast, Ruthenizer 470 is more efficiently adsorbed on the {001} facets (Fig. 11), therefore the TMC samples with higher $S^{M}_{\{001\}} / S^{M}_{\{101\}}$ values exhibit higher activities for H_2 production (Fig. 10). The electrons directly injected from the excited dyes can avoid charge recombination with the dye cations remaining on the {001} surface because of efficient migration across the assembled nanocrystals interface and reach the Pt cocatalyst on the {101} surface (Fig. 13C). A similar strategy for achieving efficient charge separation by site-specific modification of sensitizers and cocatalysts was recently used to develop novel plasmonic photocatalysts, where Au and Pt nanoparticles were loaded on the $\{001\}_M$ and $\{101\}_M$ surfaces of TMCs, respectively.[42]

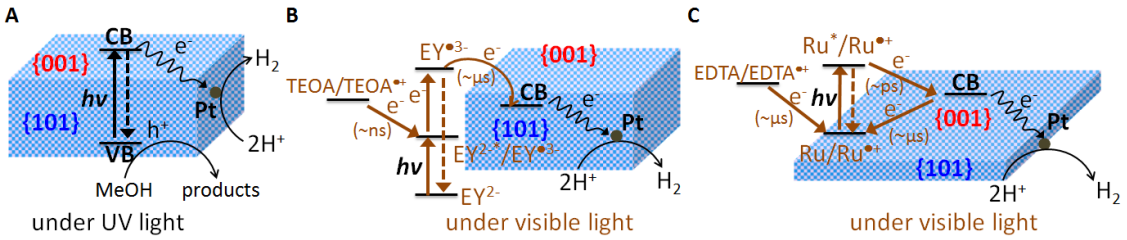

Fig. 13 H_2 evolution during (A) UV-light irradiation of Pt/TMC in methanol–water solution, (B) visible-light irradiation of Pt/TMC in aqueous solution (pH 10) containing EY and TEOA, and (C) visible light irradiation of Pt/TMC in aqueous solution (pH 3) containing Ruthenizer 470 and EDTA. VB is valence band of TiO_2. Ru is adsorbed Ruthenizer 470. Typical time scales for electron transfer[57,74-76] are shown below the arrows.

4. Conclusiton

In summary, the author developed a novel strategy for synthesizing a series of TiO_2 mesocrystals with desired crystal structures. It was found that mesocrystals with different facet ratios showed different reactivity orders in photo-oxidation, i.e., $\{001\}_M > \{101\}_M$, and photoreduction, i.e., $\{101\}_M > \{001\}_M$, under UV-light irradiation, similar to those observed in conventional nanocrystal systems. Furthermore, the author examined the visible-light photocatalytic activities of mesocrystals with different morphologies, using EY and ruthenium dyes as sensitizers. It was confirmed that the $\{001\}_M$ facets are preferred for molecular adsorption and electron injection from the photoexcited dye sensitizers to the CB of TiO_2, whereas the $\{101\}_M$ facets are efficient for the collection of photogenerated electrons, owing to directional electron flow. These findings highlight that the concept of crystal-facet-dependent photocatalytic reactions can be extended to superstructure systems with well-regulated morphologies. The synergetic effect of crystal-facet engineering and nanocrystal arrangements will significantly improve the efficiencies and selectivities of semiconductor photocatalysts.

5. Reference

(1) Diebold, U. *Surf. Sci. Rep.* **2003**, *48*, 53.

(2) Thompson, T. L.; Yates, J. T., Jr. *Chem. Rev.* **2006**, *106*, 4428.

(3) Somorjai, G. A.; Frei, H.; Park, J. Y. *J. Am. Chem. Soc.* **2009**, *131*, 16589.

(4) Henderson, M. A. *Surf. Sci. Rep.* **2011**, *66*, 185.

(5) Yin, Y.; Alivisatos, A. P. *Nature* **2005**, *437*, 664.

(6) Jun, Y.-w.; Choi, J.-s.; Cheon, J. *Angew. Chem., Int. Ed.* **2006**, *45*, 3414.

(7) Xia, Y.; Xiong, Y.; Lim, B.; Skrabalak, S. E. *Angew. Chem., Int. Ed.* **2009**, *48*, 60.

(8) Liu, G.; Yu, J. C.; Lu, G. Q.; Cheng, H.-M. *Chem. Commun.* **2011**, *47*, 6763.

(9) Kuang, Q.; Wang, X.; Jiang, Z.; Xie, Z.; Zheng, L. *Acc. Chem. Res.* **2014**, *47*, 308.

(10) Giocondi, J. L.; Rohrer, G. S. *J. Phys. Chem. B* **2001**, *105*, 8275.

(11) Ohno, T.; Sarukawa, K.; Matsumura, M. *New J. Chem.* **2002**, *26*, 1167.

(12) Giocondi, J. L.; Salvador, P. A.; Rohrer, G. S. *Top. Catal.* **2007**, *44*, 529.

(13) Yang, H. G.; Sun, C. H.; Qiao, S. Z.; Zou, J.; Liu, G.; Smith, S. C.; Cheng, H. M.; Lu, G. Q. *Nature* **2008**, *453*, 638.

(14) Murakami, N.; Kurihara, Y.; Tsubota, T.; Ohno, T. *J. Phys. Chem. C* **2009**, *113*, 3062.

(15) Zheng, Z.; Huang, B.; Lu, J.; Qin, X.; Zhang, X.; Dai, Y. *Chem. - Eur. J.* **2011**, *17*, 15032.

(16) Li, R.; Zhang, F.; Wang, D.; Yang, J.; Li, M.; Zhu, J.; Zhou, X.; Han, H.; Li, C. *Nat. Commun.* **2013**, *4*,2401.

(17) Liu, C.; Han, X.; Xie, S.; Kuang, Q.; Wang, X.; Jin, M.; Xie, Z.; Zheng, L. *Chem. - Asian J.* **2013**, *8*, 282.

(18) Fujishima, A.; Zhang, X.; Tryk, D. A. *Surf. Sci. Rep.* **2008**, *63*, 515.

(19) Hoffmann, M. R.; Martin, S. T.; Choi, W.; Bahnemann, D. W. *Chem. Rev.* **1995**, *95*, 69.

(20) Carp, O.; Huisman, C. L.; Reller, A. *Prog. Solid State Chem.* **2004**, *32*, 33.

(21) Chen, X.; Mao, S. S. *Chem. Rev.* **2007**, *107*, 2891.

(22) Froeschl, T.; Hoermann, U.; Kubiak, P.; Kucerova, G.; Pfanzelt, M.; Weiss, C. K.; Behm, R. J.; Huesing, N.; Kaiser, U.; Landfester, K.; Wohlfahrt-Mehrens, M. *Chem. Soc. Rev.* **2012**, *41*, 5313.

(23) Ohtani, B.; Ogawa, Y.; Nishimoto, S.-i. *J. Phys. Chem. B* **1997**, *101*, 3746.

(24) Lin, H.; Huang, C. P.; Li, W.; Ni, C.; Shah, S. I.; Tseng, Y.-H. *Appl. Catal., B* **2006**, *68*, 1.

(25) Tachikawa, T.; Tojo, S.; Fujitsuka, M.; Sekino, T.; Majima, T. *J. Phys. Chem. B* **2006**, *110*, 14055.

(26) Yang, D.; Liu, H.; Zheng, Z.; Yuan, Y.; Zhao, J.-c.; Waclawik, E. R.; Ke, X.; Zhu, H. *J. Am. Chem. Soc.* **2009**, *131*, 17885.

(27) Lazzeri, M.; Vittadini, A.; Selloni, A. *Phys. Rev. B Condens. Matter Mater. Phys.* **2002**, *65*, 119901.

(28) Yang, H. G.; Liu, G.; Qiao, S. Z.; Sun, C. H.; Jin, Y. G.; Smith, S. C.; Zou, J.; Cheng, H. M.; Lu, G. Q. *J. Am. Chem. Soc.* **2009**, *131*, 4078.

(29) Liu, G.; Yang, H.-G.; Wang, X.-W.; Cheng, L.; Lu, H.-F.; Wang, L.-Z.; Lu, G.-Q.; Cheng, H.-M. *J. Phys. Chem. C* **2009**, *113*, 21784.

(30) Zhang, D.; Li, G.; Yang, X.; Yu, J. C. *Chem. Commun.* **2009**, 4381.

(31) Ma, X. Y.; Chen, Z. G.; Hartono, S. B.; Jiang, H. B.; Zou, J.; Qiao, S. Z.; Yang, H. G. *Chem. Commun.* **2010**, *46*, 6608.

(32) Wen, C. Z.; Zhou, J. Z.; Jiang, H. B.; Hu, Q. H.; Qiao, S. Z.; Yang, H. G. *Chem. Commun.* **2011**, *47*, 4400.

(33) Pan, J.; Liu, G.; Lu, G. Q.; Cheng, H.-M. *Angew. Chem., Int. Ed.* **2011**, *50*, 2133.

(34) Gordon, T. R.; Cargnello, M.; Paik, T.; Mangolini, F.; Weber, R. T.; Fornasiero, P.; Murray, C. B. *J. Am. Chem. Soc.* **2012**, *134*, 6751.

(35) Tachikawa, T.; Yamashita, S.; Majima, T. *J. Am. Chem. Soc.* **2011**, *133*, 7197.

(36) D'Arienzo, M.; Carbajo, J.; Bahamonde, A.; Crippa, M.; Polizzi, S.; Scotti, R.; Wahba, L.; Morazzoni, F. *J. Am. Chem. Soc.* **2011**, *133*, 17652.

(37) Cölfen, H.; Antonietti, M. *Angew. Chem., Int. Ed.* **2005**, *44*, 5576.

(38) Song, R.-Q.; Cölfen, H. *Adv. Mater.* **2010**, *22*, 1301.

(39) Zhou, L.; O'Brien, P. *Small* **2008**, *4*, 1566.

(40) Fang, J.; Ding, B.; Gleiter, H. *Chem. Soc. Rev.* **2011**, *40*, 5347.

(41) Bian, Z.; Tachikawa, T.; Zhang, P.; Fujitsuka, M.; Majima, T. *Nat. Commun.* **2014**, *5*, 4038.

(42) Bian, Z.; Tachikawa, T.; Zhang, P.; Fujitsuka, M.; Majima, T. *J. Am. Chem. Soc.* **2014**, *136*, 458.

(43) Bian, Z.; Tachikawa, T.; Majima, T. *J. Phys. Chem. Lett.* **2012**, *3*, 1422.

(44) Bian, Z.; Tachikawa, T.; Kim, W.; Choi, W.; Majima, T. *J. Phys. Chem. C* **2012**, *116*, 25444.

(45) Zhou, L.; Smyth-Boyle, D.; O'Brien, P. *J. Am. Chem. Soc.* **2008**, *130*, 1309.

(46) Tachikawa, T.; Zhang, P.; Bian, Z.; Majima, T. *J. Mater. Chem. A* **2014**, *2*, 3381.

(47) Sato, S.; White, J. M. *Chem. Phys. Lett.* **1980**, *72*, 83.

(48) Tabata, S.; Nishida, H.; Masaki, Y.; Tabata, K. *Catal. Lett.* **1995**, *34*, 245.

(49) Bae, E.; Choi, W. *J. Phys. Chem. B* **2006**, *110*, 14792.

(50) Choi, S. K.; Kim, S.; Ryu, J.; Lim, S. K.; Park, H. *Photochem. Photobiol. Sci.* **2012**, *11*, 1437.

(51) Maitani, M. M.; Zhan, C.; Mochizuki, D.; Suzuki, E.; Wada, Y. *Catal. Sci. Technol.* **2014**, *4*, 871.

(52) Walter, M. G.; Warren, E. L.; McKone, J. R.; Boettcher, S. W.; Mi, Q.; Santori, E. A.; Lewis, N. S. *Chem. Rev.* **2010**, *110*, 6446.

(53) Kudo, A.; Miseki, Y. *Chem. Soc. Rev.* **2009**, *38*, 253.

(54) Chen, X.; Shen, S.; Guo, L.; Mao, S. S. *Chem. Rev.* **2010**, *110*, 6503.

(55) McHedlov-Petrossyan, N. O.; Kukhtik, V. I.; Bezugliy, V. D. *J. Phys. Org. Chem.* **2003**, *16*, 380.

(56) French, R. A.; Jacobson, A. R.; Kim, B.; Isley, S. L.; Penn, R. L.; Baveye, P. C. *Environ. Sci. Technol.* **2009**, *43*, 1354.

(57) Islam, S. D. M.; Konishi, T.; Fujitsuka, M.; Ito, O.; Nakamura, Y.; Usui, Y. *Photochem. Photobiol.* **2000**, *71*, 675.

(58) Zhang, J.; Sun, L.; Yoshida, T. *J. Electroanal. Chem.* **2011**, *662*, 384.

(59) Duonghong, D.; Ramsden, J.; Grätzel, M. *J. Am. Chem. Soc.* **1982**, *104*, 2977.

(60) Hengerer, R.; Kavan, L.; Krtil, P.; Grätzel, M. *J. Electrochem. Soc.* **2000**, *147*, 1467.

(61) De Angelis, F.; Vitillaro, G.; Kavan, L.; Nazeeruddin, M. K.; Grätzel, M. *J. Phys. Chem. C* **2012**, *116*, 18124.

(62) Yu, J.; Fan, J.; Lv, K. *Nanoscale* **2010**, *2*, 2144.

(63) Laskova, B.; Zukalova, M.; Kavan, L.; Chou, A.; Liska, P.; Wei, Z.; Bin, L.; Kubat, P.; Ghadiri, E.; Moser, J. E.; Grätzel, M. *J. Solid State Electrochem.* **2012**, *16*, 2993.

(64) Gong, X.-Q.; Selloni, A. *J. Phys. Chem. B* **2005**, *109*, 19560.

(65) Tanner, R. E.; Sasahara, A.; Liang, Y.; Altman, E. I.; Onishi, H. *J. Phys. Chem. B* **2002**, *106*, 8211.

(66) Gong, X.-Q.; Selloni, A.; Vittadini, A. *J. Phys. Chem. B* **2006**, *110*, 2804.

(67) Vittadini, A.; Selloni, A.; Rotzinger, F. P.; Grätzel, M. *Phys. Rev. Lett.* **1998**, *81*, 2954.

(68) Tachikawa, T.; Majima, T. *Chem. Commun.* **2012**, *48*, 3300.

(69) Lakshminarasimhan, N.; Bae, E.; Choi, W. *J. Phys. Chem. C* **2007**, *111*, 15244.

(70) Lakshminarasimhan, N.; Kim, W.; Choi, W. *J. Phys. Chem. C* **2008**, *112*, 20451.

(71) Choi, S. K.; Kim, S.; Lim, S. K.; Park, H. *J. Phys. Chem. C* **2010**, *114*, 16475.

(72) Tachikawa, T.; Fujitsuka, M.; Majima, T. *J. Phys. Chem. C* **2007**, *111*, 5259.

(73) Kim, W.; Tachikawa, T.; Majima, T.; Choi, W. *J. Phys. Chem. C* **2009**, *113*, 10603.

(74) Clifford, J. N.; Palomares, E.; Nazeeruddin, M. K.; Grätzel, M.; Nelson, J.; Li, X.; Long, N. J.; Durrant, J. R. *J. Am. Chem. Soc.* **2004**, *126*, 5225.

(75) Kim, W.; Tachikawa, T.; Majima, T.; Li, C.; Kim, H.-J.; Choi, W. *Energy Environ. Sci.* **2010**, *3*, 1789.

(76) Benkoe, G.; Kallioinen, J.; Korppi-Tommola, J. E. I.; Yartsev, A. P.; Sundstroem, V. *J. Am. Chem. Soc.* **2002**, *124*, 489.

Chapter 3: In situ topotactic transformation confined doping into TMC with visible-light activation

Part 1. n-type F-doping on TMC for efficient visible-light driven photocatalytic hydrogen generation

1. Introduction

It is a central theme in nanoscience to develop efficient metal oxide semiconductors for versatile applications in photocatalysis, photovoltaics, batteries, and sensors.[1-7] Titanium dioxide (TiO_2) is one of the most intensively studied semiconductors due to its strong redox ability, high chemical stability, low toxicity, and abundant availability.[8,9] As photocatalytic materials since 1972,[10] TiO_2 represents limitations in widespread applications of photovoltaics and photo(electro)catalysis inevitably due to its wide band gap and low quantum efficiency.[11-14] The nanomaterials based on structure-performance relationship have been developed to significantly improve the quantum efficiency of photocatalysis. As a new class of porous materials, TiO_2 mesocrystal (TMC) with the superstructure exhibits excellent photocatalytic activities than conventional TiO_2 nanocrystals and commercial P25.[15-19] It was further revealed that the long-range ordered mesocrystal superstructures significantly retard the recombination of electron-hole pairs due to efficient interparticle charge transfer.[18-21] Therefore, it is strongly required to extend the absorption of TMCs into the visible region for effectively utilizing the solar energy with practical functions.[21,22] In addition, it still remains a challenge to facilely synthesize TMCs with higher visible-light activity in research fields.

In order to activate TiO_2 under the visible-light irradiation, many efforts have attempted to create a midgap energy state or to narrow the intrinsic band gap over the past decades.[23,24] From the experimental and theoretical results, the incorporation of dopants to the TiO_2 structures cannot show effective photoactivity, inevitably ascribed to increase the rate of undesired charge recombination.[25] Even in this case, the moderate doping methods always improve their photocatalytic activity than pure TiO_2.[26] The dopant incorporation often accompanies an oxygen vacancy (V_o), which is known to affect the charge transfer dynamics in photocatalysis.[15] On the contrary, the substitution of an oxygen with a fluorine (F) atom is the alternative way as a n-type doping with Ti^{3+} to improve the efficiency.[27-29] Recently, the extended series of phase doped TiO_2

with promising performance, such as NH_4F and HF doping, have attracted increasing attention of researchers.[26,30] Attributed to covalent interaction between F and Ti, titanium oxydifluoride ($TiOF_2$) was proposed as a F-dopant source to obtain a visible-light photocatalyst for dye degradation.[31,32] To date, many attentions have been paid to ideally fabricate the hierarchical TiO_2 from the original $TiOF_2$ via in situ transformation.[33-35] It was found that the stability of reactive {001}[18,22] facet and crystallization can be improved after F species was introduced from $TiOF_2$.[36] How can achieve the n-type F-doping with higher contents of F into TMC during the topotactic transformation and understand the formation mechanisms? To the best of our knowledge, the details of oriented transformation of TMC and its compatibility with n-type F-doping have not been reported until now.

Herein the author reported the incorporation of $TiOF_2$ as n-type F-dopant source to TMCs during the topotactic transformation along with efficient visible-light driven H_2 generation for the first time. The oriented transformation of TMC such as crystal growth, phase transition, and morphologic change was monitored via in situ temperature-dependent techniques. The dynamics of charge separation and trapping were investigated by the means of time-resolved transient absorption measurement to clarify the impact of n-type F-doping into TMC. The results are discussed with comparison to their photocatalytic efficiency for n-type F-doped TMC. It is suggested that surface potential and hydrophilicity are changed by the F-doping, indicating the higher photocatalytic activity for n-type F-doped TMC. The results are discussed with comparison to the photocatalytic efficiency for TMC and F-doped TMC.

2. Experimental Section

Materials. Titanium(IV) fluoride and chloroplatinic acid were purchased from Sigma-Aldrich. Ammonium nitrate, ammonium fluoride, boric acid and lactic acid were purchased from Wako Pure Chemical Industries. All of these chemicals were analytical grade and used as received.

Preparation of TMC and F-doped TMC. The samples were synthesized according to former reports.[18,22] A precursor solution containing TiF_4, H_2O, NH_4NO_3, and NH_4F (molar ratio= 1:117:6.6:4) was prepared, and were placed on a silicon wafer to form a thin layer with the thickness around 2~3 mm. It was calcined in air using a heating rate of 10 $^oC\ min^{-1}$ at different temperatures for 2 h. The annealed samples were collected and designed as Tx, in which the x represents the annealing temperatures. As a controllable reference, the obtained samples (T500) were calcined in pure oxygen atmosphere at 600 ^oC for 4 h to remove surface residue and control

the F-doped amount, which was referred as T500-O_2.

Preparation of Pt/TMC and F-doped TMC. A loading of 1 wt % Pt nanoparticles was photochemical deposited on TMC and F-doped TMC.[20] In a typical procedure, 30 mg TMC or F-doped TMC, 27 mL of Milli-Q ultrapure water (Millipore), 3 mL methanol, and a certain amount H_2PtCl_6 were mixed to form a homogeneous suspension. The solutions were then exposed to the visible light from a mercury light source (Asahi Spectra, REX-250) for 30 min at room temperature. After centrifugation and dried, the products were collected and subsequently calcined in air at 300 ^oC for 30 min. The amounts of loaded Pt were determined by inductively coupled plasma emission spectroscopy (Shimadzu, ICPS-8100).

Characterization. The structures of the samples were examined using in situ powder X-ray diffraction (XRD; Rigaku, Smartlab; operated at 40 kV and 200 mA, Cu Kα source). The morphologies were investigated using transmission electron microscopy (TEM) equipped with EDX analyzer (JEOL, JEM 3000F operated at 300 kV or JEM-2100 operated at 200 kV). Scanning TEM (STEM) and energy dispersive spectroscopy (EDS) mapping were performed using a Cs corrected JEM-ARM200F microscope operated at 200 kV. The in situ TEM was operated via the microscope of Hitachi H-800. TG-DTA thermogravimetry (TG) and differential thermal analysis (DTA The steady state UV-Vis absorption and diffuse reflectance spectra were measured by UV-Vis-NIR spectrophotometers (Shimadzu, UV-3100 or Jasco, V-570) at room temperature. The concentration of Pt was determined by ICP (Shimadzu, ICPS-8100). The X-ray photoelectron spectroscopy (XPS) measurements were performed with the PHI X-tool (ULVAC-PHI).

Hydrogen Production Activity Tests. About 2 mg of catalyst was suspended with 2 mL water solution containing lactic acid (10 vol%) in 10 mL quartz cell. The cell was sealed with a rubber septum and purged with Ar gas for 20 min before initiating the irradiation. The sample was irradiated via Xenon lamp (Asahi Spectra, HAL-320; 200 mW cm^{-2}) or UV-LED source (Asahi Spectra, POT-365; 100 mW cm^{-2}) with constant magnetic stirring at room temperature. Under the visible-light irradiation, a 420 nm cutoff filter combined with 750 nm cooling filter were used to remove UV and NIR. After the reaction, 0.1 mL of the gas was collected from the headspace of the reactor and analyzed using a Shimadzu GC-8A gas chromatograph equipped with an MS-5A column and a thermal conductivity detector.

Time-Resolved Diffuse Reflectance Transient Absorption Measurements. The

femtosecond diffuse reflectance transient absorption spectra were measured by the pump and probe method using a regeneratively amplified titanium sapphire laser (Spectra-Physics, Spitfire Pro F, 1 kHz) pumped by a Nd:YLF laser (Spectra-Physics, Empower 15). The seed pulse was generated by a titanium sapphire laser (Spectra-Physics, Mai Tai VFSJW; fwhm 80 fs). The fourth harmonic generation (330 or 440 nm, 3 μJ $pulse^{-1}$) of the optical parametric amplifier (Spectra-Physics, OPA-800CF-1) was used as the excitation pulse. A white light continuum pulse, which was generated by focusing the residual of the fundamental light on a sapphire crystal after the computer controlled optical delay, was divided into two parts and used as the probe and the reference lights, of which the latter was used to compensate the laser fluctuation. Both probe and reference lights were directed to the sample powder coated on the glass substrate, and the reflected lights were detected by a linear InGaAs array detector equipped with the polychromator (Solar, MS3504). The pump pulse was chopped by the mechanical chopper synchronized to one-half of the laser repetition rate, resulting in a pair of spectra with and without the pump, from which the absorption change (% Abs) induced by the pump pulse was estimated. All measurements were carried out at room temperature.

3. Results and Discussion

3.1 Synthesis and Characterization of F-doped TMC.

The synthetic process of F-doped TMC is illustrated in Fig. 1A. The precursor solution containing of Ti^{4+}, F^{-}, NH^{4+}, and H_2O was dropped on silicon wafer to form a thin layer with 2~3 mm thickness. The intermediate NH_4TiOF_3 firstly formed during the initial annealing process below 200 ^{o}C.[18] With elevating annealing temperatures from 200 to 500 ^{o}C, NH_4TiOF_3 transforms into anatase TiO_2 while keeping the morphology.[18,37] Actually, several intermediates such as $HTiOF_3$ and $TiOF_2$ formed during the topotactic transformation, but the process from NH_4TiOF_3 to TiO_2 is still unexplored up to now. The n-type F-doping into TMCs induced the coloration from white to pale yellow after annealing in air (see below). All the annealed samples were referred as Tx, where x represents the annealing temperatures. The analyses of morphologies and elements were carried out using field emission scanning electron microscopy (FESEM) and scanning transmission electron microscopy equipped with energy dispersive X-ray spectroscopy (STEM-EDS) to confirm the structures and spatial distribution of dopants on TMCs. Figs. 1B, C show the sheet-like structures of T500 with the width and thickness of 3~6 μm and ~200 nm, respectively. The exposed pore structures are clearly seen in Figs. 1C and D,

confirming the mesocrystal superstructure. From the high-resolution TEM (HRTEM) image in Fig. 1E, the spaces of 0.24 nm and 0.35 nm are corresponding to the (001) and (101) facets, respectively. The results indicate the crystal grains have a same direction along the [001] axis, which is supported by the symmetric pattern from selective area electron diffusion (SAED) in Fig.1F. From the top view of two stacked sheets, it was observed that F element is distributed over TMCs together with other elements, Ti and O (Fig. 1G).

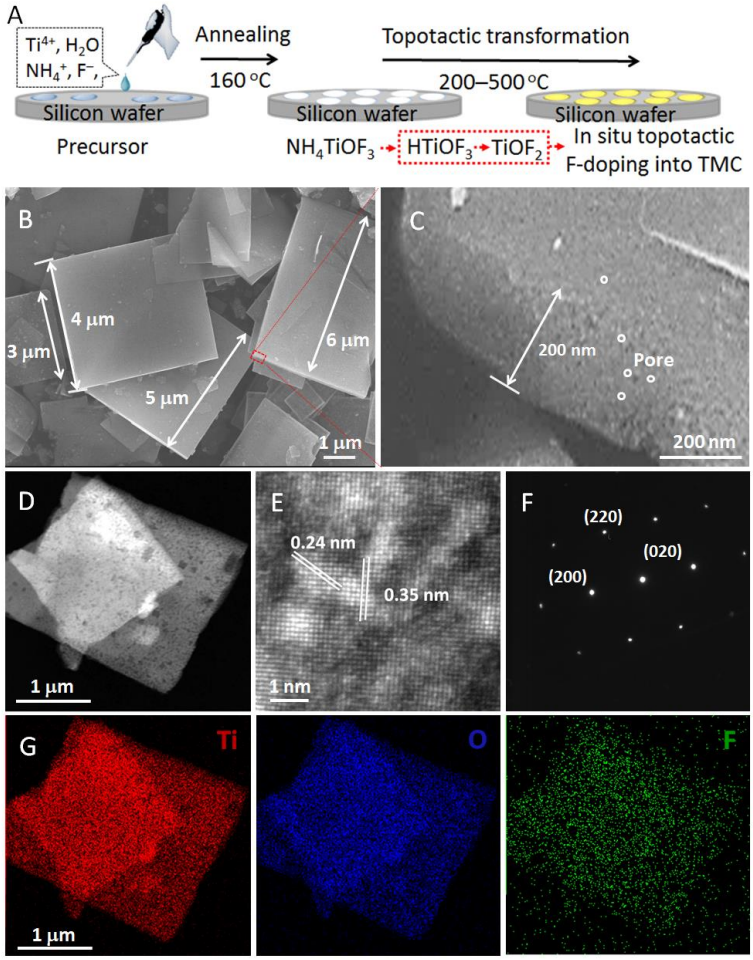

Fig. 1 (A) Schematic diagram of the in situ topotactic F-doping into TiO_2 mesocrystal (TMC) during the topotactic transformation from NH_4TiOF_3 to F-doped TMC via $HTiO_3$ and $TiOF_2$. (B) FESEM, (C) high magnification image marked in (B), (D) dark-field STEM, (E) its HRTEM, (F) SAED pattern, and (G) STEM-EDS elemental mapping images of the as-synthesized T500.

The optical responses of the samples annealed at different temperatures were measured using UV-visible diffuse reflectance spectroscopy (Fig. 2A). The elevated temperatures have a significant effect on the F-doping process. As compared to T300 and T400 as well as T160

(initial intermediate NH_4TiOF_3), T500 showed much stronger visible-light absorption due to its higher F content, which is attributed to the isolated color centers in the midgap (Fig. 2A inset).[38] With a further increase of the annealing temperature (600 ^oC), however, the dopant concentration seems to decrease significantly (Table 1). As shown in Fig. 2B, the TG-DTA curves indicate three sequential stages.[38] Below 250 ^oC, the gradual weight losses appeared mainly due to the removal of water. From 250 ^oC to 420 ^oC, the sharp endothermic peak was related to a phase transformation from NH_4TiOF_3 to $TiOF_2$. The final small endothermic peak between the 420 ^oC and 470 ^oC is alluded to the phase conversion from $TiOF_2$ to TiO_2.[38] There was no additional weight loss beyond 500 ^oC owing to the good thermal stability of the TMC.[18] The observed phase transitions during the in situ topotactic F-doping are further proved by powder XRD and XPS analyses.

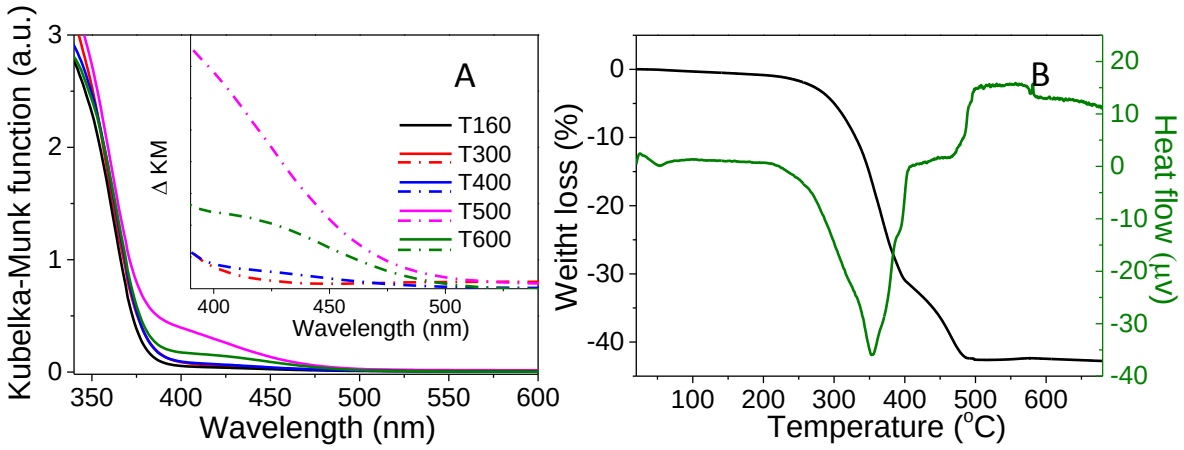

Fig. 2 (A) UV-visible diffuse-reflectance spectra of samples annealed at different temperatures and the subtracted spectra by differentiating from the spectrum of T160 (inset). (B) TG-DTA curve of NH_4TiOF_3 measured in air.

3.2 In situ Temperature-Dependent Measurements.

In situ temperature-dependent powder XRD measurements provide a vital capability to monitor the evolution of phase composition and crystallization during the in situ topotactic F-doping after thermal annealing. The XRD patterns were collected from the samples at desired temperatures in air with the rate of 10 ℃ min^{-1}, as shown in Fig. 3A. All the diffraction peaks of T160, which was used as the starting material, are matched well with those in the standard card of NH_4TiOF_3, indicating no impurity phase. It was found that a broad band centered at $2\theta = 25.1^o$

appeared after heating to 200 ^{o}C, which is corresponding to the (101) crystallographic planes of anatase TiO_2. The crystallinity of TiO_2 increased from T230 to T260 along with the decreases of all diffraction intensities of NH_4TiOF_3. A dissolution of NH_4TiOF_3 to intermediate $HTiOF_3$ was not characterized due to their similar diffraction peaks.[39] Coincided with the description at the second stage of TG-DTA, an intermediate of $TiOF_2$ with (100) plane diffraction at $2\theta = 23.4^{o}$ was found in T290. From the peak deconvolution from T160 to T320 in the enlarged XRD patterns (Fig. 3B), it was clarified that the dominated components changed from NH_4TiOF_3 ($HTiOF_3$) to $TiOF_2$ with increasing the temperature. The transformation of $TiOF_2$ to F-doped TiO_2 started at ~300 ^{o}C with the disappearance of $TiOF_2$ peaks. This result is not consistent with the TG-DTA curve in the range of 420~470 ^{o}C, suggesting that $TiOF_2$ crystals within TiO_2 phase formed at ~300 ^{o}C and underwent the phase transition at higher temperatures at 420~470 ^{o}C due to the dissolution-recrystallization.[33,34] Further heating treatment from 320 ^{o}C to 500 ^{o}C improves the crystallinity of anatase TiO_2, which is suggested by the stronger peak intensity and the narrower diffraction peak.

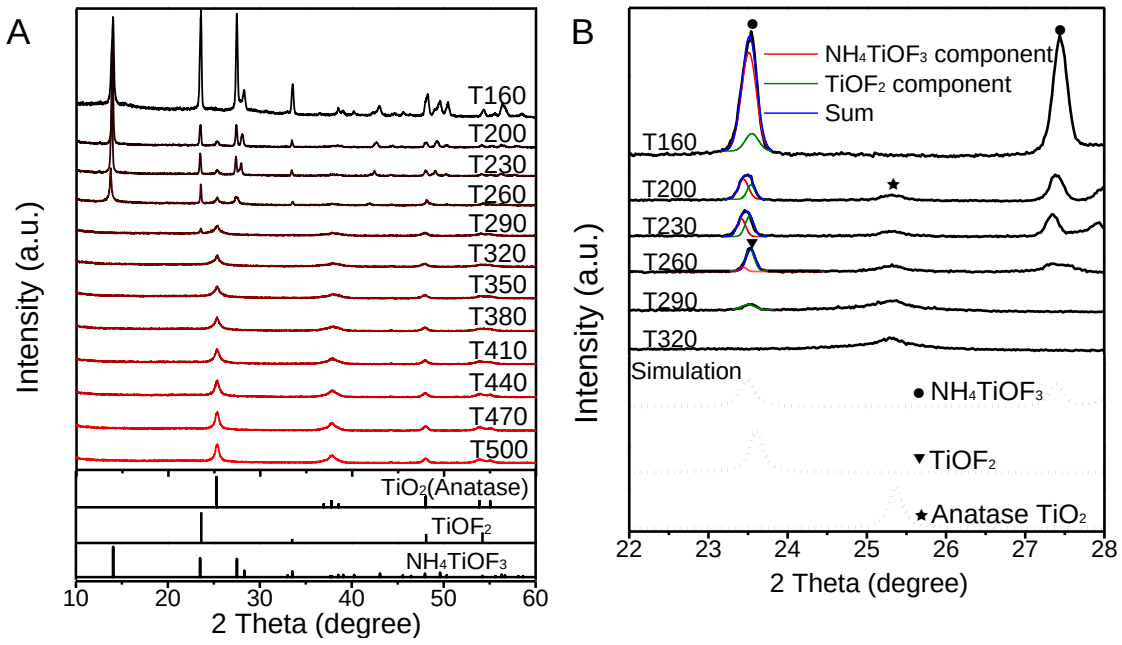

Fig. 3. (A) In situ heating powder XRD patterns upon variable annealing temperatures and (B) Enlarged patterns with phase deconvolutions and simulation results of NH_4TiOF_3, $TiOF_2$, and anatase TiO_2.

The relative elemental compositions including the in situ topotactic F-doping were analyzed via XPS (Fig. 4 and Table 1). The elements of F, O, and Ti were present in the survey scans from the annealed samples, except the N element in T160 (Fig. 4A). Intriguingly, the T300 without N peaks reveals the formation of intermediate $HTiOF_3$ from NH_4TiOF_3 after NH_3 gas was released. From the high-resolution XPS spectra of F 1s in Fig. 4B, the independent phase of $TiOF_2$ formed in TiO_2 was confirmed by its symmetric peak centered at ca. 685.3 eV among the T400 and T500, suggesting the in situ topotactic F-doping from the intermediate source of $TiOF_2$.[32,40] The shifts of Ti $2p_{3/2}$ and O 1s peaks with elevating temperatures are mainly ascribed to the formation of TiO_2 (Figs. 4C, D).[32,37] Note that the intensity at around 457 eV represents the Ti^{3+} state, which was formed by Ar sputtering.

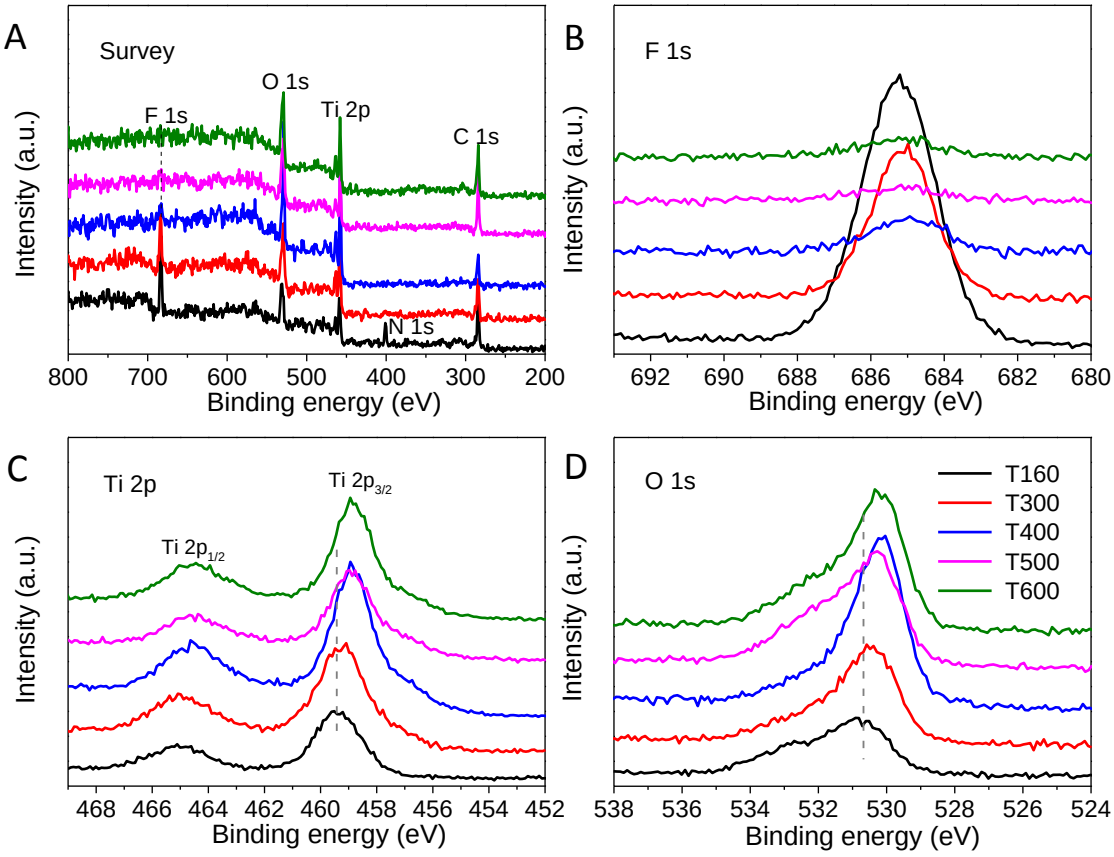

Fig.4 XPS spectra of (A) survey scans, (B) F 1s, (C) Ti 2p, and (D) O 1s in the series of the samples annealed at various temperatures.

Table 1. XPS Peak Positions and the F Contents of the Samples with Various Annealed Temperatures.

Sample	Ti $2p_{3/2}$ (eV)	O 1s (eV)	F 1s (eV)	F/Ti
T160	459.4	530.7	685.2	2.60
T300	459.3	530.4	685.1	1.11
T400	458.9	530.1	685.2	0.25
T500	458.9	530.1	685.3	0.26
T600	458.9	530.1	685.3	0.19

To gain more insights into the intermediate phase transition during the in situ topotactic F-doping, the dynamic structural evolution of growth mechanism was monitored via in situ temperature-dependent TEM. All TEM and SAED images are acquired and analyzed from the same area. Starting from T160 (Fig. 5A), the sheet-like NH_4TiOF_3 was observed with invisible pore structures on the surface.[18] The symmetry diffraction spots along the [001] zone-axis are derived from the ordered orthorhombic single crystal orientation (Fig. 5G).[37] To observe the growth processes with morphological changes, a series of temporal TEM images (Figs. 5B-F) with the representative diffraction patterns (Figs. 5H-L) were obtained during further annealing in TEM. As temperature was gradually elevated, the overall shapes from T160 to T500 are preserved with similar thickness and edge length ascribed to the topotactic transformation from NH_4TiOF_3 to F doped TiO_2 with the similar critical parameters in {001} plane (NH_4TiOF_3: a = 7.5594 Å, b = 7.5754 Å, c = 12.7548 Å; TiO_2: a = b = 3.78 Å, c = 9.5143 Å).[37] Of particular interest, the complex growth processes of block fusing and crystallographically ordered assembling were clearly observed (Figs. 5B-F). From T200 and T300 (Figs. 5B, C), the small TiO_2 grains were generated and grown larger with consuming the lattice-matched NH_4TiOF_3 (Fig. 3A). As an exact intermediate of $HTiOF_3$ (a = b = 3.74 Å, c = 12.59 Å) from NH_4TiOF_3, the layered structure of $TiOF_5$ octahedral is triggering to change to $TiOF_2$ thermodynamically.[39] The F-doped TMC structure was expected to form in the temperature range of 350 ^oC ~ 400 ^oC (Figs. 5D, E) with accompanying the spaces between the adjacent nanocrystals by fusion and shrink.[37,41,42] The intermediate $TiOF_2$ is considered as a good template for the phase transformation to TiO_2 with recrystallization from edge to center (Figs. 5D-E).[33,34] The defective

constructions around the center from irregular aggregates of merged nanocrystals happened occasionally during the topotactic transformation. However, there is no significant effect on the mesocrystal structure of TiO_2 from its depicted diffractions with minor distortions. The roughening facet and visible porosity were observed in the final structure of T500 with aligned nanocrystals (Fig. 5F), which remains the original dimension of NH_4TiOF_3 controlled by the facet directing agent of HF.[18] Attributed to the similar arrangement of Ti atom in the {001} planes, all materials exhibited identical diffraction patterns across the static orientation. These real-time imaging and electron diffraction patterns directly support the temperature-dependent phase transition.

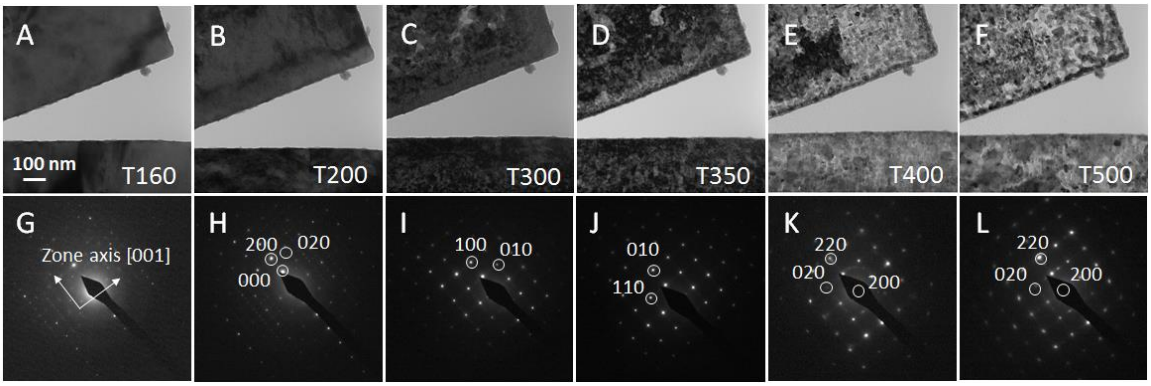

Fig. 5 In situ temperature-dependent (A-F) TEM images and (G-I) their corresponding SAED patterns from T160 (i.e., NH_4TiOF_3 as the starting material) in vacuum.

3.3 Photocatalytic H_2 Evolution and Charge Transfer Dynamics on F-doped TMC.

The photocatalytic hydrogen generation of pure TMC[18] and F-doped TMCs with Pt modification was evaluated under the visible-light irradiation ($\lambda \geq 420$ nm) as shown in Fig. 6A. As compared to pure TMC with no absorption in the visible-light region, all F-doped TMC markedly enhanced the photocatalytic efficiency because of their absorption in the visible-light region. It was observed that T500 with the Pt modification exhibited the highest activity (1.7 $\mu mol\ g^{-1}\ h^{-1}$) among them due to the strongest visible-light absorption induced by the highest F-dopant concentration (Table 1).[40] However, T600 lost about a half in the activity compared to T500, which is attributed to the loss of F-dopants after annealing at 600 ^oC (Table 1). To elucidate the significant role of F-doping into TMC, T500 was annealed in O_2 at 600 ^oC (T500-O_2) to lower the F contents and remove V_o (Fig. S1).[27] T500-O_2 has a lower concentration of F-dopant inducing a lower visible-light photocatalytic activity than T500 (Fig. 6B). On the other

hand, T500-O_2 exhibited more superior activity compared to T500 under the UV irradiation.

In order to understand the photocatalytic activity of T500 and T500-O_2 under the visible-light and UV irradiation, the charge transfer dynamics in photocatalysis was examined by the time-resolved diffuse reflectance transient absorption measurements (Fig. 6C). The kinetic parameters were determined from the decays of transient absorption at 900 nm assigned to the trapped electrons[21] as summarized in Table 2. Upon the 440-nm laser excitation, it was observed that the decay occurred within the subpicosecond time scale for T500-O_2 (τ_1, 0.6 $\pm$0.1 ps), faster than for T500 (τ_1, 2.4 $\pm$0.3 ps). In the case of T500, more Ti^{3+} species with good electronic conductivity were produced in TMC after n-type F-doping.[17,28] The longer lifetime of electrons were attributed to their trapping/detrapping processes via Ti^{3+} (F) doping states (Fig. S1).[43] In the case of T500-O_2 with lower F components, a large number of electrons formed at the shallow trapes promptly recombined with neighboring holes (Fig. S1). In the period of 10~50 ps, a similar decay of T500 (τ_2, 50 $\pm$ 3 ps) and T500-O_2 (τ_2, 48 $\pm$ 4 ps) was observed because the trapped electrons escaped from geminate recombination and relaxed into deeper trap levels.[43] Over 100 ps, the trapped electrons decayed in the ns-time range for T500 and T500-O_2. A little longer lifetime for T500 (τ_3, 2691 $\pm$107 ps) does not support four times higher photocatalytic efficiency for H_2 generation than T500-O_2 (τ_3, 2436 $\pm$ 142 ps), suggesting other important factors such as surface potential and hydrophilicity favorable for T500 due to F-doping.[44] The holes were considered to be trapped at the shallow trap sites and their spectral position is outside the wavelength range measured here. It is noteworthy that an opposite tendency was observed under the UV laser excitation for the decay kinetics of trapped electrons for T500-O_2, 12.5 $\pm$ 0.9 ps (τ_1), 110 $\pm$ 7 ps (τ_2), 3622 $\pm$ 162 ps (τ_3), and for T500, 5.7 $\pm$ 0.3 ps (τ_1), 62 $\pm$ 3 ps (τ_2), 2480 $\pm$97 ps (τ_3). After excited with the 330-nm laser, conduction-band electrons in T500 are trapped in the time scale of 5.7 ps to the inherent defects, possibly V_o, and recombine the holes, which is faster than in T500-O_2. Meanwhile, the O_2 treatment of T500 successfully removed such undesired recombination centers, thus resulting in the longer lifetime of 12.5 ps for the trapped electrons. The difference of τ_3 (3622 ps and 2480 ps for T500-O_2 and T500, respectively) is roughly consistent with two times difference of photocatalytic activity for H_2 generation.

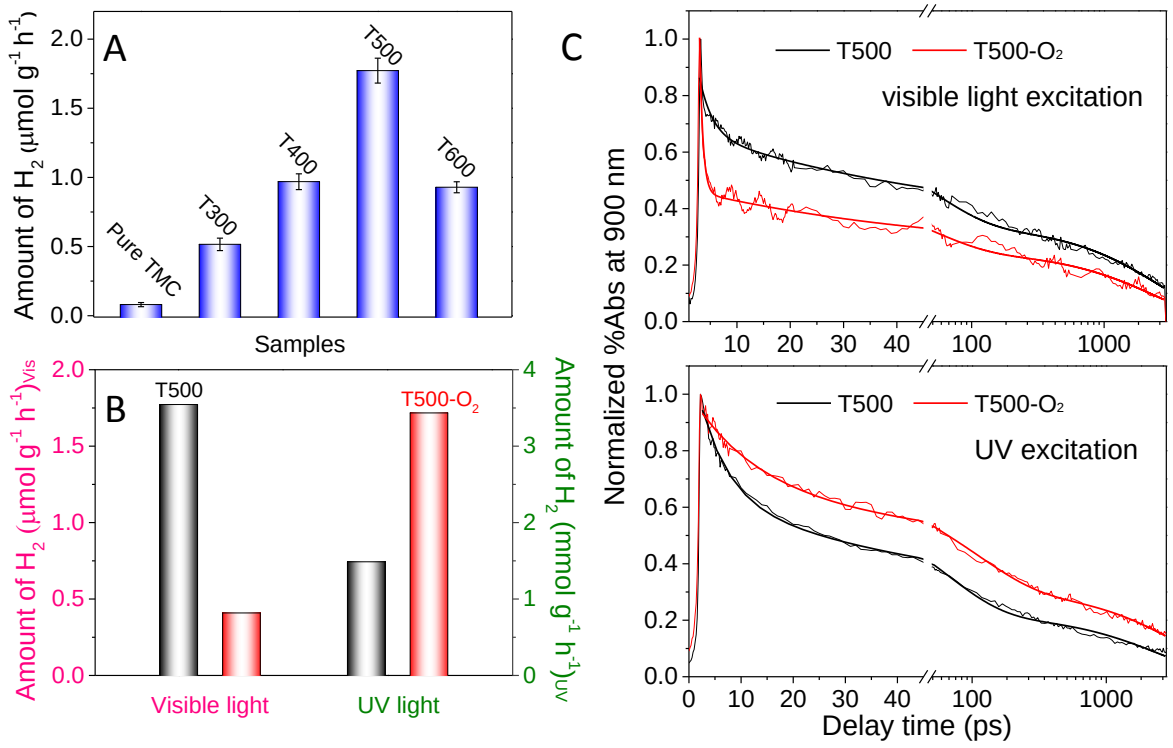

Fig. 6 (A) Hydrogen evolution for TMC and F-doped TMCs with Pt modification under the visible-light irradiation. (B) Comparison of photocatalytic activity for T500 and T500-O_2 under the visible-light and UV irradiation. (C) Normalized transient absorption traces observed at 900 nm for T500 (black) and T500-O_2 (red). Bold lines in (C) indicate multiexponential curves fitted to the kinetic traces.

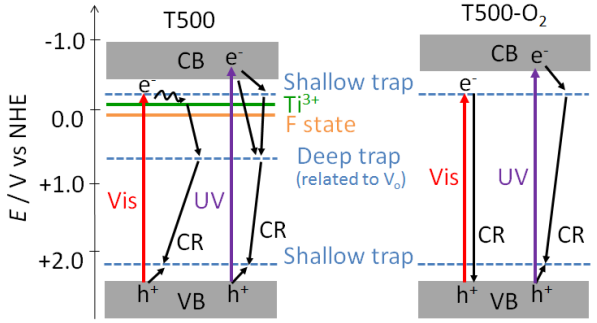

Fig. S1. Schematic illustration of the spatial and energetic distribution of the electrons and holes in T500 (left) and T500-O_2 (right) after visible and UV light excitation.

Table 2. Kinetic Parameters of Decays for T500 and T500-O_2 under the Visible (440 nm) or UV (330 nm) Laser Excitations

Sample	Excitation	τ_1 (ps)	τ_2 (ps)	τ_3 (ps)
T500	Visible	2.4 ± 0.3 (32%)	50 ± 3 (34%)	2691 ± 107 (34%)
	UV	5.7 ± 0.3 (45%)	62 ± 3 (36%)	2480 ± 97 (19%)
T500-O_2	Visible	0.6 ± 0.1 (53%)	48 ± 4 (22%)	2436 ± 142 (25%)
	UV	12.5 ± 0.9 (34%)	110 ± 7 (35%)	3622 ± 162 (31%)

4. Conclusion

The details of crystal growth, phase transition, and dynamic structural evolution during the topotactic transformation from NH_4TiOF_3 to F-doped TMC were monitored via in situ temperature-dependent XRD and TEM techniques. It was found that intermediate $TiOF_2$ was incorporated as F color centers to F-doped TMC without any morphological change. The comparison of the charge transfer dynamics with the photocatalysitc efficiency for T500 and T500-O_2 confirmed that n-type F-doping (T500) induces faster electronic mobility and surface modification favorable for the efficient visible-light driven H_2 generation. Although the present F-doped TMCs are required to be improved for their performance, the in situ topotactic F-doping into TMC for incorporation of active color centers will facilitate the development of materials design with visible-light response and accelerate their applications in various fields including energy and environment.

5. Reference

(1) Chen, X.; Shen, S.; Guo, L.; Mao, S. S.*Chem. Rev.* **2010,** *110*, 6503.

(2) Kudo, A.; Miseki, Y. *Chem. Soc. Rev.* **2009**, *38*, 253.

(3) Fujishima, A.; Honda, K. *Nature* **1972**, *238*, 37.

(4) Ma, Y.; Wang, X.; Jia, Y.; Chen, X.; Han, H.; Li, C. *Chem. Rev.* **2014**, *114*, 9987.

(5) Kapilashrami, M.; Zhang, Y.; Liu, Y. S.; Hagfeldt, A.; Guo, J. *Chem. Rev.* **2014**, *114*, 9662.

(6) Sang, L. X.; Zhao, Y. X.; Burda, C. *Chem. Rev.* **2014**, *114*, 9283.

(7) Yang, J.; Wang, D.; Han, H.; Li, C. *Acc. Chem. Res.* **2013**, *46*, 1900.

(8) Ran, J.; Zhang, J.; Yu, J.; Jaroniec, M.; Qiao, S. Z. *Chem. Soc. Rev.* **2014**, *43*, 7787.

(9) Trasatti, S. *J. Electroanal. Chem.* **1972**, 39, 163.

(10) Nørskov, J. K.; Bligaard, T.; Logadottir, A.; Kitchin, J. R.; Chen, J. G.; Pandelov, S.; Stimming, U. *J. Electrochem. Chem.* **2005**, *152*, 23.

(11) Nørskov, J. K.; Bligaard, T.; Rossmeisl, J.; Christensen, C. H. *Nat. Chem.* **2009**, *1*, 37.

(12) Chhowalla, M.; Shin, H. S.; Eda, G.; Li, L. J.; Loh, K. P.; Zhang, H.*Nat. Chem.* **2013**, *5*, 263.

(13) Yan, Y.; Xia, B.; Xu, Z.; Wang, X. *ACS Catal.* **2014**, *4*, 1693.

(14) Kanda, S.; Akita, T.; Fujishima, M.; Tada, H. *J. Colloid Interface Sci.* **2011**, *354*, 607-610.

(15) Zhou, W.; Yin, Z.; Du, Y.; Huang, X.; Zeng, Z.; Fan, Z.; Liu, H.; Wang, J.; H. Zhang, *Small* **2013**, *9*, 140-147.

(16) King, L. A.; Zhao, W.; Chhowalla, M.; Riley, D. J.; Eda, G. *J. Mater. Chem. A* **2013**, *1*, 8935-8941.

(17) Eda, G.; Yamaguchi, H.; Voiry, D.; Fujita, T.; Chen, M.; Chhowalla, M. *Nano Lett.* **2011**, *11*, 5111-5116.

(18) Lukowski, M. A.; Daniel, A. S.; Meng, F.; Forticaux, A.; Li, L.; Jin, S. *J. Am. Chem. Soc.* **2013**, *135*, 10274-10277.

(19) Ding, Q.; Meng, F.; English, C. R.; Cabán-Acevedo, M.; Shearer, M. J.; Liang, D.; Daniel, A. S.; Hamers, R. J.; Jin, S. *J. Am. Chem. Soc.* **2014**, *136*, 8504-8507 .

(20) Voiry, D.; Salehi, M.; Silva, R.; Fujita, T.; Chen, M.; Asefa, T.; Shenoy, V. B.; Eda, G.; Chhowalla, M. *Nano Lett.* **2014**, *13*, 6222-6227.

(21) Maitra, U.; Gupta, U.; De, M.; Datta, R.; Govindaraj, A.; Rao, C. N. R. *Angew. Chem., Int. Ed.* **2013**, *52*, 13057-13061.

(22) Hinnemann, B.; Moses, P. G.; Bonde, J.; Jørgensen, K. P.; Nielsen, J. H.; Horch, S.; Chorkendorff, I.; Nørskov, J. K. *J. Am. Chem. Soc.* **2005**, *127*, 5308-5309.

(23) Jaramillo, T. F.; Jørgensen, K. P.; Bonde, J.; Nielsen, J. H.; Horch, S.; Chorkendorff, I. *Science* **2007**, *317*, 100-102.

(24) Kibsgaard, J.; Chen, Z.; Reinecke, B. N.; Jaramillo, T. F. *Nat. Mater.* **2012**, *11*, 963-969.

(25) Zong, X.; Na, Y.; Wen, F.; Ma, G.; Yang, J.; Wang, D.; Ma, Y.; Wang, M.; Sun, L.; Li, C. *Chem. Commun.* **2009**, 4536-4538.

(26) Min, S.; Lu, G. *J. Phys. Chem. C.* **2012**, *116*, 25415-25424.

(27) Li, Y.; Wang, H.; Xie, L.; Liang, Y.; Hong, G.; Dai, H. *J. Am. Chem. Soc.* **2011**, *133*, 7296-7299.

(28) Xiang, Q.; Yu, J.; Jaroniec, M. *J. Am. Chem. Soc.* **2012**, *134*, 6575-6578.
(29) Meng, F.; Li, J.; Cushing, S. K.; Zhi, M.; Wu, N. *J. Am. Chem. Soc.* **2013**, *135*, 10286-10289.
(30) Chang, K.; Mei, Z.; Wang, T.; Kang, Q.; Ouyang, S.; Ye, J. *ACS Nano* **2014**, *8*, 7078-7087.
(31) Bian, Z.; Tachikawa, T.; T.Majima, *J. Phys. Chem. Lett.* **2012**, *3*, 1422-1427.
(32) Bian, Z.; Tachikawa, T.; Zhang, P.; Fujitsuka, M.; Majima, T. *J. Am. Chem. Soc.* **2014**, *136*, 458-465.
(33) Tachikawa, T.; Zhang, P.; Bian, Z.; Majima, T. *J. Mater. Chem. A* **2014**, *2*, 3381-3388.
(34) Bian, Z.; Tachikawa, T.; Zhang, P.; Fujitsuka, M.; Majima, T. *Nat. Commun.* **2014**, 5:3038.
(35) Chou, S. S.; Kaehr, B.; Kim, J.; Foley, B. M.; De, M.; Hopkins, P. E.; Huang, J.; Brinker, C. J.; Dravid, V. P. *Angew. Chem., Int. Ed.* **2013**, *52*, 4160-4164.
(36) Yu, Y.; Huang, S. Y.; Li, Y.; Steinmann, S. N.; Yang, W.; Cao, L. *Nano Lett.* **2014**, *14*, 553-558.
(37) Tachikawa, T.; Yamashita, S.; Majima, T. *J. Am. Chem. Soc.* **2011**, *133*, 7197-7204.
(38) Pan, J.; Liu, G.; Lu, G. Q.; Cheng, H. M. *Angew. Chem., Int. Ed.* **2011**, *50*, 2133-2137.
(39) Bian, Z.; Tachikawa, T.; Kim, W.; Choi, W.; Majima, T. *J. Phys. Chem. C* **2012**, *116*, 25444-25453.

Part 2. Nitrogen and fluorine codoping on TMC with interaction in visible-light-induced photocatalytic activity

1. Introduction

The visible light induced photocatalyst has been widely progressed with continuous consideration on environmental pollution and insufficient natural energy. The photoactivation of TiO_2 has caused enormous interest to scientists and engineers after the photocatalytic water splitting reported by Fujishima and Honda in 1972.[1] Due to the versatile physicochemical properties of nontoxicity, high chemical stability, low cost, and easy synthesis, TiO_2 is a promising photocatalyst to be applied in the wide range of solar-to-chemical energy conversion such as environmental remediation, solar water splitting, CO_2 photoreduction, and photovoltaic cells.[2-5] However, because of the intrinsic wide band gap, TiO_2 can be only excited under the UV

light irradiation which covers less than ~5% of the solar spectrum. Aimed at the practical utilization of visible light, a variety of modifications are undertaken to tune the band gap of the electronic structure.[6-7] Among the metal and non-metal doping, the N doping is the most efficient avenues to create N 2p in the localized midgap state leading to the increase of thermal stability and the decrease of recombination centers.[8-10] With the respect to synthesize N-doped TiO_2, a large amount of nitrification processes, such as wet and dry process with additional N source, are embodied in nano powders, thin films, nanotubes and nanowires.[8-10] However, it is still highly required a facile synthetic craft to dope N on anatase TiO_2 without the instrument-dependent and cost-ineffective treatment.

It is worthily mentioned that the large-scale preparation in practical application, the novel pyrolysis of Ti-compound containing dopants is proposed as the ideal candidate to acquire efficient doping.[11] The ammonium oxofluorotitanate is a fundamental group of Ti-compound for the synthesis of doped TiO_2.[12] It is inferred that the anisotropic dissolution of NH_4TiOF_3 can chemically convert to TiO_2 mesocrystal (TMC) during the topochemical transformation, accompanying with N and F releasing.[13-16] As a new class of porous building blocks oriented assembly of nanocrystals, the obtained TMC with a well-defined crystal shape significantly enhances the charge separation with remarkably long-lived charges and exhibits excellent photocatalytic activities compared with TiO_2 nanocrystals and commercial P25.[17-20] It is a great of significance to introduce the dopant simultaneously from the original precursors or intermedium during the synthesis, without affecting the nucleation and growth on TMC. With more positive promotion of N doping for larger photostability and photocatalytic efficiency, it is an imperative issue to exploit the effects of the F codoping on the N-doped TMC with the visible light activity.[6, 21] Although fascinating performances emerged in a variety of codoping methods have been studied, the mechanism of the interaction among versatile dopants is still inconclusive due to the complexity of the methods.

To resolve the scientific challenge in doping field, the author reported a novel strategy for the synthesis of TMC with the uniform distribution of N, F dopants from the direct annealing of the intermediate NH_4TiOF_3 during the topochemical transformation. The photoreductive efficiency of Cr (VI) to Cr (III) was correlated to the optical absorption dependent on the dopant content at various annealing temperatures. The author confirmed the doping of N in the localized midgap state together with the surface adsorbed F enhanced the photocatalytic degradation of MB based

on charge transfer dynamics under the visible or UV light irradiation. With the effect in promoting the visible light absorption and facilitating the degradation efficiency, the N and F codoping on TiO_2 as the prevalent photocatalyst will open a new road in the practical application under the solar light irradiation.

2. Experimental section

Materials. The titanium (IV) fluoride was purchased from Sigma-Aldrich. The ammonium nitrate, ammonium fluoride, and boric acid were purchased from Wako Pure Chemical Industries. All of these chemicals were analytical grade and used as received.

Preparation of NH_4TiOF_3. The samples were synthesized with some modifications according to the previous reports.[22-24] A precursor solution containing TiF_4, H_2O, NH_4NO_3, and NH_4F (molar ratio= 1:503.4:4.9:2.4) was prepared, and were placed on a silicon wafer to form a thin layer. It was calcined in air using a heating rate of 10 $^oC\ min^{-1}$ at 160 ^oC for 2 h. The annealed sample was collected for the further treatment.

Preparation of TiO_2 Mesocrystal (TMC). The as-prepared NH_4TiOF_3 was mixed with boric acid (0.5 M) at 60 ^oC for 4 h and dried after washing by water and ethanol separately.[25] Furthermore, the obtained samples were calcined at 500 ^oC for 0.5 h, which was referred as pristine TMC.

Preparation of Doped TMC. The as-prepared NH_4TiOF_3 placed in a narrow neck vessel (L ×R = 7.5 cm ×1.75 cm) with a lid was annealed in air with a heating rate of 20 $^oC\ min^{-1}$ at different temperatures for 0.5 h. The obtained samples were designed as NFT-x, in which the x represents the annealing temperatures. As a controllable reference, the NFT samples were treated with NaOH aqueous solution (0.01 M) in the dark for 8 h to remove the excess fluorine impurity, which was referred as NFT-NaOH.[26]

Characterization. The structures of the samples were examined using X-ray diffraction (XRD; Rigaku, Smartlab; operated at 40 kV and 200 mA, Cu Kα source). The morphologies were investigated using field-emission scanning electron microscopy (FESEM) equipped with EDX analyzer (JEOL, JSM-6330FT) and transmission electron microscopy (TEM) equipped with EDX analyzer (JEOL, JEM-2100 operated at 200 kV). Scanning TEM (STEM) and energy dispersive spectroscopy (EDS) mapping were performed using a Cs corrected JEM-ARM200F microscope operated at 200 kV. The Brunauer–Emmett–Teller (BET) surface areas were measured using nitrogen sorption (BEL Japan, BELSORP max). The pore volumes and pore

diameter distributions were derived from the adsorption isotherms using the Barrett–Joyner–Halenda (BJH) model. The steady state UV-Vis absorption and diffuse reflectance spectra (DRS) were measured by UV-Vis-NIR spectrophotometers (Shimadzu, UV-3100 or Jasco, V-570) at room temperature. The thermal analysis was performance by thermogravimetric analysis (Rigaku, Thermo plus EVO II/TG-DTA, TG8120) in N_2. The X-ray photoelectron spectroscopy (XPS) spectral measurements were performed with the PHI X-tool (ULVAC-PHI).

Photocatalytic Test. For a typical photocatalytic process, the catalytic dispersions (2 g L^{-1}) containing $K_2Cr_2O_7$ (Wako Pure Chemical Industries, 0.05 mM, pH = 3) or methylene blue (Wako Pure Chemical Industries, 0.03 mM) were transferred to a quartz cuvette after sonication. The photocatalytic reaction was initiated by irradiation with UV-LED source (POT-365; 100 mW cm^{-2}) or Xenon lamp (HAL-320; 200 mW cm^{-2}), with constant magnetic stirring at room temperature. After stopping the light illumination, the sample was centrifuged at 10000 rpm (Hitachi, himac CF16RX) to separate the solid particles. The concentration of unreacted molecules, from which the degradation yield was calculated, was analyzed using a UV-visible-near infrared spectrophotometer (Shimadzu, UV-3600) at the characteristic wavelength.

Time-resolved Diffuse Reflectance Spectral Measurements. The femtosecond diffuse reflectance spectra (TDR) were measured by the pump and probe method using a regeneratively amplified titanium sapphire laser (Spectra-Physics, Spitfire Pro F, 1 kHz) pumped by a Nd:YLF laser (Spectra-Physics, Empower 15). The seed pulse was generated by a titanium sapphire laser (Spectra-Physics, Mai Tai VFSJW; fwhm 80 fs). The fourth harmonic generation (330 or 440 nm, 3 μJ $pulse^{-1}$) of the optical parametric amplifier (Spectra-Physics, OPA-800CF-1) was used as the excitation pulse. A white light continuum pulse, which was generated by focusing the residual of the fundamental light on a sapphire crystal after the computer controlled optical delay, was divided into two parts and used as the probe and reference lights, of which the latter was used to compensate the laser fluctuation. Both the probe and reference lights were directed to the sample powder coated on the glass substrate, and the reflected lights were detected by a linear InGaAs array detector equipped with the polychromator (Solar, MS3504). The pump pulse was chopped by the mechanical chopper synchronized to one-half of the laser repetition rate, resulting in a pair of spectra with and without the pump, from which the absorption change (% Abs) induced by the pump pulse was estimated. All measurements were carried out at room temperature.

3. Results and Discussion

To investigate the growth mechanism during the topochemical transformation (Fig. 1), the phase identification and the structural analysis of doped TMCs were performed from XRD, N_2 adsorption–desorption isotherm with pore size distribution, and the FESEM. After the water evaporation from the precursor (Process A), the phase of NH_4TiOF_3 was firstly formed on silicon wafer at 160 ^oC. The sheet-like NH_4TiOF_3 mesocrystal showed invisible pore superstructure on the surface and low surface area (7.4 m^2 g^{-1}, Table 1) due to the assemble fusion.[14-15] Subsequently, the NH_4TiOF_3 mesocrystal was collected from silicon wafer and annealed in a narrow neck vessel to 200 ^oC (Process B). It is noted that a major part of the NH_4TiOF_3 was transformed to anatase TiO_2 after calcined at 300 ^oC (Fig. 2A). Additionally, the surface structure started to decompose and merge to be the larger particles than NH_4TiOF_3 (Fig. 3A and Table1).[11] Upon further annealing to 400 ^oC, the pure phase of anatase TiO_2 formed from NH_4TiOF_3 without morphology change, which is attributed to the topochemical transformation (Fig. 3B).[22] More importantly during this process, the sources of N and F were released from the crystal lattice of NH_4TiOF_3 and doped on TMC simultaneously in a narrow neck vessel.[25] The clear shrinks of the crystal lattice resulted from the doping are in good agreement with the movement of (101) diffraction peak toward to the higher angle range (Fig. 2A inset).[21, 27-28] When the annealing temperatures increased to 500 ^oC, the void was formed to create the visual porous structures between the adjacent nanocrystals (Fig. 3C). This result is consistent with decreasing gradually the specific surface area (17.7 m^2 g^{-1}, Table 1) and increasing the particle size (2.08 nm, Table 1) due to the fusion of TiO_2 nanoparticles.[22] Continuously elevating up to 600 ^oC, most of the structures are collapsed inevitably into nanoscale particles (2.08 nm, Table 1) with the decrease of the surface area (9.8 m^2 g^{-1}, Table 1) in Fig. 3D. But there was no remarkable impurity phase observed after the annealing at 600 ^oC due to its good thermal stability of the anatase phase.[22] It can be deduced that the TMC undergoes crystal growth during the doping process, correlated to the strengthened crystallinity from the sharper diffraction peaks as the elevating temperatures. The series of annealed samples were referred as NFT-x, in which x represents the annealing temperature. As compared to the doped TMC, the pristine TMC showed a smaller average size, due to the dissolution and disaggregation during the recrystallization by the H_3BO_3 treatment (Table 1).[11]

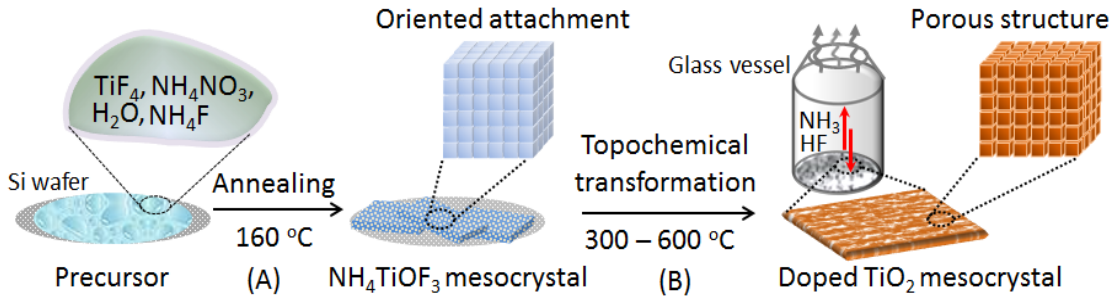

Fig. 1 Schematic illustration of preparation for N and F codoped TiO_2 mesocrystals (NFT).

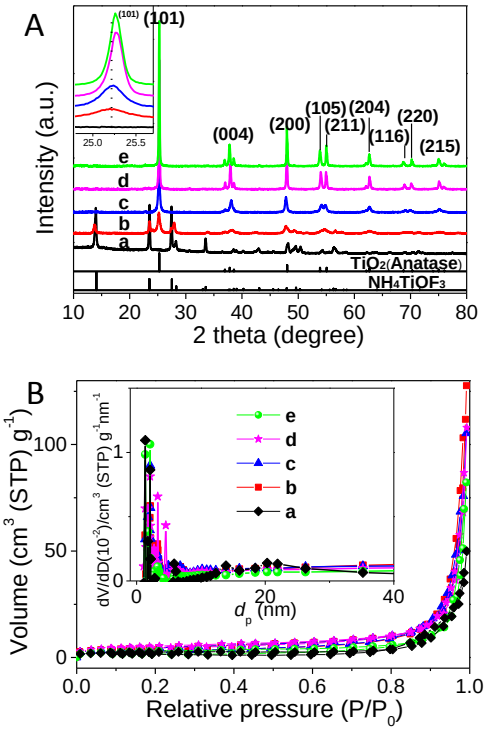

Fig. 2 (A) Powder XRD patterns with an enlarged (101) diffraction peak (inset), (B) N_2 adsorption–desorption isotherms and pore size distribution (inset) of (a) NH_4TiOF_3, (b) NFT-300, (c) NFT-400, (d) NFT-500, and (e) NFT-600.

Table 1. Structural characteristics of NH_4TiOF_3, pristine TMC, and doped TMC at various annealing temperatures.

Sample	S_{BET} ($m^2 g^{-1}$)	V_p ($cm^3 g^{-1}$)	D_p (nm)	N content (wt %)	F content (wt %)
Pristine TMC	23	0.10	2.03	0.01	0.03
NH_4TiOF_3	7.4	0.03	1.34	14.20	33.16
NFT-300	16.0	0.07	2.06	5.43	20.4
NFT-400	16.1	0.07	2.07	2.30	6.1
NFT-500	17.7	0.06	2.08	3.23	4.87
NFT-600	9.79	0.05	2.08	3.03	3.78

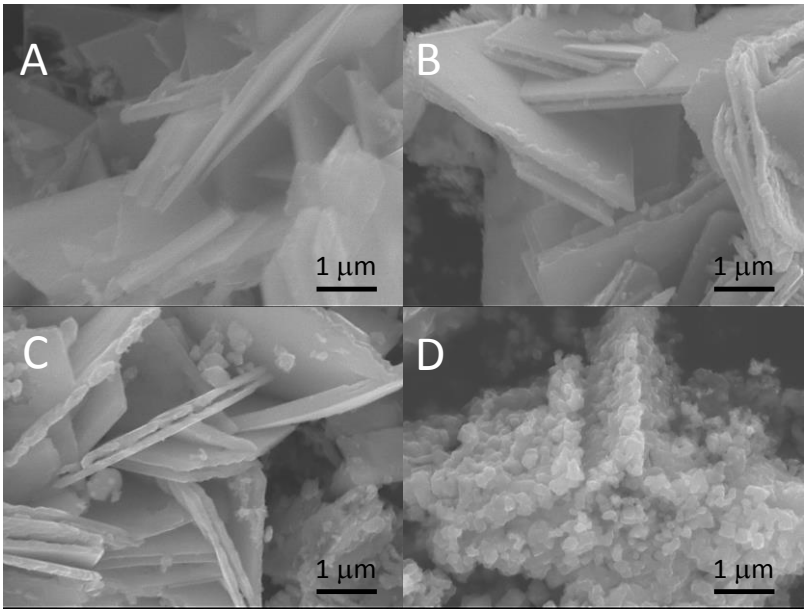

Fig. 3 FESEM images of (A) NFT-300, (B) NFT-400, (C) NFT-500, and (D) NFT-600.

The morphology of NFT-500 was characterized by TEM in Fig. 4A. It is observed that NFT-500 has a sheet-like structure with {001} facet dominated from the selective area electron diffusion (SAED) in Fig. 4A inset.[19] Comparable to other samples with different annealing temperatures in Table 1, the EDS analysis of NFT-500 exhibited the high concentrations of N (3.23 wt%) and F (4.87 wt%) in Fig. 4B, showing that the N and F doping are strongly dependent on the elevating temperature.[29-30] From the elemental mapping in Fig. 4C, it is clearly observed that both N and F are doped on TMC superstructure with homogeneous distribution. The doping intensity increased as the elevating temperature, which is in good agreement with the optical spectrum (see below). Their chemical composition of NFT-500 was analyzed by XPS. The XPS spectra of F 1s with binding energy around 684 eV and 688.5 eV are ascribed to the F absorbed

on surface and substitution.[28, 30-31] It has been reported that the substitutional N modification is formed due to the detected N 1s peak centered at 399 eV.[9, 31-32] Ti^{4+} on the surface was observed with two peaks of Ti $2p_{1/2}$ (465 eV) and Ti $2p_{3/2}$ (458 eV). In the O 1s region, a clear peak around 532 eV assigned to the surface adsorbed –OH was observed together with other peak at 520 eV assigned to the lattice oxygen. On the other hand, the peaks of N 1s and F1s with high-noise level were observed due to the low content of two dopants, which are consistent with the EDS results.[31-32]

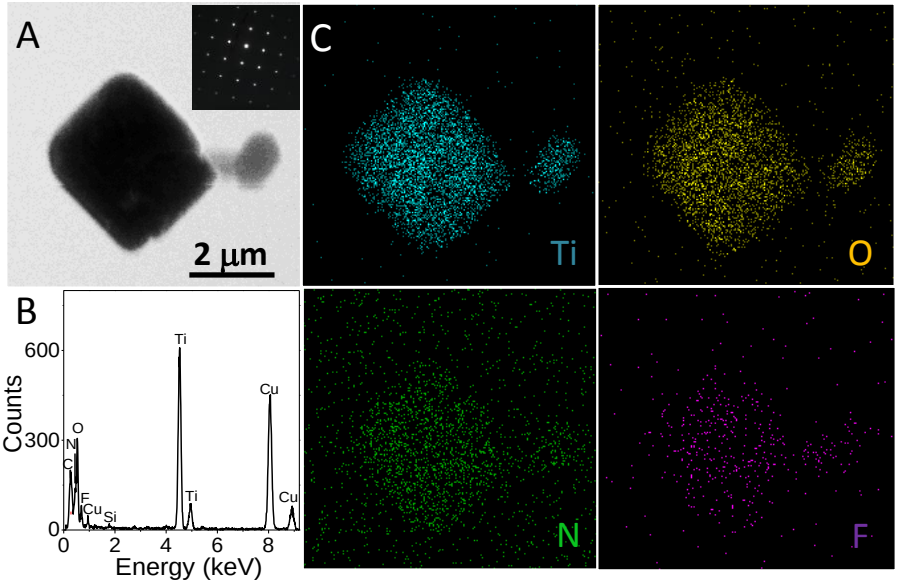

Fig. 4 (A) STEM, (B) EDX spectrum, and (C) elemental mapping images of NFT-500. The elements of Ti, O, N, and F are shown in blue, yellow, green, and purple color.

The optical responses of NFT are variable with the calcination temperature, which is indicated by the UV-Vis diffuse reflectance spectra (DRS) in Fig. 5A. Compared with the pristine TMC, the absorption edge shifted to longer wavelength in the visible light region with increasing the calcination temperature.[11] It is remarkably worth that add-on shoulders for NFT-300 and NFT-400 were imposed from 380 nm to 550 nm due to the N doping with an isolated N 2p state in the midgap. The effective extension for light absorption of NFT-500 is mainly response to the higher content of N dopants depending on the annealing temperature. Additionally, NFT-600 exhibited a low optical intensity due to the loss of two dopants after the high temperature annealing (Table 1).[30] With increasing the calcination temperature, the thermal conversion was monitored by the thermogravimetric analyses (TG-DTA) of NH_4TiOF_3 in Fig. 5B. After NH_4TiOF_3 was formed (equation 1), there was no obvious weight loss below 200 ^oC where water is adsorbed on

hygroscopic TiO_2.[14-15] In the temperature range of 250 °C to 500 °C, a sharp endothermic peak was arisen due to the chemical phase transformation from the intermedium to TiO_2 (equations 2 and 3). This implies that the major contributions of the weight loss are attributed to the progressive release of NH_3 and HF. In the closed glass vessel, it can be inferred that the amount of N and F was saturated firstly and then start to be doped on TMC gradually. Coincided with the result of XRD, there was also no additional weight loss observed from 500 °C to 600 °C during the topochemical transformation due to its good thermal stability with maximum doping.

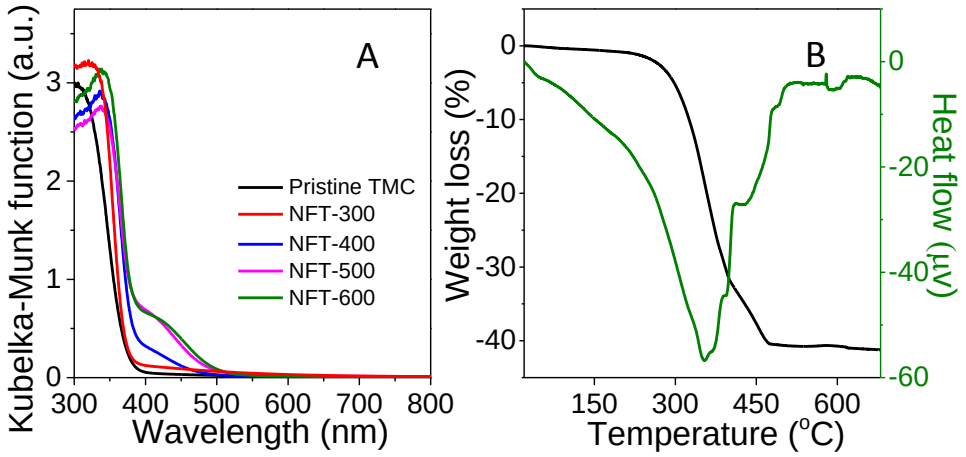

Fig. 5 (A) Steady state diffuse reflectance spectra of NFT with various temperatures (NFT-300 ~ 600) compared with the pristine TMC, and (B) TG-DTA curves of the NH_4TiOF_3 in N_2.

$$Ti^{4+} + 3F^- + NH_4^+ + H_2O \rightleftarrows NH_4TiOF_3\downarrow + 2H^+ \quad (1)^{22}$$

$$NH_4TiOF_3 + H_2O \rightleftarrows TiO_2\downarrow + 2HF + NH_4F \quad (2)^{16}$$

$$NH_4F \rightleftarrows HF\uparrow + NH_3\uparrow \quad (3)^{33}$$

The photocatalytic reductive efficiency of pristine TMC and NFT synthesized at various temperatures was evaluated from the reduction of Cr (VI) to Cr (III) under the visible irradiation ($\lambda \geq 420$ nm) in Fig. 6A. The reductive rate for Cr (VI) to Cr (III) was estimated to be 0.0011, 0.0013, 0.0017, 0.0066, and 0.0030 min^{-1} for pristine TMC and NFT-300 ~ 600, respectively from the slopes of the linear plot between $\ln(C_0/C)$ and irradiation time. As compared to pristine TMC with feeble response to visible light, N and F doped TMC, NFT-300 and NFT-400, showed markedly improvement of the reductive efficiency due to the strengthen doping with the elevating temperature. It was obviously shown that the NFT-500 exhibited the highest photocatalytic efficiency due to the strongest ability of the visible light harvesting by the large

amount of N doped content.[34] On the other hand, NFT-600 with similar optical response to NFT-500 showed nearly half efficiency, which were resulted from the poor charge migration among the random nanoparticles because of the collapsed mesocrystal structure.[23, 35] The negligible degradation was observed in the absence of NFT or visible light irradiation. It is reasonable that the N content corresponds to the absorption ability from N in the localized midgap state, influencing the efficiency of the photoreduction of Cr (VI).

To clarify the role of F codoping on the predominant energy sate of N, the NFT-500 was subsequently washed by NaOH aqueous solution (NFT-NaOH) to controllably remove the surface adsorbed F. The fraction of surface adsorbed –OH (532 eV) may be increased by removing F in a part. Intriguingly, a die-off (20%) in Cr (VI) reduction by NFT-NaOH was observed even it possess the similar optical absorption and surface area to NFT-500. In order to clarify the interaction or effect of two dopants on the photocatalytic efficiency, the degradation of methylene blue (MB) was examined under the visible (λ = 420~440 nm) or UV light (λ = 365 nm) irradiation (Fig. 6B).[32] During the visible light irradiation, NFT-500 exhibited the highest degradation efficiency than the pristine TMC and NFT-NaOH, while no degradation was shown using the sole F doping TiO_2 under the visible light irradiation, because the atomic p level of F (*ca*. –11.0 eV) exists below the O (*ca*. –8.5 eV) and no visible absorption exists for the sole F doping TiO_2.[9] On contrary, the pristine TMC with intrinsic absorption showed the superior efficiency under the UV irradiation in spite of the negligible activity under the visible light irradiation. The duplicated runs were carried out to average the results with the similar tendency. It is suggested that the poor contribution of surface adsorbed F for NFT-NaOH is leading to the lower photocatalytic efficiency under the visible or UV light case.[30] From the comparison of the redox reaction under the visible or UV light irradiation, it is suggested that the effect of N and F dopants affects the overall reaction efficiency.

As a powerful technique, the femtosecond TDR spectroscopic measurement was performed to clarify the charge carrier dynamics in the photocatalytic reaction under the visible or UV light irradiation (Fig. 6C). The schematic illustration of the energy diagram is shown in Fig. 6D. After the sufficient generation of charge carriers upon the 440-nm laser excitation of NFT-500, electrons are excited from N 2p in the isolated midgap sate to the conduction band Ti 3d to be directly trapped (τ_1, 2.1 ps; Table 2) on the adjacent oxygen vacancy (V_o) generated from the codoping (red line in Fig. 6D).[31, 36] On the other hand, the generated holes are separated and

localized at the N 2p state at the same time. After the equilibrium between electrons in the surface trap and the bulk (τ_2, 52 ps; Table 2), the favorable reduction pathway and charge recombination occur (τ_3, 2751 ps; Table 2) in NFT-500. Generally, a longer lifetime of charge carrier enhances the photocatalytic efficiency. However, it is unusual that NFT-NaOH with the lower efficiency exhibited longer lifetimes of two components (τ_2, 63 ps; τ_3, 3086 ps) than those for NFT-500, showing the similar photocatalytic efficiency under the UV irradiation (see below). The shorter lifetime of NFT-NaOH (τ_1, 0.5 ps) observed at the first decay component corresponds to the inequivalent oxygen atom at the deep state of Vo because F is removed in NFT-NaOH as compared in NFT-500.[31-32] The time profile of the transient adsorption at 900 nm for pristine TMC is not discussed here, because it is probably resulted from unknown impurities. Under the UV laser excitation at 330 nm, the generated electrons and holes on pristine TMC are usually trapped at the surface defects (τ_1) separately to yield reductive oxygen species (black line) with enhancing photocatalytic efficiency (longer τ_2 and τ_3).[30] In this case, NFT-500 showed three components 5.2 ps (τ_1), 60 ps (τ_2), and 2510 ps (τ_3) in Fig. 6C and Table 2. Compared with those for pristine TMC, 2.1 ps (τ_1), 36 ps (τ_2), and 1288 ps (τ_3) in Table 2, it is shown that the slower recombination process on NFT-500 corresponds to the hole localized on the N 2p state in Fig. 6D.[37-38] On the other hand, the efficient charge separation of NFT-500 was observed with the lower photocatalytic efficiency under the UV irradiation compared to that for pristine TMC, suggesting the low yield of hydroxyl radical because of less positive potential of N in the localized midgap state (Fig. 6D).[39] Compared with NFT-500 under the same irradiation condition, NFT-NaOH showed low photocatalytic efficiency even though the longer lifetime, 13.2 ps (τ_1), 110 ps (τ_2), and 3298 ps (τ_3). It has been reported that the surface adsorbed F^- replaces the sites of adsorbed OH^- ($\equiv Ti–OH + F^- \rightarrow \equiv Ti–F + OH^-$) for NF-doped TiO_2,[31,32] suggesting the electron flow occurs to O_2 through $\equiv Ti–F$ to yield superoxide anion ($O_2^{\bullet -}$) which changes to hydroxyl radical ($OH^{\bullet}$) via the protonation and O-O bond cleavage processes.[30] Therefore, the higher amount of $OH\cdot$ is accomplished together with the preferential adsorption of MB on the acidic surface for NFT-500 to show the higher photocatalytic efficiency under the visible light irradiation.[30,32]

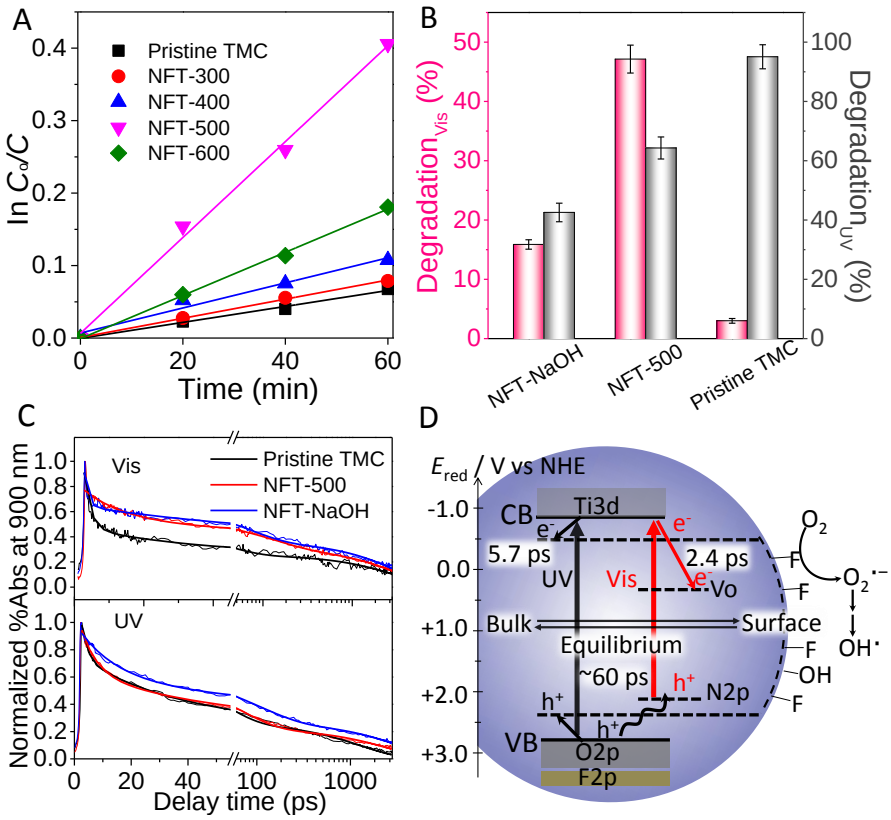

Fig. 6 (A) Photoreduction of Cr (VI) between pristine TMC and NFT under the visible light irradiation. (B) Comparison of MB degradation from pristine TMC, NFT-500, and NFT-NaOH under the visible or UV light irradiation, and (C) their corresponding normalized transient absorption trace. (D) Schematic illustration of the spatial and energetic distribution of electrons and holes in NFT after excitation at 440 nm (red arrow) and 330 nm (black arrow). The V_o denotes the oxygen vacancy.

Table 2. Kinetic Parameters of Decays for Pristine TMC, NFT-500, and NFT-NaOH under the Visible or UV Light Excitation.

Sample	Visible light			UV light		
	τ_1 (ps)	τ_2 (ps)	τ_3 (ps)	τ_1 (ps)	τ_2 (ps)	τ_3 (ps)
Pristine TMC	1.1 (48%)	27 (26%)	2945 (26%)	2.1 (52%)	36 (32%)	1288 (16%)
NFT-500	2.1 (33%)	52 (33%)	2751 (34%)	5.2 (46%)	60 (33%)	2510 (21%)
NFT-NaOH	0.5 (34%)	63 (30%)	3086 (36%)	13.2 (40%)	110 (33%)	3298 (27%)

4. Conclusion

In this present work, the author was successfully synthesized NFT with N and F codopants into TMC during the topochemical transformation. The NFT with (001) facet exposed exhibited uniform distribution of two dopants depending on the annealing temperature. Their reductive photocatalytic efficiency from Cr (VI) to Cr (III) was consistent with the optical absorption by N in the isolated midgap state, which is doped with a certain amount after the annealing. It is found that NFT-500 exhibited the highest photocatalytic efficiency due to the highest concentration of N with the surface modification from F coupling. Together with the charge transfer dynamics, the poor degradation of MB for NFT-NaOH under the visible or UV light irradiation is explained by the effect of F codoping with high yield hydroxyl radical and preferential adsorption, accompanying with assistant role to N in the localized midgap state. TMC with N and F codoping presents a particular interest on promising visible light driven photocatalytic efficiency and allows us to devote the effect on developing new materials as the photocatalyst.

5. Reference

(1) Fujishima, A.; Honda, K. *Nature* **1972**, *238*, 37.

(2) Ma, Y.; Wang, X.; Jia, Y.; Chen, X.; Han, H.; Li, C. *Chem. Rev.* **2014**, *114*, 9987.

(3) Wang, L.; Sasaki, T. *Chem. Rev.* **2014**, *114*, 9455.

(4) Bai, Y.; Mora-Sero, I.; De Angelis, F.; Bisquert, J.; Wang, P. *Chem. Rev.* **2014**, *114*, 10095.

(5) Walter, M. G.; Warren, E. L.; McKone, J. R.; Boettcher, S. W.; Mi, Q.; Santori, E. A.; Lewis, N. S. *Chem. Rev.* **2010**, *110*, 6446.

(6) Schneider, J.; Matsuoka, M.; Takeuchi, M.; Zhang, J.; Horiuchi, Y.; Anpo, M.; Bahnemann, D. W. *Chem. Rev.* **2014**, *114*, 9919.

(7) Sang, L.; Zhao, Y.; Burda, C. *Chem. Rev.* **2014**, *114*, 9283.

(8) Pelaez, M.; Nolan, N. T.; Pillai, S. C.; Seery, M. K.; Falaras, P.; Kontos, A. G.; Dunlop, P. S. M.; Hamilton, J. W. J.; Byrne, J. A.; O'Shea, K.; Entezari, M. H.; Dionysiou, D. D. A *Appl. Catal. B: Environ.* **2012**, *125*, 331.

(9) Asahi, R.; Morikawa, T.; Irie, H.; Ohwaki, T. *Chem. Rev.* **2014**, *114*, 9824.

(10) Ong, W. J.; Tan, L. L.; Chai, S. P.; Yong, S. T.; Mohamed, A. R. *Nanoscale* **2014**, *6*, 1946.

(11) Chen, D.; Jiang, Z.; Geng, J.; Zhu, J.; Yang, D. *J. Nanopart. Res.* **2008**, *11*, 303.

(12) Hojamberdiev, M.; Zhu, G.; Sujaridworakun, P.; Jinawath, S.; Liu, P.; Zhou, J. P. *Powder Technol.* **2012**, *218*, 140.

(13) Liu, Y.; Zhang, Y.; Tan, H.; Wang, J. *Cryst. Growth Des.* **2011**, *11*, 2905.

(14) Liu, Y.; Zhang, Y.; Li, H.; Wang, J. *Cryst. Growth Des.* **2012**, *12*, 2625.

(15) Liu, Y.; Zhang, Y.; Wang, J. *CrystEngComm* **2013**, *15*, 791.

(16) Lee, H. K.; Lee, S. W. *Chem. Lett.* **2015**, *44*, 604.

(17) Tachikawa, T.; Majima, T. *NPG Asia Mater.* **2014**, *6*, e100.

(18) Liu, G.; Yang, H. G.; Pan, J.; Yang, Y. Q.; Lu, G. Q.; Cheng, H. M. *Chem. Rev.* **2014**, *114*, 9559.

(19) Bergström, L.; Sturm, E. V.; Salazar-Alvarez, G.; Cölfen, H. *Acc. Chem. Res.* **2015**, *48*, 1391.

(20) Liu, Y.; Zhang, Y.; Wang, J. *CrystEngComm* **2014**, *16*, 5948.

(21) Di Valentin, C.; Finazzi, E.; Pacchioni, G.; Selloni, A.; Livraghi, S.; Czoska, A. M.; Paganini, M. C.; Giamello, E. *Chem. Mater.* **2008**, *20*, 3706.

(22) Bian, Z.; Tachikawa, T.; Majima, T. *J. Phys. Chem. Lett.* **2012**, *3*, 1422.

(23) Zhang, P.; Tachikawa, T.; Bian, Z.; Majima, T. *Appl. Catal. B: Environ.* **2015**, *176-177*, 678.

(24) Bian, Z.; Tachikawa, T.; Zhang, P.; Fujitsuka, M.; Majima, T. *Nat. Commun.* **2014**, *5*, 3038.

(25) Zhou, L.; Smyth-Boyle, D.; O'Brien, P. *J. Am. Chem. Soc.* **2008**, *130*, 1309.

(26) Gordon, T. R.; Cargnello, M.; Paik, T.; Mangolini, F.; Weber, R. T.; Fornasiero, P.; Murray, C. B. *J. Am. Chem. Soc.* **2012**, *134*, 6751.

(27) Wang, W.; Lu, C.; Ni, Y.; Su, M.; Huang, W.; Xu, Z. *Appl. Surf. Sci.* **2012**, *258*, 8696.

(28) Wang, W.; Ni, Y.; Lu, C.; Xu, Z. *Appl. Surf. Sci.* **2014**, *290*, 125.

(29) Wang, J.; Tafen, D. N.; Lewis, J. P.; Hong, Z.; Manivannan, A.; Zhi, M.; Li, M.; Wu, N. *J. Am. Chem. Soc.* **2009**, *131*, 12290.

(30) Brauer, J. I.; Szulczewski, G. *J. Phys. Chem. B* **2014**, *118*, 14188.

(31) Kumar, N.; Maitra, U.; Hegde, V. I.; Waghmare, U. V.; Sundaresan, A.; Rao, C. N. *Inorg. Chem.* **2013**, *52*, 10512.

(32) Cheng, J.; Chen, J.; Lin, W.; Liu, Y.; Kong, Y. *Appl. Surf. Sci.* **2015**, *332*, 573.

(33) Gurdip, S.; lnder, P.; Jaspreet, K. *Indian J. Eng. Mater. Sci.* **2007**, *7*, 229.

(34) Kim, W.; Tachikawa, T.; Kim, H.; Lakshminarasimhan, N.; Murugan, P.; Park, H.; Majima, T.; Choi, W. *Appl. Catal. B: Environ.* **2014**, *147*, 642.

(35) Zhang, P.; Tachikawa, T.; Fujitsuka, M.; Majima, T. *Chem. Commun.* **2015**, *51*, 7187.

(36) Yamanaka, K. i.; Morikawa, T. *J. Phys. Chem. C* **2012**, *116*, 1286.

(37) Wu, H. C.; Lin, Y.-S.; Lin, S. W. *Int. J. Photoenergy* **2013**, *2013*, 1.

(38) Varley, J. B.; Janotti, A.; Van de Walle, C. G. *Adv.Mater.* **2011**, *23*, 2343.

(39) Hamilton, J. W. J.; Byrne, J. A.; Dunlop, P. S. M.; Dionysiou, D. D.; Pelaez, M.; O'Shea, K.; Synnott, D.; Pillai, S. C. *J. Phys. Chem. C* **2014**, *118*, 12206.

General Conclusion

Throughout this thesis, the potential and versatility of TMC photocatalyst in solar energy conversion have been studied after modification and doping.

In Chapter 1, reaction dynamics of photogenerated charge carriers in CoPi-deposited TMC and MoS_2-TMC was studied. In the case of CoPi-deposited TMC, ensemble-averaged experiment and single-particle spectroscopy were used to confirm their superior efficiency. The in situ single-particle fluorescence imaging technique with specific probes was used to monitor the photooxidative reaction on individual catalysts. The combination of CoPi/Pt co-deposition and the anisotropic electron flow in TMC significantly retarded the charge recombination.

On the other hand, it is demonstrated that 3D architectures of TMC uniformly packed with a chemically exfoliated MoS_2 shell exhibited promising reactive efficiency and good stability in synergetic hydrogen evolution. Their efficient interfacial electron transfer from the excited TiO_2 moieties to the decorated ultrathin MoS_2 shell was effectively monitored to promote their good photocatalytic activity in HER.

In Chapter 2, a series of TMCs with controllable {001} and {101} facets was successfully synthesized using a crystal growth inhibitor (NH_4F). Their photocatalytic performances are explored in pollutant degradation and H_2 evolution. It is suggested that the {101} facets prefer reduction, whereas the {001} facets favor oxidation, and anisotropic electrons flow in dye system, which are attributed to crystal-facet-dependent surface adsorption and tunable electron transfer.

In chapter 3, the author facilely designed doped TMC via topotactic transformation confined doping. In the first part, the details of crystal growth, phase transition, and dynamic structural evolution during the topotactic transformation from NH_4TiOF_3 to F-doped TMC were monitored via in situ temperature-dependent techniques. The intermediate $TiOF_2$ was incorporated as F color centers to F-doped TMC without any morphological change. Their comparison of charge transfer dynamics with the photocatalytic efficiency confirmed that n-type F-doping induces faster electronic mobility and favorable surface modification for the efficient visible-light driven H_2 generation.

Secondly, the author successfully synthesized TMC with the uniform distribution of N, F dopants from the direct annealing of the intermediate NH_4TiOF_3 during the topochemical transformation. The photoreductive efficiency of Cr (VI) to Cr (III) was correlated to the optical absorption dependent on the dopant content at various annealing temperatures. It is found that the doping of N in the localized mid-gap state together with the surface F coupling enhanced the photocatalytic degradation of MB based on charge transfer dynamics under the visible or UV light irradiation.

To conclude, it is clear that this thesis introduces the development of TMC and clarify their photochemical characteristics from UV light to visible-light region after modification or doping. All works help us to gain an in-depth understanding of the efficient charge separation within appropriate morphologies of materials with good structure-induced photocatalytic activity for environmental remediation and energy conversion. With intensive study of extraordinary performance in TMC, more expected device and superstructure will be designed to significantly improve the limitation of low quantum efficiency and wide band gap from TiO_2. The mesocrystal is still at the early stage of development, the promising future of it will be foreseen as the basic building block for next generation high-end materials in energy and environment.

List of Publications

1. Efficient Charge Separation and Photooxidation on Cobalt Phosphate-Loaded TiO_2 Mesocrystal Superstructures
   Takashi Tachikawa, Peng Zhang, Zhenfeng Bian, and Tetsuro Majima.
   J. Mater. Chem. A **2014**, 10(2), 3381-3388.

2. Selective Photoredox Activity on Specific Facet-Dominated TiO_2 Mesocrystal Superstructures Incubated with Directed Nanocrystals
   Peng Zhang, Takashi Tachikawa, Zhenfeng Bian, and Tetsuro Majima.
   Appl. Catal. B: Environ. **2015**, 176-177, 678-686.

3. Efficient Charge Separation on 3D Architectures of TiO_2 Mesocrystals Packed with a Chemically Exfoliated MoS_2 Shell in Synergetic Hydrogen Evolution
   Peng Zhang, Takashi Tachikawa, Mamoru Fujitsuka, and Tetsuro Majima.
   Chem. Commun. **2015**, 33(51), 7187-7190.

4. In Situ Topotactic n-Type F-Doping into TiO_2 Mesocrystal Superstructures for Efficient Visible-Light Driven Hydrogen Generation
   Peng Zhang, Takashi Tachikawa, Mamoru Fujitsuka, and Tetsuro Majima.
   Revision.

5. TiO_2 Mesocrystal with Nitrogen and Fluorine Codoping during Topochemical Transformation: Efficient Visible Light induced Photocatalyst with the Effect of Codopants
   Peng Zhang, Mamoru Fujitsuka, and Tetsuro Majima.
   *Appl. Catal. B: Environ.***2016**, 185, 181-188.

Other publication

1. Au/TiO_2 Superstructure-Based Plasmonic Photocatalysts Exhibiting Efficient Charge Separation and Unprecedented Activity
   Zhenfeng Bian, Takashi Tachikawa, Peng Zhang, Mamoru Fujitsuka, and Tetsuro Majima.
   J. Am. Chem. Soc. **2013**, 136(1), 458-465.

2. A Nanocomposite Superstructure of Metal Oxides with Effective Charge Transfer Interfaces
   Zhenfeng Bian, Takashi Tachikawa, Peng Zhang, Mamoru Fujitsuka, and Tetsuro Majima.
   Nat. Commun. **2014**, 5:3038, 1-9.

3. Stimulated Ti^{3+} Self-Doped Nanocryatal TiO_2 with Amorphous Tunnel Layer as Metal-Insulator Semiconductor via Atomic Layer Deposition for Enhanced Visible-Light Driven Hydrogen Evolution from Formic Acid
   Peng Zhang, Takashi Tachikawa, Mamoru Fujitsuka, and Tetsuro Majima.
   Submitted.

Acknowledgements

The author wishes to express his sincerest gratitude to Professor Tetsuro Majima, the Institute of Science and Industrial Research (SANKEN), Osaka University, for his invaluable supervision, guidance, and advice throughout the doctoral study.

The author deeply appreciates Assistant Professor Takashi Tachikawa (currently, Associate Professor in Kobe University) for his valuable suggestion and helpful support during the doctoral course. Specially Appointed Associate Professor Mamoru Fujitsuka for his helpful guidance of research activities in laser flah photolysis. The author is also indebted to Professor Akira Sugimoto, Professor Mikiji Miyata, Associate Professor Kiyohiko Kawai, Assistant Professor Yasuko Osakada, Assistant Professor Sachiko Tojo, and Assistant Professor Sooyeon Kim for their kind helps and advice.

The author is also deeply grateful to Professor Yoshio Aso and Professor Naoto Chatani, and all professors of Applied Chemistry, Graduate School of Engineeing, Osaka University, for their suggestion and help in the preparation of this thesis.

Furthermore, the author appreciates Professor Hexing Li, department of chemistry, Shanghai Normal University (currently, Professor in Shanghai University of Electric Power) for his warm-hearted encouragements in the period of master cource.

The author would like to thank all the members of Professor Majima's research group, including Dr. Zhenfeng Bian, Dr. Man Jae Park, Dr. Zhaoke Zheng, Dr. Zaizhu Lou, Dr. Mingshan Zhu, Dr. Shaoqing Song, Mr. Shih-Hsun Lin, Miss Xiaoyan Cai, Mr. Chao Lu, Mr. Atsushi Tanaka, Mr. Ossama Elbanna, Mr. Shixiao Wei, Miss Mayuka Ishikawa, Miss Jiang Zhang, Mr. Tatsuya Ohsaka, Mr. Takeshi Koshimo, Mr. Yui Tei, Mr. Shunsuke Ano, Mr. Kenshi Nakao, Miss Ayaka Kuroda, Mr. Kota Nomura, Mr. Yoji Yamamoto, Mr. Yuma Ichinose, Mr. Yang Zhou, Miss Jie Xu, and Miss Sanae Tominaga (SANKEN) for their encouragement and help from research discussions to daily lives in Japan.

Finally, the author expresses to thank his family, fathter Cunling Zhang, mother Yumei Suo, elder sister Ting Zhang, wife Ling Li, and daughter Xiaoxi Zhang, for their endless supports,

encouragements and love during his doctoral study.

Peng Zhang

2016